

学位論文

Cosmological implications of  
non-topological solitons

(ノントポロジカルソリトンの宇宙論への影響)

平成29年12月博士（理学）申請

東京大学大学院理学系研究科

物理学専攻

洪 正平



Ph.D. Thesis

**Cosmological implications of  
non-topological solitons**

Department of Physics, Graduate School of Science  
University of Tokyo

Jeong-Pyong Hong

January 23, 2018

## Abstract

In this thesis, we mainly focus on two cosmological issues: charged soliton dark matter scenario, and inflatonic solitons in a recently motivated inflation model. Former is realized after the Affleck-Dine baryogenesis through the partial decay of Q-balls. We focus on the fact that these objects are detectable by the usual electromagnetic processes, unlike the ordinary neutral Q-balls. We apply the most stringent constraint from the MICA experiment to the model where the charged Q-balls are realized. We find that the MICA constraint is severer than those from IceCube, which probe neutral Q-ball process, leading to the smaller allowed parameter region. Secondly, we study the inflaton fragmentation into I-balls in E-models of  $\alpha$ -attractors. These are observationally favored due to the asymptotic flatness of the potentials, which can lead to the local fragmentation. Through the linear instability analysis and the lattice simulation, we find that the I-balls are formed for  $\alpha \lesssim \alpha_{\text{th}}^{\text{E}} \sim 10^{-3}$ , which is larger than in the case of T-models:  $\alpha_{\text{th}}^{\text{T}} \sim 10^{-4}$ .

# Contents

<b>1</b>	<b>Introduction</b>	<b>1</b>
<b>2</b>	<b>Standard cosmology</b>	<b>5</b>
2.1	Homogeneous isotropic universe . . . . .	5
2.1.1	Friedmann-Robertson-Walker metric . . . . .	5
2.1.2	Expansion of the universe . . . . .	6
2.1.3	Redshift . . . . .	7
2.1.4	Dynamics of expansion . . . . .	8
2.1.5	Density parameters . . . . .	9
2.1.6	Horizon . . . . .	11
2.1.7	Thermal history of the universe . . . . .	12
2.2	Perturbed universe . . . . .	24
2.2.1	Linear perturbations . . . . .	24
2.2.2	Evolution of the fluctuations . . . . .	28
<b>3</b>	<b>Inflationary universe</b>	<b>30</b>
3.1	Problems of standard cosmology . . . . .	30
3.1.1	Flatness problem . . . . .	30
3.1.2	Horizon problem . . . . .	31
3.1.3	Monopole problem . . . . .	31
3.1.4	Gravitino problem . . . . .	32
3.1.5	Solution through accelerated expansion . . . . .	33
3.2	Slow-roll inflation . . . . .	34
3.2.1	Inflation models . . . . .	36
3.3	Generation of primordial fluctuations . . . . .	42
3.3.1	Model dependence . . . . .	46
3.4	Reheating . . . . .	49
3.5	Reheating temperature and e-folds . . . . .	52

<b>4</b>	<b>Affleck-Dine mechanism</b>	<b>54</b>
4.1	Baryogenesis . . . . .	54
4.1.1	Sakharov's conditions . . . . .	54
4.2	Flat directions in MSSM . . . . .	57
4.3	Dynamics of Affleck-Dine field and baryogenesis . . . . .	57
4.3.1	Gravity mediation case . . . . .	58
4.3.2	Gauge mediation case . . . . .	60
<b>5</b>	<b>Q-balls</b>	<b>63</b>
5.1	Q-ball solutions . . . . .	63
5.1.1	General properties . . . . .	63
5.1.2	Thin-wall approximation . . . . .	66
5.1.3	Q-balls in SUSY . . . . .	68
5.2	Q-ball formation after the AD mechanism . . . . .	71
5.2.1	Gravity mediation case . . . . .	72
5.2.2	Gauge mediation case . . . . .	74
<b>6</b>	<b>Charged Q-balls</b>	<b>75</b>
6.1	Charged Q-ball solution and its properties . . . . .	75
<b>7</b>	<b>Charged Q-ball dark matter from <math>B</math> and <math>L</math> direction</b>	<b>80</b>
7.1	Charged Q-balls in two scalar model . . . . .	80
7.2	Charged Q-ball dark matter scenario . . . . .	83
7.2.1	Maximal electric charge . . . . .	83
7.2.2	Evolution of Charged Q-balls until the present . . . . .	84
7.2.3	Constraints from MICA direct detection . . . . .	85
7.3	Charged Q-ball decay rates into fermions . . . . .	91
7.3.1	Setup and method . . . . .	91
7.3.2	Results . . . . .	94
7.4	Brief summary . . . . .	97
<b>8</b>	<b>I-balls</b>	<b>100</b>
8.1	I-ball solution and its existence conditions . . . . .	100
<b>9</b>	<b>I-ball formation in E-models of <math>\alpha</math>-attractors</b>	<b>104</b>
9.1	Model . . . . .	105
9.2	I-ball solution and its profile . . . . .	107
9.3	Linear instability analysis . . . . .	110
9.4	Lattice simulations . . . . .	111
9.5	Implications . . . . .	113
9.6	Brief summary . . . . .	117

<b>10 Conclusions</b>	<b>118</b>
<b>Acknowledgements</b>	<b>121</b>
<b>A Notations</b>	<b>122</b>
<b>B Geometry in the expanding spacetime</b>	<b>124</b>
B.1 Geometry in FRW metric . . . . .	124
B.1.1 Metric . . . . .	124
B.1.2 Christoffel symbols . . . . .	125
B.1.3 Ricci tensor and scalar . . . . .	126
B.2 Geometry in perturbed metric . . . . .	126
B.2.1 Metric . . . . .	127
B.2.2 Christoffel symbols . . . . .	127
B.2.3 Ricci tensor and scalar . . . . .	127
<b>C Flat directions in MSSM</b>	<b>130</b>
<b>D Fermions outside the charged Q-ball</b>	<b>134</b>

# Chapter 1

## Introduction

Solitons, which are spatially localized objects, appear in various cosmological contexts. The topological defects, which are produced after a symmetry breaking, are well-known examples of the solitons, including monopoles, cosmic strings, domain walls, etc. These are classically stable due to the conservation of topological charge. Their peculiar origins and properties can alter the scenario in nontrivial ways. For instance, the well-known monopole problem is due to the fact that the monopole is stable by virtue of its topological charge, in spite of its heavy mass. The domain walls pose another serious problem, called domain wall problem, since after the formation they extend their areas along with the expansion, which leads to their domination of the universe.

While these topological solitons are more familiar objects to many of us, there also exist localized objects of simpler structures without any topological charge. These are called non-topological solitons, which are usually extremely massive spherical scalar condensates, and their classical stability is again guaranteed by a certain conserved quantity, such as global  $U(1)$  charge. Due to the heavy masses, their classical behavior resembles that of non-relativistic matter. However, their individual profile, or the inner structures, leads to unique decaying properties, etc., which are different from those of ordinary point particles. In many cases, their decay rates into light particles will be of interest, since their decay must occur before the Big Bang Nucleosynthesis. In the case where they are stable against the decay, their present relics must not dominate the universe. If the relics are of a proper amount, they may be able to explain the abundance of the dark matter (DM) of the present universe. This will be one of the main interests in this thesis.

Inflatonic solitons are localized configurations of inflaton field, which are of importance in rather different contexts. Since all the other species are generated from the inflaton, their decaying properties become more important in that they determine the beginning of the radiation-dominated era. They will also affect



the amount of certain non-thermal relics, which is independent of the radiation temperature, but depends on the initial particle production. The formation of spatially localized solitons is generically expected to generate the gravitational waves (GW), since it induces the anisotropic stress tensor. Inflaton solitons are possible to give a large amount of GW energy, since the inflaton dominates the energy of the universe during and after inflation. However, it is worthwhile to point out that if the soliton formation is realized just after the inflation, for instance, the scale of the fluctuation is naively expected to be about the size of the horizon at that era, and this is actually too small in frequency to be observed, even after the scale is redshifted until the present universe.

In this thesis, we study the cosmological implications of non-topological solitons. The first of our interest is the investigation of the soliton dark matter scenario, where as a dark matter candidate, we consider an object called charged Q-ball. After the Affleck-Dine (AD) baryogenesis [1, 2], the Affleck-Dine field, which is typically a MSSM flat direction, fragments into localized lumps, called Q-balls [3, 4, 5, 6], since the supersymmetry (SUSY) breaking gives the correction to the AD potential that induces the negative pressure. In the models where the SUSY breaking is mediated by gauge interaction, which are called gauge mediated SUSY breaking models, the Q-ball is known to be stable against the decay for large enough charge [7], and this leads to the possibility of the Q-ball dark matter scenario. Since the Q-ball relics must be of a proper amount to be the dark matter, the properties of the Q-balls are constrained by the observations, which in turn leads to the constraints on the model, in this case, gauge mediation model. Since the flat direction is neutral under the gauge interactions, the only known detectable process of the Q-ball is KKST process [8], where the Q-ball absorbs a proton and emits a pion of  $\sim \text{GeV}$  through gluino exchange. This occurs since the baryon dissociates due to the  $SU(3)$  breaking inside the Q-ball. However, if the flat direction consists not only of a baryonic but also of a leptonic component, there is no suppression of the decay channel into charged leptons, which makes the Q-ball electrically charged. Hence, this kind of Q-ball is detectable through the electromagnetic reactions. Since this is categorized as charged dark matter, it must be consistent with various observations besides the DM abundance, such as Big Bang Nucleosynthesis (BBN), bullet cluster, etc. We expect that these are satisfied by virtue of the extremely heavy mass of the Q-ball (typically  $10^{20}$  to  $10^{30}$  GeV), which leads to very small number density in order to satisfy the DM abundance. However, we find that the constraint from the direct detection of the charged DM flux on earth is quite severe and the significant region of the model parameters is excluded, compared to the ordinary Q-ball DM scenario, which means that a small improvement of the sensitivity either may detect the charged Q-ball DM, or gives a stronger constraint on the model [9, 10, 11].

It is worthwhile to comment on our implicit assumption that the decay of the leptonic component is sufficiently fast, so that the electrically charged Q-balls are formed in the early universe. In order to gain some insight on that matter, we derive the decay rate of the charged Q-ball of one scalar into fermions using semiclassical method [12], and point out that there is virtually no difference in the decay rate compared to the neutral Q-ball, mainly due to the smallness of the electric charge compared to the baryon or lepton number of each Q-ball. The decay rate of the neutral Q-ball is typically known to be of the order of GeV, hence we conclude that the decay of the charged Q-ball is sufficiently fast, which validates our naive assumption.

Our second interest is in the study on the inflatonic soliton formation in recently proposed inflation models. Recent observations of cosmic background radiation (CMB) [13] have excluded the various class of inflation models, including single power-law potential models, through the combined constraints on the spectral index  $n_s$  and the tensor-to-scalar ratio  $r$ . A new class of inflationary models called  $\alpha$ -attractors was recently proposed [14, 15, 16], which unify many kinds of inflation models by one (phenomenologically) free-parameter  $\alpha$ : For example, the quadratic inflation model [17, 18] and the Starobinsky model [19, 20] are obtained by  $\alpha = \infty$  and  $\alpha = 1$ , respectively.  $\alpha$ -attractors, which are currently categorized into T- and E-models, are observationally favored due to the asymptotic flatness of the potentials. It is known that such a flatness of the potential induces negative pressure and leads to the inflaton fragmentation into the quasi-stable objects called I-balls, which are also called oscillons [21, 22, 23, 24]. I-balls are real scalar condensate, whose stability comes from the conservation of adiabatic invariant  $I$ . It was reported that the I-balls are formed in T-models, for  $n = 1$ ,  $\alpha \lesssim 10^{-4}$  [25, 26]. This is because the negative quartic term induces the negative pressure on the inflaton. In E-models, however, all the even-order terms are positive, and odd-order terms make the potential asymmetric and flatter than quadratic only for  $\phi > 0$ , with  $\phi$  inflaton, which may lead to different phenomena from the T-models. We investigate the possibility of the I-ball formation in E-models [27]. In order for the instability to overcome the cosmic expansion, small  $\alpha$  is favored, since the initial Hubble rate is roughly proportional to  $\alpha$ . We treat  $\phi$  in linear instability analysis and examined whether fluctuation grows for small  $\alpha$ . We find that the instability grows for  $\alpha \lesssim 10^{-3}$ . In order to confirm the I-ball formation, one must follow the non-linear dynamics. We perform the lattice simulations in 1D, 2D, 3D, by modifying *LatticeEasy* [28], which is a C++ program designed for simulating the scalar field dynamics under the cosmic expansion. We confirm that indeed I-balls are formed for  $\alpha \lesssim 10^{-3}$ .

This thesis is organized as follows. In Chap. 2 and Chap. 3, we briefly review basic issues on standard cosmology and inflation. Then, in Chap. 4 and Chap. 5,

we review Affleck-Dine mechanism and Q-balls, which are formed after the Affleck-Dine mechanism. In Chap. 6 and Chap. 7, we introduce the charged Q-ball and investigate the scenario of charged Q-ball dark matter. In Chap. 8 and Chap. 9, we briefly review the I-ball solution and its existence condition, and study the I-ball formation in E-models of cosmological  $\alpha$ -attractors. Finally in Chap. 10, we conclude this thesis.

# Chapter 2

## Standard cosmology

In this chapter, we briefly review the standard big bang cosmology, which mainly concerns the evolution of the universe that is assumed to be nearly homogeneous and isotropic. Our universe is believed to be expanding, which is driven by the energy component that is dominant in that era. The energy of the universe essentially consists of all existing particles, and in the framework of standard cosmology, these are usually assumed to be the species predicted by standard model (SM) of particle physics. We solve the dynamics of the expansion of spacetime in the presence of SM particles. The deviation from homogeneity and isotropy is also important in that it drives the formation of the structures in the universe. We treat this fluctuation perturbatively and study its evolution.

### 2.1 Homogeneous isotropic universe

#### 2.1.1 Friedmann-Robertson-Walker metric

The standard cosmology is governed by a big assumption, which states that there is no special point or direction in the universe. This assumption, called cosmological principle, leads to a very simple geometric structure of the universe, which is given by the following metric:

$$ds^2 = g_{\mu\nu}dx^\mu dx^\nu = dt^2 - a^2(t) \left( \frac{dr^2}{1 - Kr^2} + r^2 d\Omega \right), \quad (2.1)$$

where  $a(t)$  is the scale factor of the universe, which is usually normalized to be unity at present. The constant  $K$  gives the three-dimensional curvature through the following relation:

$$R^{(d=3)} = -\frac{6K}{a^2}, \quad (2.2)$$

where  $R^{(d=3)}$  denotes the three-dimensional Ricci scalar:  $K > 0$  gives the closed universe with positive curvature;  $K < 0$  the open universe with negative curvature; and  $K = 0$  the flat universe. Here, due to our metric sign  $(+, -, -, -)$ , negative (positive)  $R^{(d=3)}$  gives positive (negative) spatial curvature. Our universe is known to be nearly flat by observations, as we will see later. The metric Eq. (2.1) determined by the cosmological principle is called Friedmann-Robertson-Walker (FRW) metric.

### 2.1.2 Expansion of the universe

The physical distance between two points  $A$  and  $B$  is given as

$$d = \int_A^B dl \quad (2.3)$$

$$= a(t) \int dr \frac{1}{\sqrt{1 - Kr^2}}, \quad (2.4)$$

which is also called proper distance. This distance changes with time since it is proportional to the scale factor:

$$\dot{d} = \frac{\dot{a}}{a} d \quad (2.5)$$

$$= H d, \quad (2.6)$$

where we defined the Hubble rate  $H$  as follows:

$$H \equiv \frac{\dot{a}}{a}. \quad (2.7)$$

The present value of the Hubble rate  $H_0$ , which is called Hubble constant, is known by observations [29] as

$$H_0 \simeq 68 \text{ km s}^{-1} \text{ Mpc}^{-1}, \quad (2.8)$$

which means that our universe is expanding. This appears as the recessional velocities of distant objects such as galaxies:

$$v \equiv \dot{d} \quad (2.9)$$

$$= H d, \quad (2.10)$$

which is nothing but the Hubble law. The Hubble constant is also denoted by the following parameter:

$$h \equiv H_0 / (100 \text{ km s}^{-1} \text{ Mpc}^{-1}), \quad (2.11)$$

whose observational value becomes  $h \simeq 0.68$ .

### 2.1.3 Redshift

We study the effect of the expansion on the propagation of light, especially on its wavelength. Suppose that the light is emitted from  $(r, t) = (r_1, t_1)$ , which arrives to the observer at  $(r, t) = (0, t_0)$ . Since the light propagates satisfying  $ds^2 = 0$ , the following relation holds:

$$\int_{t_1}^{t_0} \frac{dt}{a(t)} = - \int_{r_1}^0 \frac{dr}{\sqrt{1 - Kr^2}}. \quad (2.12)$$

The right-hand side is independent of time, especially the same for the light that is emitted at  $t = t_1 + \delta t_1$  and arrives at  $t_0 + \delta t_0$ :

$$\int_{t_1}^{t_0} \frac{dt}{a(t)} = \int_{t_1 + \delta t_1}^{t_0 + \delta t_0} \frac{dt}{a(t)}, \quad (2.13)$$

which gives

$$\frac{\delta t_1}{a(t_1)} \simeq \frac{\delta t_0}{a(t_0)}, \quad (2.14)$$

assuming  $\delta t_0, \delta t_1 \ll t_0, t_1$ . Then, using  $\lambda_i \sim 1/\nu_i \sim 1/\delta t_i$  ( $i = 0, 1$ ), we obtain the following relation:

$$1 + z \equiv \frac{\lambda(t_0)}{\lambda(t_1)} = \frac{a(t_0)}{a(t_1)}, \quad (2.15)$$

which implies that the wavelength is redshifted due to the cosmic expansion. The parameter  $z$ , also called redshift, is frequently used as a quantity to represent the cosmic time.

The cosmic expansion also affects the propagation of a massive particle, which is described by the following geodesic equation:

$$\frac{d^2 x^\mu}{d\tau^2} + \Gamma_{\alpha\beta}^\mu \frac{dx^\alpha}{d\tau} \frac{dx^\beta}{d\tau} = 0. \quad (2.16)$$

The  $\mu = 0$  component gives

$$E \frac{dE}{dt} = -\Gamma_{\alpha\beta}^0 p^\alpha p^\beta \quad (2.17)$$

$$= -\frac{\dot{a}}{a}(E^2 - m^2), \quad (2.18)$$

where we used  $\Gamma_{0\beta}^0 = 0, \Gamma_{ij}^0 = -(\dot{a}/a)g_{ij}$  (see App. B), and  $p^\mu p_\mu = E^2 - g_{ij}p^i p^j$ . This can easily be solved as

$$E^2 - m^2 \propto a^{-2}, \quad (2.19)$$

which gives

$$p \propto a^{-1}. \quad (2.20)$$

This implies that the momentum of a massive particle is redshifted by the cosmic expansion.

#### 2.1.4 Dynamics of expansion

The dynamics of the FRW metric is governed by the following Einstein equation:

$$R_{\mu\nu} - \frac{1}{2}g_{\mu\nu}R - \Lambda g_{\mu\nu} = \frac{T_{\mu\nu}}{M_{\text{pl}}^2}, \quad (2.21)$$

where  $\Lambda$  is cosmological constant and  $T_{\mu\nu}$  denotes the energy-momentum tensor. We have also used the reduced Planck mass  $M_{\text{pl}} = 2.4 \times 10^{18}$  GeV. By virtue of the cosmological principle,  $T_{\mu\nu}$  has the following form of perfect fluid.

$$T_{\mu\nu} = -Pg_{\mu\nu} + (\rho + P)u_\mu u_\nu \quad (2.22)$$

where  $\rho$ ,  $P$  are the energy density and the pressure of the fluid, respectively, and  $u_\mu$  denotes four-velocity, which becomes  $u_\mu = (1, 0, 0, 0)$  in the rest frame of the fluid.

Then, due to the highly symmetric features, Eq. (2.21) can easily be solved, whose  $(0, 0)$  component becomes

$$G_{00} = 3 \left[ \left( \frac{\dot{a}}{a} \right)^2 + \frac{K}{a^2} \right] = \frac{T_{00}}{M_{\text{pl}}^2} \quad (2.23)$$

$$= \frac{\rho}{M_{\text{pl}}^2}, \quad (2.24)$$

which gives

$$\left( \frac{\dot{a}}{a} \right)^2 + \frac{K}{a^2} = \frac{\rho}{3M_{\text{pl}}^2}. \quad (2.25)$$

Note that we absorbed the cosmological constant into the energy-momentum tensor by treating it as a fluid with  $\rho_\Lambda = -P_\Lambda$ , which is also called dark energy. This equation is called Friedmann equation and determines the evolution of scale factor for a given energy density  $\rho$ . The  $(i, j)$  component of Eq. (2.21) gives

$$G_{ij} = \left[ \left( \frac{\dot{a}}{a} \right)^2 + 2\frac{\ddot{a}}{a} + \frac{K}{a^2} \right] g_{ij} = \frac{T_{ij}}{M_{\text{pl}}^2} \quad (2.26)$$

$$= -\frac{P}{M_{\text{pl}}^2} g_{ij}, \quad (2.27)$$

hence

$$\frac{\ddot{a}}{a} = -\frac{1}{6M_{\text{pl}}^2}(\rho + 3P)a. \quad (2.28)$$

This gives the acceleration of the expansion, which is determined by the following equation of state of the dominant energy component in that era:

$$P = w\rho. \quad (2.29)$$

The non-relativistic matter and radiation behave as  $w = 0$ ,  $w = 1/3$ , respectively, and give decelerated expansion. For  $w < -1/3$ , however, the expansion is accelerated, which is the case when the dark energy dominates the universe, since it gives  $w = -1$ .

For a given  $w$ , Eq. (2.25) and Eq. (2.28) can be solved as follows:

$$\rho \propto a^{-3(1+w)}, \quad (2.30)$$

$$a \propto \begin{cases} t^{\frac{2}{3(1+w)}}, & w \neq -1 \\ e^{Ht}, & w = -1 \end{cases} \quad (2.31)$$

where  $H$  is a constant when  $w = -1$ . Here we are neglecting the spatial curvature  $K$ , which will be verified later. Then, from Eq. (2.30), we can see that the energy of the universe is diluted along with the expansion. This is the fastest for the radiation ( $\rho \propto a^{-4}$ ), due to the redshift of the wavelength of the individual photon, while there is no dilution for the dark energy ( $\rho = \text{const.}$ ), due to the effective negative pressure. Thus, the universe experiences the following evolution:

Radiation-dominated era  $\rightarrow$  Matter-dominated era  $\rightarrow$  Dark energy-dominated era,

which is illustrated in Fig. 2.1. As we will see in the following, observations suggest that the present universe is dominated by the dark energy by about 70 %, the rest being mainly the non-relativistic matter.

### 2.1.5 Density parameters

We define the following quantities called density parameters:

$$\Omega_i \equiv \frac{\rho_i}{\rho_{\text{cr}}}. \quad (2.32)$$

These are energy densities that are normalized by the critical density defined as  $\rho_{\text{cr}} \equiv 3H^2 M_{\text{pl}}^2$ , whose value in the present universe is known as  $\rho_{\text{cr},0} = 1.9 \times$



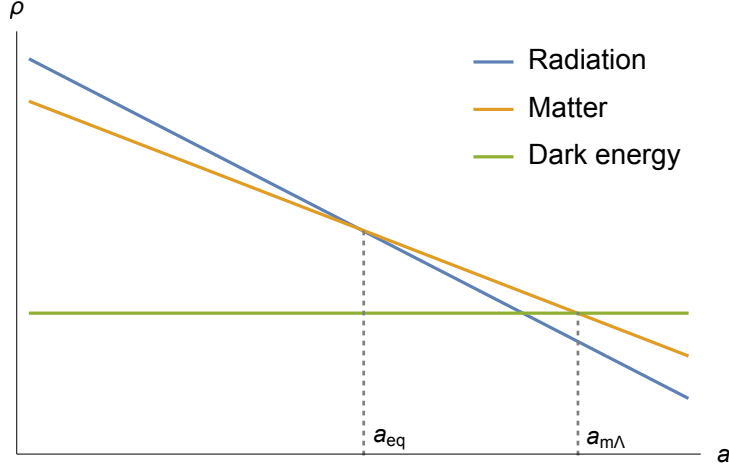


Figure 2.1: Illustration of the evolution of the energy components of the universe. We used  $a_{\text{eq}}$  and  $a_{\text{m}\Lambda}$  as the time of equality between radiation and matter, and matter and dark energy, respectively.

$10^{-29}h^2 \text{ g cm}^{-3} = (3.0 \times 10^{-3} \text{ eV})^4 h^2$  from observations. Using the above density parameters, the Friedmann equation Eq. (2.25) is rewritten as follows:

$$\sum_i \Omega_i + \Omega_\Lambda + \Omega_K = 1, \quad (2.33)$$

where we have defined  $\Omega_K \equiv -K/(a^2 H^2)$ , treating the spatial curvature as an energy component. As previously mentioned, the observations suggest that the present universe is nearly flat:  $\Omega_{K,0} \ll 1$ , and dark energy-dominated, which can be seen from the present values of the density parameters:

$$\Omega_{\Lambda,0} = 0.692 \pm 0.012 \text{ (68\%)}, \quad (2.34)$$

$$\Omega_{\text{m},0} = 0.308 \pm 0.012 \text{ (68\%)}. \quad (2.35)$$

However, from the observation of non-gravitational effects, including baryon acoustic oscillation (BAO), etc., it turned out that the main component of the non-relativistic matter has almost no interaction besides the gravitational interaction, which excludes SM species. This non-interacting matter is called dark matter, whose domination of the matter component can be seen again from the following density parameters:

$$\Omega_{\text{dm},0} h^2 = 0.1186 \pm 0.0020 \text{ (68\%)}, \quad (2.36)$$

$$\Omega_{\text{b},0} h^2 = 0.02226 \pm 0.00023 \text{ (68\%)}, \quad (2.37)$$

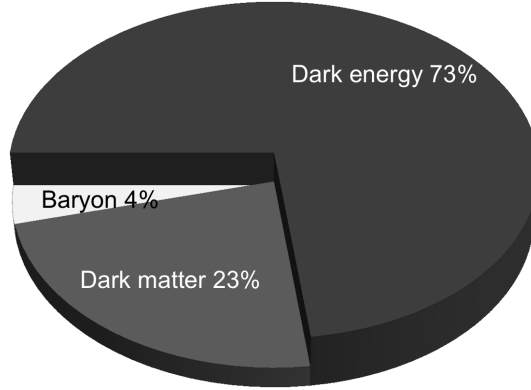


Figure 2.2: Fractions of the energy component in the present universe. We neglected small radiation component.

where  $\Omega_{\text{dm}}$  and  $\Omega_{\text{b}}$  denote the density parameters for the dark matter and the baryonic matter, respectively. We illustrate the fraction of each component in Fig. 2.2. Revealing the identity of the dark matter is one of the biggest problems in modern cosmology.

### 2.1.6 Horizon

It is important in cosmology to know whether the distant two points are causally connected. The maximal distance for the causal connection is bounded from above by the distance the light travels, since any interaction can propagate at most in the speed of light. This upper bound on the causal distance is called horizon.

#### Particle horizon

The maximal distance for the causal relation from the beginning of the universe to the time  $t$  is called particle horizon. This is given by the distance the light traveled until  $t$ , which can be obtained by integrating  $ds^2 = 0$  until  $t$ :

$$d_{\text{p}} \equiv a(t) \int_0^t \frac{dt'}{a(t')}. \quad (2.38)$$

Using Eq. (2.31), this can be calculated for each era of the universe as follows:

$$d_{\text{p}} = \begin{cases} 2t, & \text{Radiation-dominated era} \\ 3t, & \text{Matter-dominated era} \\ H^{-1}(e^{Ht} - 1), & \text{Dark energy-dominated era} \end{cases} \quad (2.39)$$

which increase along with the time.

### Event horizon

The distance the light can travel from the time  $t$  is called event horizon, which again can be obtained through integrating  $ds^2 = 0$  from  $t$  to the infinite future:

$$d_e \equiv a(t) \int_t^\infty \frac{dt'}{a(t')}. \quad (2.40)$$

We can easily find that it diverges for radiation-dominated era and matter-dominated era, which implies that given a sufficient amount of time, the light can travel all over the space. However, in the dark energy-dominated era, it converges to the constant  $H^{-1}$ , which means that for the exponential expansion, the two points more distant than a certain threshold, can never be causally connected. Furthermore, due to the redshift, the originally connected regions cross the horizon in a finite time and become disconnected.

We summarize the event horizon in each era in the following:

$$d_e = \begin{cases} \infty, & \text{Radiation-dominated era} \\ \infty, & \text{Matter-dominated era} \\ H^{-1}. & \text{Dark energy-dominated era} \end{cases} \quad (2.41)$$

### Hubble horizon

There is another useful distance scale related to the horizon given as

$$d_H \equiv H^{-1}, \quad (2.42)$$

which is called Hubble horizon, or Hubble radius. This is the inverse of the Hubble rate and roughly equal to the particle horizon in radiation-dominated era and matter-dominated era, while it is equal to the event horizon in dark energy-dominated era:

$$d_H = H^{-1} = \begin{cases} 2t \sim d_p, & \text{Radiation-dominated era} \\ 3t/2 \sim d_p, & \text{Matter-dominated era} \\ d_e. & \text{Dark energy-dominated era} \end{cases} \quad (2.43)$$

## 2.1.7 Thermal history of the universe

If the interactions among the particles are efficient, they are expected to be in thermal equilibrium. However, as the universe is cooled down due to the expansion,

the interactions become inefficient, which leads to the departure from the equilibrium. This is called decoupling. It is important to know the time when an energy component decouples from thermal equilibrium, in the viewpoint of the evolution of the universe. There is a useful standard, which is called Gamow criterion [30], where we compare an interaction rate  $\Gamma$  to the expansion rate  $H$ , and estimate the time of decoupling as when  $\Gamma < H$ . The equilibrium realizes when  $\Gamma > H$ . In the following, we briefly summarize the thermal history of the universe using the Gamow criterion.

First, we define some thermodynamical variables that will be useful. In thermal equilibrium of temperature  $T$ , the distribution function  $f(p)$  has the form of either Fermi or Bose distribution:

$$f(p) = \frac{1}{e^{(E(p)-\mu)/T} \pm 1}, \quad (2.44)$$

where  $E(p) = \sqrt{p^2 + m^2}$  and  $\mu$  are energy and chemical potential, respectively. Then, the number density, energy density, and pressure of an energy component are given as follows:

$$n = g \int \frac{d^3p}{(2\pi)^3} f(p) \quad (2.45)$$

$$= \frac{g}{2\pi^2} \int dp \frac{p^2}{e^{(E(p)-\mu)/T} \pm 1}, \quad (2.46)$$

$$\rho = g \int \frac{d^3p}{(2\pi)^3} E(p) f(p) \quad (2.47)$$

$$= \frac{g}{2\pi^2} \int dp \frac{p^2 E(p)}{e^{(E(p)-\mu)/T} \pm 1}, \quad (2.48)$$

$$P = g \int \frac{d^3p}{(2\pi)^3} \frac{p^2}{3E(p)} f(p) \quad (2.49)$$

$$= \frac{g}{6\pi^2} \int dp \frac{p^4}{E(p)} \frac{1}{e^{(E(p)-\mu)/T} \pm 1}, \quad (2.50)$$

where  $g$  denotes the degrees of freedom of each particle species. The integrals can be performed in the non-relativistic limit  $m \gg T$  as

$$n \simeq g \left( \frac{mT}{2\pi} \right)^{3/2} e^{-(m-\mu)/T}, \quad (2.51)$$

$$\rho \simeq mn + \frac{3}{2}nT, \quad (2.52)$$

$$P \simeq nT, \quad (2.53)$$

and we especially note that in equilibrium, if the temperature becomes lower than the rest mass of the energy component, its density is exponentially suppressed. On the other hand, the relativistic limit becomes

$$n \simeq g \frac{\zeta(3)}{\pi^2} T^3 \times \begin{cases} 1, & \text{Bosons} \\ 3/4, & \text{Fermions} \end{cases} \quad (2.54)$$

$$\rho \simeq g \frac{\pi^2}{30} T^4 \times \begin{cases} 1, & \text{Bosons} \\ 7/8, & \text{Fermions} \end{cases} \quad (2.55)$$

$$P \simeq \frac{1}{3} \rho, \quad (2.56)$$

where  $\zeta(3) = 1.20206 \dots$ . This especially gives the energy density in the radiation-dominated era as

$$\rho \simeq \frac{\pi^2}{30} \left[ \sum_{\text{bosons}} g_i T_i^4 + \frac{7}{8} \sum_{\text{fermions}} g_i T_i^4 \right] \quad (2.57)$$

$$\equiv \frac{\pi^2}{30} g_* T^4, \quad (2.58)$$

where  $T$  denotes the photon temperature and we defined the following effective degrees of freedom:

$$g_* \equiv \sum_{\text{bosons}} g_i \left( \frac{T_i}{T} \right)^4 + \frac{7}{8} \sum_{\text{fermions}} g_i \left( \frac{T_i}{T} \right)^4. \quad (2.59)$$

This decreases in time since the particles become non-relativistic as the universe cools down. We will discuss this evolution of  $g_*$  later.

The entropy density is given by

$$s = \frac{\rho + P}{T} \quad (2.60)$$

due to the following relation of thermodynamics:

$$TdS = dE + PdV, \quad (2.61)$$

where  $S$  and  $V$  are entropy and volume, respectively. Then, using Eq. (2.55) and Eq. (2.56),  $s$  can be written as

$$s = \frac{2\pi}{45} g_{s*} T^3, \quad (2.62)$$

where we have defined the degrees of freedom for entropy as follows:

$$g_{s*} \equiv \sum_{\text{bosons}} g_i \left( \frac{T_i}{T} \right)^3 + \frac{7}{8} \sum_{\text{fermions}} g_i \left( \frac{T_i}{T} \right)^3. \quad (2.63)$$

We note that the entropy  $a^3 s$  is conserved due to the following continuity equation.

$$\frac{d(a^3 \rho)}{dt} = -P \frac{d(a)}{dt}, \quad (2.64)$$

which is derived from Eq. (2.25) and Eq. (2.28).

In the following, we study the thermal history of the universe, especially comparing various interaction rates  $\Gamma$  with the expansion rate  $H$ , which now we know that is given by

$$H^2 = \frac{\rho}{3M_{\text{pl}}^2} \quad (2.65)$$

$$= \frac{\pi^2}{90M_{\text{pl}}^2} g_* T^4, \quad (2.66)$$

in the radiation-dominated universe.

### Electroweak and QCD phase transition

For a temperature of  $T \gtrsim 300$  GeV, the electroweak symmetry is restored, hence all the SM particle species are massless. They are also in thermal equilibrium and have the same temperature. This gives the following effective degrees of freedom:

$$g_*(T \gtrsim 300 \text{ GeV}) = 2 \times 2 + 8 \times 2 + \frac{7}{8}(6 \times 3 \times 2 \times 2 + 3 \times 2 \times 2 + 3 \times 2) = 106.75, \quad (2.67)$$

where we counted, as bosons, Higgs complex doublet ( $2 \times 2$ ), eight gluons of both polarization ( $8 \times 2$ ), four electroweak gauge bosons of both polarization ( $4 \times 2$ ), and as fermions, six (anti-) quarks of three colors and both spins ( $6 \times 3 \times 2 \times 2$ ), and electron, muon, tau of both spins and their anti-particles ( $3 \times 2 \times 2$ ), and three (anti-) neutrinos ( $3 \times 2$ ).

For  $T \lesssim 100$  GeV, the electroweak symmetry breaking occurs, and  $W^\pm$ ,  $B$ , Higgs boson, and fermions gain masses, which is called electroweak phase transition. Then, for  $T \lesssim 200$  MeV, QCD phase transition occurs, which confines the (anti-)quarks and gluons into baryons and mesons. These hadrons are mostly unstable except protons and neutrons. Most of the other massive particles also have decayed or annihilated, hence the particle species that are present in this

era become protons, neutrons, photons, electrons, positrons, and (anti-) neutrinos. Since these are in thermal equilibrium and have the same temperature, the effective degrees of freedom becomes

$$g_*(1.5 \text{ MeV} \lesssim T \lesssim 200 \text{ GeV}) = 2 + \frac{7}{8}(2 \times 2 + 3 \times 2) = 10.75, \quad (2.68)$$

where we counted photons of both polarization, electron (positron) of both spins, and three (anti-) neutrinos. The protons and neutrons do not contribute since they are non-relativistic. The lower bound of temperature 1.5 MeV is when the neutrinos decouple from the thermal bath, as we will see below.

### Neutrino decoupling

Since neutrinos experience only the weak interaction, they decouple from the equilibrium earlier than other species. The low energy effective theory for weak interaction gives the following cross section:

$$\sigma \sim G_F^2 E^2, \quad (2.69)$$

where  $G_F = 1.17 \times 10^{-5} \text{ GeV}^{-2}$  is the effective coupling constant in the low energy effective theory of weak interaction, which is called Fermi constant. Since the energy  $E$  is about the temperature  $T$ , the interaction rate  $\Gamma$  is given as

$$\Gamma = n\sigma \sim G_F^2 T^5, \quad (2.70)$$

where we used  $n \sim T^3$  (see Eq. (2.54)). Since the Hubble rate  $H$  is given as

$$H^2 = \frac{\pi^2}{90 M_{\text{pl}}^2} g_* T^4, \quad (2.71)$$

we can estimate the decoupling temperature by comparing  $\Gamma$  and  $H$ . If we use  $g_* = 10.75$ , the ratio between  $\Gamma$  and  $H$  is estimated as

$$\frac{\Gamma}{H} \sim \left( \frac{T}{1.5 \text{ MeV}} \right)^3, \quad (2.72)$$

which implies that the neutrinos decouple at the temperature  $T \simeq 1.5 \text{ MeV}$ .

After the decoupling, the momentum distribution of the neutrino is fixed as

$$f_\nu(p) = \frac{1}{e^{p_{\text{dec}}/T_{\text{dec}}} + 1}, \quad (2.73)$$

where  $t_{\text{dec}}$  denotes the time of decoupling. Since the momentum is redshifted as

$$p \propto a^{-1}, \quad (2.74)$$

it can be written as

$$f_\nu(p) = \frac{1}{e^{p/T_\nu} + 1}, \quad (2.75)$$

where  $T_\nu \equiv T_{\text{dec}} a_{\text{dec}}/a$  behaves as the temperature of the neutrinos. Note that  $T_\nu$  is always proportional to  $a^{-1}$  after the decoupling.

### Electron-positron annihilation

When the temperature becomes lower than the electron (positron) mass:  $T \lesssim 0.5$  MeV, the number density of electron-positron pairs dramatically decreases (see Eq. (2.54)), which is called electron-positron annihilation. Then, due to the entropy conservation, this slightly increases the temperature of the radiation. Here, however, the neutrino temperature is unaffected and just redshifts due to the expansion, since the neutrino is already decoupled from the thermal plasma. We estimate this gap in temperature. The effective degrees of freedom for entropy before the pair-annihilation is

$$g_{s*-} = 2 + \frac{7}{8}(2 \times 2 + 3 \times 2) = \frac{43}{4}, \quad (2.76)$$

which is the same as  $g_*$ . The effective degrees of freedom for entropy after the pair-annihilation is given as

$$g_{s*+} = 2 + \frac{7}{8} \times 3 \times 2 \times \left( \frac{T_{\nu+}}{T_+} \right)^3 \quad (2.77)$$

$$= 2 + \frac{21}{4} \left( \frac{T_{\nu+}}{T_+} \right)^3, \quad (2.78)$$

where  $T_+$  and  $T_{\nu+}$  denote photon and neutrino temperature, respectively, after the pair-annihilation. Then, the entropy conservation gives

$$g_{s*+} T_+^3 a_+^3 = g_{s*-} T_-^3 a_-^3, \quad (2.79)$$

while the neutrino temperature just redshifts as

$$T_{\nu+} a_+ = T_{\nu-} a_- \quad (2.80)$$

$$= T_- a_-, \quad (2.81)$$

where we used that the neutrino temperature before the pair-annihilation  $T_{\nu-}$  is the same as the photon temperature  $T_-$ . Combining the above, we obtain the following ratio between the neutrino and photon temperature after the pair-annihilation:

$$\frac{T_{\nu+}}{T_+} = \left( \frac{4}{11} \right)^{1/3}. \quad (2.82)$$



This temperature gap is maintained until the present, and the observational value of the present photon temperature  $T_0 \simeq 2.7$  K gives the present neutrino temperature as  $T_{\nu,0} \simeq 1.9$  K.

## Big Bang Nucleosynthesis

Meanwhile, for  $T \gtrsim 1$  MeV, non-relativistic protons and neutrons are in equilibrium through the following reactions:

$$p + e^- \leftrightarrow n + \nu_e, \quad (2.83)$$

$$p + \bar{\nu}_e \leftrightarrow n + e^+. \quad (2.84)$$

The interaction rate of these reactions is given as

$$\Gamma \sim G_F^2 (1 + 3g_A^2) T^5, \quad (2.85)$$

where  $g_A = 1.26$  is called axial vector coupling, whose value is determined from the neutron decay. If we use  $g_* = 10.75$ , we obtain the ratio between  $\Gamma$  and  $H$  as follows:

$$\frac{\Gamma}{H} \sim \left( \frac{T}{0.83 \text{ MeV}} \right)^3, \quad (2.86)$$

hence, at  $T \sim 0.83$  MeV, the number-changing between protons and neutrons through the above reactions freezes, which fixes the number ratio between protons and neutrons as

$$\frac{n_n}{n_p} \sim e^{-(m_n - m_p - \mu_n + \mu_p)/T} \quad (2.87)$$

$$\sim e^{-(m_n - m_p)/T} \quad (2.88)$$

$$\simeq e^{-1.3 \text{ MeV}/T} \quad (2.89)$$

$$\simeq e^{-1.3/0.83} \quad (2.90)$$

$$\simeq 0.21 \quad (2.91)$$

Here we used  $\mu_n \sim \mu_p$ , which can be verified as follows: Since the number changing processes between the protons and neutrons are in equilibrium, the chemical potentials satisfy the following relation.

$$\mu_p + \mu_e = \mu_n + \mu_{\nu_e}. \quad (2.92)$$

The chemical potentials for the relativistic electrons and neutrinos are given as

$$\frac{\mu_e}{T} \sim \frac{n_{e^-} - n_{e^+}}{T^3} \quad (2.93)$$

$$\sim \frac{n_{e^-} - n_{e^+}}{n_\gamma}, \quad (2.94)$$

$$\frac{\mu_{\nu_e}}{T} \sim \frac{n_{\nu_e} - n_{\bar{\nu}_e}}{T^3} \quad (2.95)$$

$$\sim \frac{n_{\nu_e} - n_{\bar{\nu}_e}}{n_\gamma}, \quad (2.96)$$

where we used  $n_\gamma \sim T^3$ . The assumption of neutrality of the universe gives

$$n_{e^-} - n_{e^+} = n_p, \quad (2.97)$$

which is sufficiently small:  $10^{-9}n_\gamma$ , as we will see just below. If we assume that the asymmetry of the neutrino sector is also small, we obtain

$$\frac{\mu_p - \mu_n}{T} = \frac{-\mu_e + \mu_{\nu_e}}{T} \ll 1, \quad (2.98)$$

which gives  $\mu_n = \mu_p$  in Eq. (2.87). Using Eq. (2.66) and  $H \simeq 1/2t$  in the radiation era, we can translate the temperature  $T \sim 0.83$  MeV into time  $t \sim 1$  sec. On the other hand, the following beta decay of neutron into proton is still efficient,

$$n \rightarrow p + e^- + \bar{\nu}_e, \quad (2.99)$$

which gives the neutron-to-baryon ratio  $X_n$  as

$$X_n(t) \equiv \frac{n_n(t)}{n_p(t) + n_n(t)} \simeq 0.17 e^{-(t-\tau_n)/\tau_n}, \quad (2.100)$$

where  $\tau_n \simeq 886$  sec is the lifetime of the neutron.

The protons and neutrons react to form the deuteron D:

$$p + n \rightarrow D + \gamma, \quad (2.101)$$

which becomes efficient when the temperature becomes lower than the binding energy of the deuteron 2.2 MeV:

$$\frac{n_n n_p}{n_D n_\gamma} \sim \left(\frac{m_p}{T}\right)^{3/2} e^{-(m_n + m_p - m_D)/T}, \quad (2.102)$$

hence

$$\frac{n_D}{n_n} \sim \frac{n_\gamma}{n_p} \left(\frac{T}{m_p}\right)^{3/2} e^{I_D/T}, \quad (2.103)$$

where  $I_D \equiv m_n + m_p - m_D \simeq 2.2$  MeV is the binding energy of the deuteron. Thus, indeed we can see that the deuteron formation becomes efficient for  $T \simeq I_D$ , where the individual photon has not enough energy to dissociate the bound state D. However, since the number density of photons is larger than that of baryons, as we will see below, large number of scatterings may destroy the deuterons, which is appearing as the prefactor  $n_\gamma/n_p$ . Therefore, the more accurate formation temperature becomes the lower value 0.06 MeV. This is translated into the formation time  $t_D \simeq 200$  sec. The formation of deuterons triggers the nucleosynthesis of heavier elements and they are mainly absorbed into  ${}^4\text{He}$ , whose mass ratio to baryons are estimated as follows:

$$Y({}^4\text{He}) = \frac{4m_p \times n_n/2}{m_p n_p + m_n n_n} \quad (2.104)$$

$$\simeq \frac{2X_n(t_D)}{1 + X_n(t_D)} \quad (2.105)$$

$$\simeq 0.25 \quad (2.106)$$

which is known to coincide with the more accurate numerical results. This production of light elements from  $T \sim 1$  MeV to  $T \sim 0.01$  MeV is called big bang nucleosynthesis (BBN).

The abundance of each element depends on the baryon-to-photon ratio  $\eta \equiv n_b/n_\gamma$ , and the observations suggest that

$$\eta \simeq 6 \times 10^{-10}, \quad (2.107)$$

as shown in Fig. 2.3, which implies the redundancy of matter to anti-matter in the early universe. Finding the origin of this asymmetry is called baryogenesis, which is one of the most crucial tasks of modern cosmology.

We also see from the figure that the  ${}^7\text{Li}$  abundance is not explained well, which leads to another serious cosmological problem, called ‘‘Lithium problem’’.

## Radiation-Matter equality

Since we know the present density parameters, we can calculate the history of each energy component, especially when the matter component begins to dominate over the radiation:

$$a_{\text{eq}} = \frac{\rho_{r,0}}{\rho_{m,0}} \quad (2.108)$$

$$= \frac{\Omega_{r,0}}{\Omega_{m,0}} \quad (2.109)$$

$$\simeq 3.1 \times 10^{-4}. \quad (2.110)$$

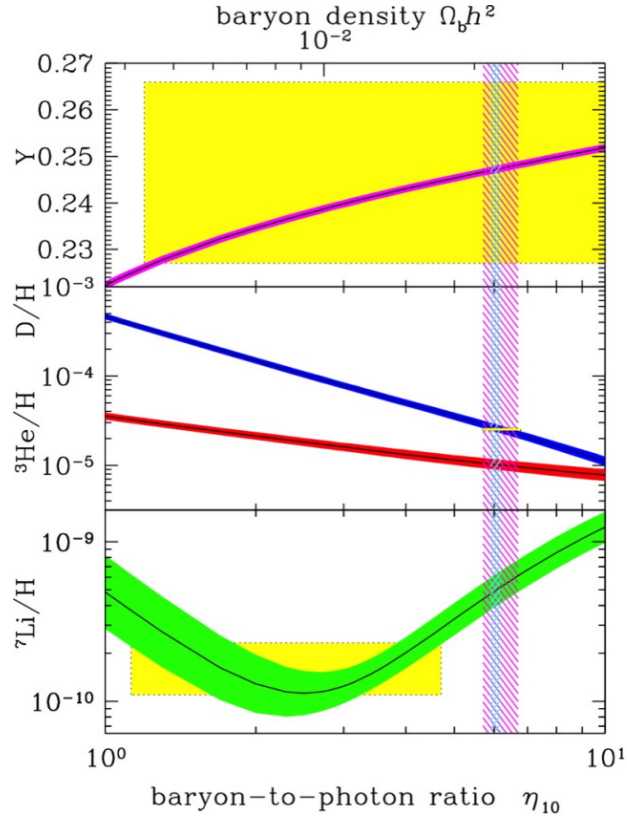


Figure 2.3: The predicted abundances of several elements. The yellow bands denote 95% CL range of observed abundances [31].

This leads to the following redshift.

$$z_{\text{eq}} = \frac{1}{a_{\text{eq}}} - 1 \quad (2.111)$$

$$\simeq 3200, \quad (2.112)$$

corresponding to the temperature,

$$T_{\text{eq}} = (1 + z_{\text{eq}})T_0 \quad (2.113)$$

$$\simeq 8600 \text{ K} \quad (2.114)$$

$$\simeq 0.74 \text{ eV}, \quad (2.115)$$

where we used the present temperature  $T_0 \simeq 2.7 \text{ K}$ .

## Recombination and photon decoupling

The protons and electrons form the hydrogens:

$$p + e \leftrightarrow H + \gamma \quad (2.116)$$

which becomes efficient when the temperature becomes lower than the binding energy of the hydrogen 13.6 eV. Here again, the more accurate temperature becomes the lower value 0.3 eV ( $z \simeq 1100$ ), since a large number of photons ionize the bound state H. This is called recombination. The abundance during the recombination can be described by the following equation:

$$\frac{n_e n_p}{n_H n_\gamma} \simeq \frac{\sqrt{\pi}}{4\sqrt{2}\zeta(3)} \left(\frac{m_e}{T}\right)^{3/2} e^{-I_H/T}, \quad (2.117)$$

where  $I_H \equiv m_e + m_p - m_H \simeq 13.6$  eV is the binding energy of the hydrogen. Here we are interested in the decreasing free-electron numbers, instead of the increasing hydrogen numbers. Using  $X_e \equiv n_e/n_b \sim n_p/n_b$  and  $n_p + n_H = n_b$ , the above equation reduces to

$$\frac{1 - X_e}{X_e^2} = \frac{4\sqrt{2}\zeta(3)}{\sqrt{\pi}} \eta \left(\frac{T}{m_e}\right)^{3/2} e^{I_H/T}, \quad (2.118)$$

which gives the following solution for  $X_e$ :

$$X_e = 2 \left[ 1 + \sqrt{1 + \frac{16\sqrt{2}\zeta(3)}{\sqrt{\pi}} \eta \left(\frac{T}{m_e}\right)^{3/2} e^{I_H/T}} \right]^{-1}. \quad (2.119)$$

Using  $T = T_0(1 + z)$ , we plot  $X_e$  as a function of  $z$  in Fig. 2.4, where we can see the drastic decrease of the free electron numbers at  $z \sim 1300$ , which is indeed  $T \simeq 0.3$  eV. The decrease of the free electrons is important, since it makes the Thomson scattering between photons and electrons inefficient. Here we estimate the decoupling temperature of the Thomson scattering: Using the Thomson cross section

$$\sigma_T = \frac{8\pi\alpha^2}{3m_e^2}, \quad (2.120)$$

with  $\alpha \simeq 1/137$  the fine structure constant, The interaction rate of the Thomson scattering is given as follows:

$$\Gamma_T = n_e \sigma_T \quad (2.121)$$

$$= X_e \frac{\rho_b}{m_p} \frac{8\pi\alpha^2}{3m_e^2}. \quad (2.122)$$

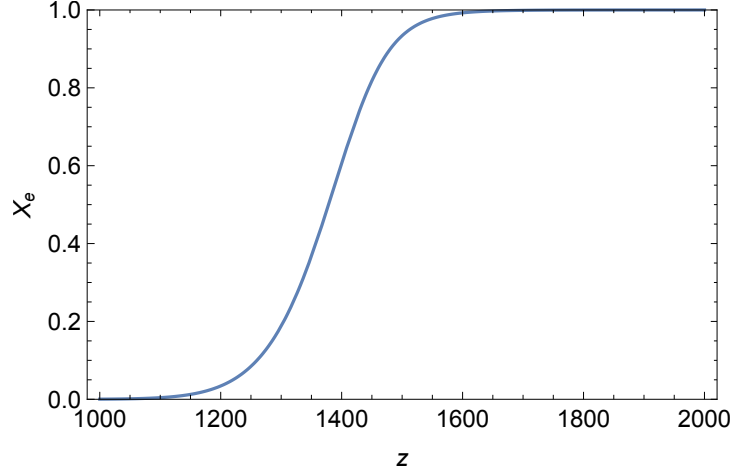


Figure 2.4:  $X_e$  as a function of  $z$ . We can see the drastic decrease at  $z \sim 1300$ .

Then the ratio to the Hubble rate  $H = \sqrt{\rho_m/3M_{\text{pl}}^2}$  becomes

$$\frac{\Gamma_T}{H} = X_e \frac{\rho_b}{m_p} \frac{8\pi\alpha^2}{3m_e^2} \left( \frac{3M_{\text{pl}}^2}{\rho_m} \right)^{1/2} \quad (2.123)$$

$$= \rho_{\text{cr},0}^{1/2} (1+z)^{3/2} X_e \frac{\Omega_{b,0}}{m_p} \frac{8\pi\alpha^2}{3m_e^2} \left( \frac{3M_{\text{pl}}^2}{\Omega_{m,0}} \right)^{1/2}. \quad (2.124)$$

Plugging in the numerical factors, we obtain the decoupling redshift  $z_{\text{dec}} \sim 1100$ , or the decoupling temperature  $T_{\text{dec}} \sim 3000 \text{ K} \simeq 0.26 \text{ eV}$ , which is just after the recombination. The decoupled photons stream freely towards the observer since the last scattering. These free-streaming photons are called Cosmic Microwave Background (CMB), whose observation is important since it gives various cosmological information on, such as density parameters, the origin of the large scale structure, astrophysical events after the last scattering, and so on.

### Matter-Dark energy equality

Since the present universe is dominated by dark energy, the transition from the matter era must have occurred, which again can be estimated from the present

density parameters as follows:

$$a_{\text{m}\Lambda} = \left( \frac{\rho_{\text{m},0}}{\rho_{\Lambda,0}} \right)^{1/3} \quad (2.125)$$

$$= \left( \frac{\Omega_{\text{m},0}}{\Omega_{\Lambda,0}} \right)^{1/3} \quad (2.126)$$

$$\simeq 0.72 \quad (2.127)$$

or

$$z_{\text{m}\Lambda} = \frac{1}{a_{\text{m}\Lambda}} - 1 \quad (2.128)$$

$$\simeq 0.38 \quad (2.129)$$

in terms of the redshift. The corresponding temperature becomes

$$T_{\text{m}\Lambda} = (1 + z_{\text{m}\Lambda})T_0 \quad (2.130)$$

$$\simeq 3.8 \text{ K}, \quad (2.131)$$

where again we used the present temperature  $T_0 \simeq 2.7 \text{ K}$ .

## 2.2 Perturbed universe

In the previous section, we studied the evolution of the expanding universe, which is assumed to be homogeneous and isotropic. However, its fluctuation is also important since it drives the structure formation of the universe. In this section, we solve the evolution of this fluctuation in the linear regime.

### 2.2.1 Linear perturbations

We consider the following linear perturbations around the nearly flat FRW metric:

$$ds^2 = (1 + 2A)dt^2 - 2a(\partial_i B - S_i)dt dx^i - a^2 [(1 - 2\psi)\delta_{ij} + 2\partial_i \partial_j E + \partial_i F_j + \partial_j F_i + h_{ij}] dx^i dx^j, \quad (2.132)$$

where we decomposed the perturbations into scalar, vector, and tensor modes, which satisfy  $\partial_i S_i = \partial_i F_i = \partial_i h_{ij} = h_{ii} = 0$ . The perturbation  $\psi$  is called curvature perturbation since it induces the spatial curvature:  $R^{(d=3)} \simeq -4\Delta\psi/a^2$ .

The perturbations behave differently in the different coordinate systems, and proper coordinate transformation can greatly simplify the geometry. Here we derive the transforming properties of the perturbations under the coordinate transformation, which is also called gauge transformation. The metric transforms as

$$\tilde{g}_{\mu\nu}(\tilde{x}) = \frac{\partial x^\alpha}{\partial \tilde{x}^\mu} \frac{\partial x^\beta}{\partial \tilde{x}^\nu} g_{\alpha\beta}(x), \quad (2.133)$$

under the coordinate transformation  $x^\mu \rightarrow \tilde{x}^\mu = x^\mu + \xi^\mu$ . Since the universe must reduce to the FRW metric without the perturbation,  $\xi^\mu$  must be of the same order as the perturbations. Then, we can expand the above transformation in the leading order of  $\xi^\mu$ :

$$\tilde{g}_{\mu\nu}(x) = \frac{\partial(x - \xi)^\alpha}{\partial\tilde{x}^\mu} \frac{\partial(x - \xi)^\beta}{\partial\tilde{x}^\nu} g_{\alpha\beta}(x - \xi) \quad (2.134)$$

$$= g_{\mu\nu}(x) - \frac{\partial\xi^\alpha}{\partial x^\mu} g_{\alpha\nu}(x) - \frac{\partial\xi^\beta}{\partial x^\nu} g_{\mu\beta}(x) - \frac{\partial g_{\mu\nu}(x)}{\partial x^\alpha} \xi^\alpha. \quad (2.135)$$

Here if we decompose  $\xi^\mu$  as  $\xi^\mu = (T, \delta^{ij}\partial_j L + L^i)$  with  $\partial_i L_i = 0$ , the transformation is also decomposed as

$$\tilde{A} = A - \dot{T}, \quad (2.136)$$

$$\tilde{B} = B - a\dot{L} + a^{-1}T, \quad (2.137)$$

$$\tilde{S}_i = S_i + a\delta_{ij}\dot{L}^j, \quad (2.138)$$

$$\tilde{\psi} = \psi + HT, \quad (2.139)$$

$$\tilde{E} = E - L, \quad (2.140)$$

$$\tilde{F}_i = F_i - \delta_{ij}L^j, \quad (2.141)$$

$$\tilde{h}_{ij} = h_{ij}. \quad (2.142)$$

We must also take into account the fluctuations of the energy-momentum tensor  $T_{\mu\nu}$ . We perturb the following perfect fluid form

$$T_{\mu\nu} = -Pg_{\mu\nu} + (\rho + P)u_\mu u_\nu, \quad (2.143)$$

as

$$\rho = \bar{\rho} + \delta\rho, \quad (2.144)$$

$$P = \bar{P} + \delta P, \quad (2.145)$$

$$u^\mu = \bar{u}^\mu + \delta u^\mu, \quad (2.146)$$

where the bar denotes the background. Since the four-velocity  $u^\mu$  satisfies  $g^{\mu\nu}u_\mu u_\nu = 1$ , we obtain the following relation:

$$\delta u_0 = \frac{1}{2}\delta g_{00} \quad (2.147)$$

$$= -\frac{1}{2}\delta g^{00}, \quad (2.148)$$



where we used  $\delta g^{\mu\nu} = -\bar{g}^{\mu\alpha}\delta g_{\alpha\beta}\bar{g}^{\beta\nu}$ . Then, the perturbations of Eq. (2.143) are given as

$$\delta T_{00} = \delta\rho + \bar{\rho}\delta g_{00}, \quad (2.149)$$

$$\delta T_{0i} = \delta T_{i0} = -\bar{P}\delta g_{i0} + (\bar{\rho} + \bar{P})\delta u_i, \quad (2.150)$$

$$\delta T_{ij} = -\bar{P}\delta g_{ij} + a^2\delta_{ij}\delta P. \quad (2.151)$$

Besides this perturbation of the perfect fluid form, we must also take into account the deviation from the perfect fluid, which is given by the anisotropic stress tensor  $\pi_{ij}$ . Then, decomposing  $\delta u_i$  and  $\pi_{ij}$  as scalar, vector, and tensor mode, we obtain

$$\delta T_{00} = \delta\rho + \bar{\rho}\delta g_{00}, \quad (2.152)$$

$$\delta T_{0i} = \delta T_{i0} = -\bar{P}\delta g_{i0} + (\bar{\rho} + \bar{P})(\partial_i\delta u^S + \delta u_i^V), \quad (2.153)$$

$$\delta T_{ij} = -\bar{P}\delta g_{ij} + a^2 \left[ \delta_{ij}\delta P + (\partial_i\partial_j - \frac{1}{3}\delta_{ij}\Delta)\pi^S + \partial_i\pi_j^V + \partial_j\pi_i^V + \pi_{ij}^T \right], \quad (2.154)$$

where  $\partial_i\delta u_i^V = \partial_i\pi_i^V = \partial_i\pi_{ij}^T = \pi_{ii}^T = 0$  holds. The gauge transformation of  $T_{\mu\nu}$  is given as follows:

$$\tilde{T}_{\mu\nu}(x) = T_{\mu\nu}(x) - \frac{\partial\xi^\alpha}{\partial x^\mu}T_{\alpha\nu}(x) - \frac{\partial\xi^\beta}{\partial x^\nu}T_{\mu\beta}(x) - \frac{\partial T_{\mu\nu}(x)}{\partial x^\alpha}\xi^\alpha, \quad (2.155)$$

at the leading order of  $\xi^\mu$ , which is again decomposed as

$$\delta\tilde{T}_{00} = \delta T_{00} - 2\bar{\rho}\dot{T} - \dot{\rho}T, \quad (2.156)$$

$$\delta\tilde{T}_{0i} = \delta\tilde{T}_{i0} = \delta T_{0i} = a^2\bar{P}(\partial_i\dot{L} + \delta_{ij}\dot{L}^j) - \bar{\rho}\partial_iT, \quad (2.157)$$

$$\delta\tilde{T}_{ij} = \delta T_{ij} - a^2\bar{P}(2\partial_i\partial_jL + \partial_i\delta_{jk}L^k + \partial_j\delta_{ik}L^k) - a^2T\delta_{ij}(2H + \dot{\bar{P}}). \quad (2.158)$$

This in turn gives the following transformation rules for  $\delta\rho$ ,  $\delta P$ ,  $\delta u^\mu$ , and  $\pi_{ij}$ .

$$\delta\tilde{\rho} = \delta\rho - \dot{\rho}T, \quad (2.159)$$

$$\delta\tilde{P} = \delta P - \dot{\bar{P}}T, \quad (2.160)$$

$$\delta\tilde{u}^S = \delta u^S - T, \quad (2.161)$$

$$\delta\tilde{u}^V = \delta u_i^V, \quad (2.162)$$

$$\delta\tilde{\pi}^S = \pi^S, \quad (2.163)$$

$$\delta\tilde{\pi}_i^V = \pi_i^V, \quad (2.164)$$

$$\delta\tilde{\pi}_{ij}^T = \pi_{ij}^T. \quad (2.165)$$

Now we define several gauge invariants that will be useful in various contexts. The following gauge invariants, called Bardeen potentials, are frequently used:

$$\Phi \equiv A - \frac{d}{dt} \left[ a^2 \left( \dot{E} - \frac{B}{a} \right) \right] = A|_{E=B=0}, \quad (2.166)$$

$$\Psi \equiv \psi + a^2 H \left( \dot{E} - \frac{B}{a} \right) = \psi|_{E=B=0}. \quad (2.167)$$

The gauge invariants can also be constructed from the energy-momentum tensor. For instance, the following quantity is gauge invariant:

$$\delta P_{\text{nad}} \equiv \delta P - \frac{\dot{\bar{P}}}{\bar{\rho}} \delta \rho, \quad (2.168)$$

which is called non-adiabatic pressure perturbation, since it is the deviation from the adiabatic pressure perturbation:

$$\delta P_{\text{ad}} \equiv \frac{\dot{\bar{P}}}{\bar{\rho}} \delta \rho. \quad (2.169)$$

Here we define the following quantity:

$$\delta q \equiv -(\bar{\rho} + \bar{P}) \delta u^S, \quad (2.170)$$

which is called momentum transfer potential since  $\delta T_i^0 = -\partial_i \delta q$ . Then we can define the following gauge invariant.

$$\delta \rho_c \equiv \delta \rho - 3H \delta q = \delta \rho|_{\delta q=0}, \quad (2.171)$$

which is the density perturbation for comoving gauge ( $\delta q = 0$ ). Finally, we define the most frequently used quantities:

$$\zeta \equiv -\psi - \frac{H}{\bar{\rho}} \delta \rho = -\psi|_{\delta \rho=0}, \quad (2.172)$$

$$\mathcal{R}_c \equiv \psi - \frac{H}{\bar{\rho} + \bar{P}} \delta q = \psi|_{\delta q=0} = -\zeta - \frac{H}{\bar{\rho}} \delta \rho_c, \quad (2.173)$$

which are curvature perturbations for uniform density gauge ( $\delta \rho = 0$ ) and comoving gauge, respectively. The initial condition of the curvature perturbation will be of interest, whose generation will be discussed in the next chapter.

### 2.2.2 Evolution of the fluctuations

The evolution of the fluctuations defined above is governed by the following Einstein equation:

$$\delta G_{\mu\nu} = \frac{\delta T_{\mu\nu}}{M_{\text{pl}}^2}. \quad (2.174)$$

The  $(0, 0)$  and  $(0, i)$  components give

$$3H(\dot{\psi} + HA) - \frac{1}{a^2}\Delta \left[ \psi + a^2 H \left( \dot{E} - \frac{B}{a} \right) \right] = -\frac{\delta\rho}{2M_{\text{pl}}^2}, \quad (2.175)$$

and

$$\dot{\psi} + HA = -\frac{1}{2M_{\text{pl}}^2}\delta q, \quad (2.176)$$

respectively, whose combination gives the following Poisson equation:

$$\frac{1}{a^2}\Delta\Psi = \frac{\delta\rho_c}{2M_{\text{pl}}^2} \quad (2.177)$$

The  $(i, j)$  component is decomposed as the terms proportional to  $\delta_{ij}$  and  $\partial_i\partial_j$ , respectively, and their combinations give

$$\ddot{\psi} + 3H\dot{\psi} + H\dot{A} + (3H^2 + 2\dot{H})A = \frac{1}{2M_{\text{pl}}^2} \left( \delta P + \frac{2}{3}\Delta\pi^{\text{S}} \right), \quad (2.178)$$

$$\frac{d}{dt} \left( \dot{E} - \frac{B}{a} \right) + 3H \left( \dot{E} - \frac{B}{a} \right) + \frac{\psi - A}{a^2} = \frac{\pi^{\text{S}}}{M_{\text{pl}}^2}. \quad (2.179)$$

The latter can be rewritten as

$$\Psi - \Phi = \frac{a^2\pi^{\text{S}}}{M_{\text{pl}}^2}, \quad (2.180)$$

using the Bardeen potentials  $\Psi$  and  $\Phi$ , which especially gives  $\Psi = \Phi$  in absence of anisotropic stress tensor.

The energy conservation condition is given by

$$\dot{\delta\rho} + 3H(\delta\rho + \delta P) = -\frac{1}{a^2}\Delta\delta q + (\bar{\rho} + \bar{P}) \left[ 3\dot{\psi} - \Delta \left( \dot{E} - \frac{B}{a} \right) \right], \quad (2.181)$$

which can be written by the gauge invariants as follows:

$$\dot{\zeta} = -H \frac{\delta P_{\text{nad}}}{\bar{\rho} + \bar{P}} - \Sigma, \quad (2.182)$$

where we defined  $\Sigma$  as

$$\Sigma \equiv \frac{1}{3a^2 H^2} \Delta \left[ \zeta + \left( 1 - \frac{2\bar{\rho}}{9(\bar{\rho} + \bar{P})} \frac{1}{a^2 H^2} \Delta \right) \Psi \right]. \quad (2.183)$$

This implies that if the perturbation is adiabatic, the curvature perturbation is conserved for superhorizon mode:  $k \ll aH$ . This point will be important in the context of the generation of the initial perturbation in the next chapter. If we use the Poisson equation Eq. (2.177), the curvature perturbation  $\mathcal{R}_c$  given by Eq. (2.173) reduces to

$$\mathcal{R}_c = -\zeta + \frac{2\bar{\rho}}{9(\bar{\rho} + \bar{P})} \frac{1}{a^2 H^2} \Delta \Psi, \quad (2.184)$$

which becomes equal to  $-\zeta$  for superhorizon mode  $k \ll aH$ .

The evolution of the vector mode is governed by  $(0, i)$  component of the Einstein equation:

$$-\Delta \left( \dot{F}_i + \frac{S_i}{a} \right) = \frac{2}{M_{\text{pl}}^2} \delta q_i, \quad (2.185)$$

where defined  $\delta q_i \equiv -(\bar{\rho} + \bar{P}) \delta u_i^V$ . Combining this with the  $(i, j)$  components, the following equation is obtained:

$$\delta \dot{q}_i + 3H \delta q_i = -\Delta \pi_i^V, \quad (2.186)$$

which gives

$$\delta q_i \propto a^{-3}, \quad (2.187)$$

in absence of the source  $\pi_i^V$ . This implies that if there is no anisotropic stress tensor  $\pi_i^V$ , the vector mode of the perturbations damps quickly even if it is initially generated. Therefore, the vector mode is usually neglected in the cosmological context.

The tensor mode in the  $(i, j)$  component of Einstein equation gives the following equation:

$$\ddot{h}_{ij} + 3H \dot{h}_{ij} - \frac{1}{a^2} \Delta h_{ij} = \frac{2}{M_{\text{pl}}^2} \pi_{ij}^T \quad (2.188)$$

This is the equation of gravitational wave, whose source is the tensor mode of the anisotropic stress tensor. Without the source, it just propagates throughout the space and especially becomes constant for superhorizon mode  $k \ll aH$ .

# Chapter 3

## Inflationary universe

In the previous chapter, we summarized the main topics of the standard cosmology, where the nearly homogeneous isotropic universe is considered, and its evolution is mainly governed by decelerated expansion driven by SM particles. However, there are some issues that cannot be explained by this framework. In this chapter, we review the problems of standard cosmology and show that these can be solved by assuming the era of accelerated expansion, which is called inflation era, before the standard radiation era dominated by the SM particles. We will see that this inflation era is realized by introducing a hypothetical scalar particle, called inflaton, whose classical dynamics gives an effective cosmological constant, which drives an exponential expansion (see Eq. (2.31)).

### 3.1 Problems of standard cosmology

In this section, we summarize some problems that are difficult to explain by the standard cosmology, and show that they can be naturally explained by introducing an accelerated expansion era, or inflation era, before the radiation domination.

#### 3.1.1 Flatness problem

In the previous chapter, we mentioned on the unnatural flatness of the universe, that is, the spatial curvature  $K$  of the universe is almost zero. This can be stated in a more specific way. If we define the quantity called density parameter as  $\Omega_i(t) \equiv \rho_i(t)/(3H^2 M_{\text{pl}}^2)$ , The Friedmann equation can be written in the following form:

$$\Omega_i(t) + \frac{K}{a^2 H^2} = 1. \quad (3.1)$$

Here if we also define  $\Omega_K(t) \equiv -K/(a^2 H^2)$ , the curvature can also be treated as an energy component, and the observations suggest that this curvature energy in the present universe is about  $|\Omega_K(t_0)| \lesssim 0.01$ , which implies nearly flat universe.  $\Omega_K(t)$  increases as the universe expands, since

$$\frac{1}{a^2 H^2} \propto \begin{cases} t, & \text{Radiation-dominated era} \\ t^{2/3}, & \text{Matter-dominated era} \end{cases} \quad (3.2)$$

Thus the universe must be flatter in the past, which for example, becomes

$$|\Omega_K(t_{\text{BBN}})| \lesssim \mathcal{O}(10^{-16}), \quad (3.3)$$

at the time of BBN. This implies that we need an unnatural tuning of the parameters in the early universe in order to explain the flatness of the universe, which is called the flatness problem.

### 3.1.2 Horizon problem

The present CMB temperature is observed to be  $T_0 \sim 2.7$  K, which is nearly homogeneous and isotropic. On the other hand, the horizon at the time of photon decoupling is given as

$$d_p \sim H_0^{-1}(1 + z_{\text{dec}})^{-3/2}. \quad (3.4)$$

If we use the following distance the photon traveled to earth since the last scattering,

$$d_A \sim H_0^{-1}(1 + z_{\text{dec}})^{-1}, \quad (3.5)$$

the horizon size becomes

$$d_p \sim 1.6^\circ \times d_A. \quad (3.6)$$

This implies that only angular range of  $1.6^\circ$  of the last scattering surface was causally connected, while the observations suggest that the whole surface is synchronized into nearly the same temperature. This is called the horizon problem.

### 3.1.3 Monopole problem

The SM gauge group  $SU(3) \times SU(2) \times U(1)$  is expected to realize through the breaking of a larger group, whose breaking scale is usually set to  $T \sim 10^{16}$  GeV. Then, it is known that the different vacua in space lead to the formation of magnetic monopoles, which are topological defects. More than  $\mathcal{O}(1)$  monopoles are

expected to be formed in each horizon at that era, which gives the following number density at the formation:

$$n_M \gtrsim H_f^3 \sim \frac{T^6}{M_{\text{pl}}^3}, \quad (3.7)$$

and its ratio to photon number density becomes

$$\frac{n_M}{n_\gamma} \gtrsim \left( \frac{T}{M_{\text{pl}}} \right)^3 \sim 10^{-6}, \quad (3.8)$$

where we used  $n_\gamma \sim T^3$  and  $T \sim 10^{16}$  GeV. If the monopoles are stable, this ratio becomes constant, which means that the monopoles exist more than baryons ( $n_b/n_\gamma \sim 10^{-9}$ ). This contradicts the non-detection of the monopoles, which is called monopole problem.

### 3.1.4 Gravitino problem

The supersymmetry (SUSY) is the symmetry between bosons and fermions, e.g.,

$$g \text{ (gluon)} \leftrightarrow \tilde{g} \text{ (gluino)} \quad (3.9)$$

$$\gamma \text{ (photon)} \leftrightarrow \tilde{\gamma} \text{ (photino)} \quad (3.10)$$

$$q \text{ (quark)} \leftrightarrow \tilde{q} \text{ (squark)} \quad (3.11)$$

$$e \text{ (electron)} \leftrightarrow \tilde{e} \text{ (selectron)} \quad (3.12)$$

and the gravitino is defined as the partner of the graviton as follows.

$$g_{\mu\nu} \text{ (graviton)} \leftrightarrow \psi_\mu \text{ (gravitino)}. \quad (3.13)$$

The gravitinos are expected to be in the equilibrium in the Planck era, whose number density becomes

$$n_{3/2} \sim n_\gamma \sim T^3. \quad (3.14)$$

The gravitinos have a long lifetime given as

$$\tau_{3/2} \sim 10^5 \text{ sec} \times \left( \frac{m_{3/2}}{1 \text{ TeV}} \right)^{-3}, \quad (3.15)$$

since they have only gravitational interactions. Thus, the radiation is significantly diluted until the decay of the gravitinos:

$$\frac{\rho_{3/2}}{\rho_\gamma} \sim \frac{m_{3/2} n_{3/2}}{T_d^4} \quad (3.16)$$

$$\sim \frac{m_{3/2}}{T_d} \quad (3.17)$$

$$\sim 10^9 \times \left( \frac{m_{3/2}}{1 \text{ TeV}} \right) \quad (3.18)$$

$$\gg 1. \quad (3.19)$$

This implies the large entropy production through the decay of the gravitinos, which especially dilutes the baryon number density. This contradicts the observations and is called gravitino problem.

### 3.1.5 Solution through accelerated expansion

Here we show that the above problems can be solved by assuming the accelerated expansion driven by some kind of cosmological constant, which we call inflation, before the radiation-dominated universe.

First, we can see that  $|\Omega_K(t)|$  decreases during inflation since

$$\frac{1}{a^2 H^2} \propto e^{-2Ht}, \quad (3.20)$$

where  $H$  is a constant. This implies that even if  $|\Omega_K(t)| \sim \mathcal{O}(1)$  before the inflation, the inflation can decrease it and naturally flatten the universe.

Due to the exponential expansion, the distance the light travels is also stretched exponentially, which naturally explains the reason why the distant points at the photon decoupling could be causally connected in the past.

Finally, the inflation can also solve the monopole and gravitino problem, since the exponential expansion leads to the significant dilution of any density compared to the entropy density produced after inflation.

Hence, we see that the problems of the standard cosmology mentioned above can be solved by introducing the inflation era before the radiation-domination. Interestingly, it is known that these problems are solved by assuming nearly the same duration of the inflation:  $N \gtrsim 60$ , where  $N$  is e-folding number defined as  $N \equiv \ln(a_f/a_i)$ , with  $a_i$  ( $a_f$ ) the scale factors at the beginning (end) of inflation.

We add a comment on the gravitino problem: While the gravitino density is diluted by the inflation, they are actually produced again by the thermal plasma after inflation, through the following process, for instance:

$$q + \bar{q} \rightarrow \tilde{g} + \psi_\mu. \quad (3.21)$$

whose Feynman diagram is illustrated in Fig. 3.1. The number density of thermally produced gravitinos is given as

$$n_{3/2} \sim \frac{n_q^2 \sigma}{H} \quad (3.22)$$

$$\sim \frac{T^4}{M_{\text{pl}}}, \quad (3.23)$$



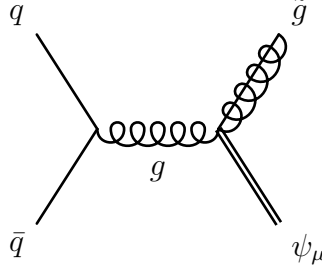


Figure 3.1: A diagram for gravitino production.

where we used  $n_q \sim T^3$  and assumed the cross section as  $\sigma \sim 1/M_{\text{pl}}^2$ . Then the energy ratio at the decay of the gravitinos becomes

$$\frac{\rho_{3/2}}{\rho_\gamma} \sim \frac{m_{3/2} n_{3/2}}{T_{\text{d}} n_\gamma} \quad (3.24)$$

$$\sim \left( \frac{m_{3/2}}{1 \text{ TeV}} \right) \left( \frac{T}{10^{10} \text{ GeV}} \right), \quad (3.25)$$

which implies that the temperature smaller than about  $10^{10}$  GeV is required to avoid the large entropy production. In addition, the radiation produced from the gravitino decay may dissociate the light elements at BBN, which gives a stronger constraint on the temperature:

$$T \lesssim 10^6 \text{ GeV}, \quad (3.26)$$

for  $100 \text{ GeV} \lesssim m_{3/2} \lesssim 40 \text{ TeV}$  (Fig. 3.2).

## 3.2 Slow-roll inflation

In the previous section, we saw that inflation can solve the problems of the standard cosmology. However, this kind of expansion needs an effective cosmological constant, which is difficult to realize using the ordinary SM particles. In this section, we show that the inflation can be realized through the dynamics of a hypothetical scalar field, inflaton. In order to obtain an effective cosmological constant, we slowly roll down the inflaton from a flat potential, whose height then plays the role of the cosmological constant.

We consider the following action:

$$S = \int d^4x \sqrt{-g} \left[ \frac{1}{2} g^{\mu\nu} \partial_\mu \phi \partial_\nu \phi - V(\phi) \right], \quad (3.27)$$

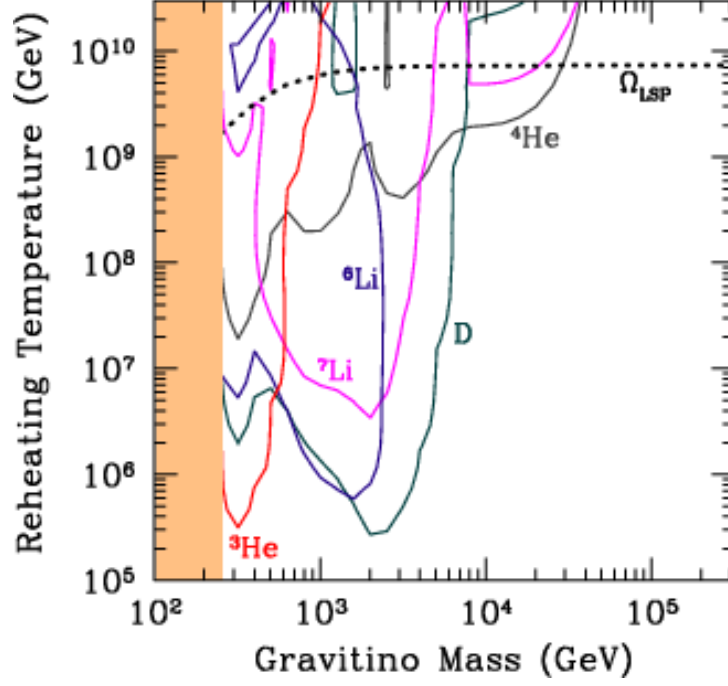


Figure 3.2: Constraint on the temperature from BBN [32].

where the real scalar  $\phi$  denotes the inflaton. Then, the equation of motion is given as

$$\ddot{\phi} + 3H\dot{\phi} + V'(\phi) = 0. \quad (3.28)$$

The energy-momentum tensor is written as

$$T_{\mu\nu} = \frac{2}{\sqrt{-g}} \frac{\delta S}{\delta g^{\mu\nu}} = \partial_\mu \phi \partial_\nu \phi - g_{\mu\nu} \left[ \frac{1}{2} g^{\rho\sigma} \partial_\rho \phi \partial_\sigma \phi - V(\phi) \right], \quad (3.29)$$

which gives the following energy density and pressure:

$$\rho = \frac{1}{2} \dot{\phi}^2 + V(\phi), \quad (3.30)$$

$$p = \frac{1}{2} \dot{\phi}^2 - V(\phi). \quad (3.31)$$

Thus, in order to realize the inflation, which is when  $\rho \simeq -p$ , the kinetic energy needs to be smaller than the potential energy, which means that  $\phi$  needs to roll down the potential slowly enough. This can be described by the following slow-roll conditions:

$$\dot{\phi}^2 \ll V(\phi), \quad (3.32)$$

$$3H\dot{\phi} \sim -V'(\phi). \quad (3.33)$$

The first condition is that the velocity of  $\phi$  is sufficiently slow, and the second states that  $\phi$  maintains to be slow for a sufficiently long time due to the Hubble friction. If we define the following slow-roll parameters,

$$\epsilon \equiv \frac{M_{\text{pl}}^2}{2} \left( \frac{V'}{V} \right)^2, \quad (3.34)$$

$$\eta \equiv M_{\text{pl}}^2 \frac{V''}{V}, \quad (3.35)$$

the above slow-roll conditions reduce to those on the slow-roll parameters as follows:

$$\epsilon \ll 1, \quad (3.36)$$

$$|\eta| \ll 1, \quad (3.37)$$

and the end of inflation is defined as the time when  $\epsilon, |\eta| \sim 1$ . The e-folding number  $N$  can also be written in terms of slow-roll parameters:

$$N \simeq \int H dt \simeq \int \frac{V}{V'} d\phi = \int \frac{d\phi}{\sqrt{2\epsilon}}, \quad (3.38)$$

which means that the duration of inflation becomes longer for smaller slow-roll parameters.

### 3.2.1 Inflation models

Here we give some examples of inflation models, where in particular the potential of the inflaton is specified.

#### Large field inflation

In the large field inflation models, the inflaton slow-rolls from a large initial value ( $> M_{\text{pl}}$ ) to the origin. In the Planck era  $H \sim M_{\text{pl}}$ , the energy density of the inflaton is naively expected to be

$$\rho \sim M_{\text{pl}}^4, \quad (3.39)$$

$$(\partial_i \phi)^2 \sim M_{\text{pl}}^4, \quad (3.40)$$

$$V \sim M_{\text{pl}}^4, \quad (3.41)$$

which is called chaotic conditions in the early universe. If we consider the following potential (Fig. 3.3),

$$V(\phi) = \frac{1}{2} m^2 \phi^2, \quad (3.42)$$

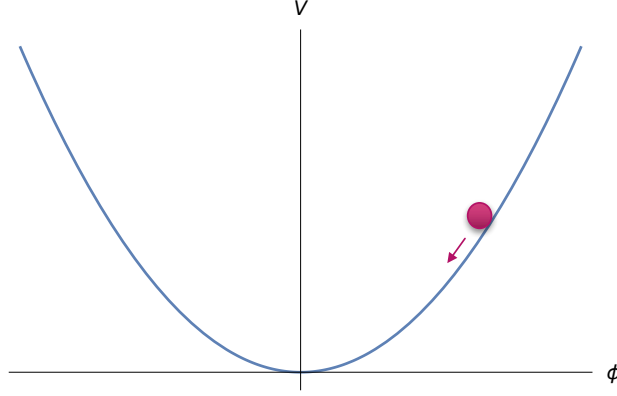


Figure 3.3: Illustration of the large field inflation.

the above conditions give

$$L \sim \frac{\phi}{M_{\text{pl}}^2}, \quad (3.43)$$

$$\phi \sim \frac{M_{\text{pl}}^2}{m}, \quad (3.44)$$

where  $L$  is the typical length scale for spatial variation of  $\phi$ . Since the inflaton mass must be much smaller than the Planck mass, as we will see later, this allows  $\phi$  to take a large initial value compared to  $M_{\text{pl}}$ , throughout the horizon scale. Since the slow-roll parameters become

$$\epsilon = \frac{M_{\text{pl}}^2}{2} \left( \frac{V'}{V} \right)^2 \quad (3.45)$$

$$= 2 \left( \frac{M_{\text{pl}}}{\phi} \right)^2, \quad (3.46)$$

$$\eta = M_{\text{pl}}^2 \frac{V''}{V} \quad (3.47)$$

$$= 2 \left( \frac{M_{\text{pl}}}{\phi} \right)^2, \quad (3.48)$$

we can see that  $\phi > M_{\text{pl}}$  naturally drives the slow-roll inflation. This is called chaotic inflation [33]. Friedmann equation and the equation of motion for  $\phi$  can

be solved as

$$\phi(t) \simeq \phi_i - \sqrt{\frac{2}{3}} M_{\text{pl}} m (t - t_i), \quad (3.49)$$

$$a(t) \simeq a_i \exp \left[ \frac{m}{\sqrt{6} M_{\text{pl}}} \phi_i (t - t_i) - \frac{m^2}{6} (t - t_i)^2 \right] \quad (3.50)$$

$$\simeq a_i \exp \left[ \frac{1}{4 M_{\text{pl}}^2} (\phi_i^2 - \phi^2(t)) \right] \quad (3.51)$$

The inflaton at the end of inflation is obtained from  $\epsilon, |\eta| \sim 1$  as

$$\phi_{\text{end}} \simeq \sqrt{2} M_{\text{pl}}. \quad (3.52)$$

Then, the e-folds  $N$  becomes

$$N = \ln \left( \frac{a_{\text{end}}}{a_i} \right) \quad (3.53)$$

$$\simeq \frac{1}{4 M_{\text{pl}}^2} (\phi_i^2 - 2 M_{\text{pl}}^2), \quad (3.54)$$

and  $N \gtrsim 60$  is realized for

$$\phi_i \gtrsim 15 M_{\text{pl}}, \quad (3.55)$$

which means that  $\Delta\phi > M_{\text{pl}}$  during the inflation.

### Small field inflation

In the small field inflation, the inflaton slowly rolls from the origin to a non-zero minimum of the potential (Fig. 3.4), whose expansion around the origin becomes the following form:

$$V = V_0 \left[ 1 - \left( \frac{\phi}{v} \right)^n \right], \quad (3.56)$$

The change of  $\phi$  during the inflation typically becomes smaller than  $M_{\text{pl}}$ :  $\Delta\phi < M_{\text{pl}}$ , as we will see below.

We consider the following potential:

$$V = V_0 - \frac{\lambda}{4} \phi^4, \quad (3.57)$$

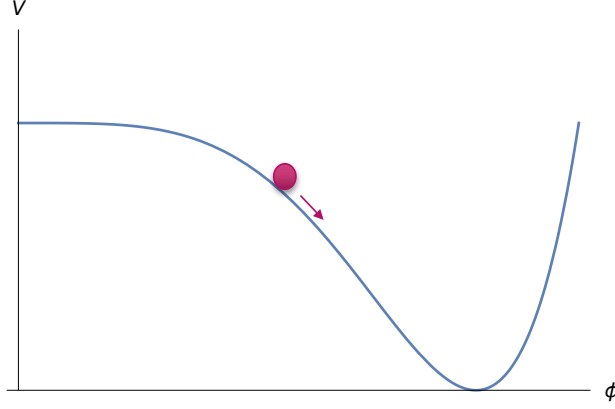


Figure 3.4: Illustration of the small field inflation.

which is an approximation around the origin, neglecting the true minimum. This is called new inflation model [34]. Then, the slow-roll parameters become

$$\epsilon = \frac{M_{\text{pl}}^2}{2} \left( \frac{\lambda \phi^3}{V_0} \right)^2, \quad (3.58)$$

$$\eta = -M_{\text{pl}}^2 \frac{3\lambda \phi^2}{V_0}. \quad (3.59)$$

Since  $V_0 > \lambda \phi^4$  around the origin, the following hierarchy exists:

$$|\eta| \gg \epsilon, \quad (3.60)$$

hence, in particular, the inflation end is defined by  $|\eta| \sim 1$  as

$$\phi_{\text{end}} = \left( \frac{V_0}{3\lambda M_{\text{pl}}^2} \right)^{1/2}. \quad (3.61)$$

Then, the e-folds  $N$  is given by

$$N = \frac{1}{M_{\text{pl}}^2} \int_{\phi_{\text{end}}}^{\phi_i} \frac{V}{V'} d\phi \quad (3.62)$$

$$= \frac{V_0}{2\lambda M_{\text{pl}}^2 \phi_i^2} - \frac{3}{2} \quad (3.63)$$

$$\simeq \frac{V_0}{2\lambda M_{\text{pl}}^2 \phi_i^2}, \quad (3.64)$$

and  $N \gtrsim 60$  requires the following initial value of  $\phi$ :

$$\phi_i \lesssim \left( \frac{V_0}{120\lambda M_{\text{pl}}^2} \right)^{1/2}. \quad (3.65)$$

Requiring

$$V_0 > \frac{1}{4}\lambda\phi_{\text{end}}^4, \quad (3.66)$$

we obtain the following condition:

$$\frac{V_0}{36\lambda M_{\text{pl}}^4} < 1, \quad (3.67)$$

which gives

$$\Delta\phi \simeq \left( \frac{V_0}{3\lambda M_{\text{pl}}^2} \right)^{1/2} < M_{\text{pl}}. \quad (3.68)$$

Eq. (3.65) means that the initial value  $\phi_i$  must be tuned sufficiently close to the origin, which leads to the initial value problem. This can be realized through the finite temperature effect, for instance, which gives the positive thermal mass to the scalar field coupled to the plasma.

### Hybrid inflation

In the model called hybrid inflation [35], another scalar field besides the inflaton, called waterfall field, is introduced to play the role to terminate inflation as it causes an instability. For instance, we consider the following potential (Fig. 3.5):

$$V = \frac{1}{2}m^2\phi^2 + \frac{\lambda}{4} \left( \chi^2 - \frac{M^2}{\lambda} \right)^2 + \frac{1}{2}g^2\phi^2\chi^2, \quad (3.69)$$

where  $\phi$  and  $\chi$  denote the inflaton and waterfall fields, respectively. Then, the effective mass of  $\chi$  becomes

$$m_{\chi,\text{eff}}^2 = 3\lambda\chi^2 - M^2 + g^2\phi^2, \quad (3.70)$$

and we can see that  $\chi$  is fixed at the origin by the positive effective mass when

$$\phi > \phi_c \equiv \frac{M}{g}. \quad (3.71)$$

If we assume that this is satisfied initially, the potential becomes

$$V = \frac{M^4}{4\lambda} + \frac{1}{2}m^2\phi^2, \quad (3.72)$$

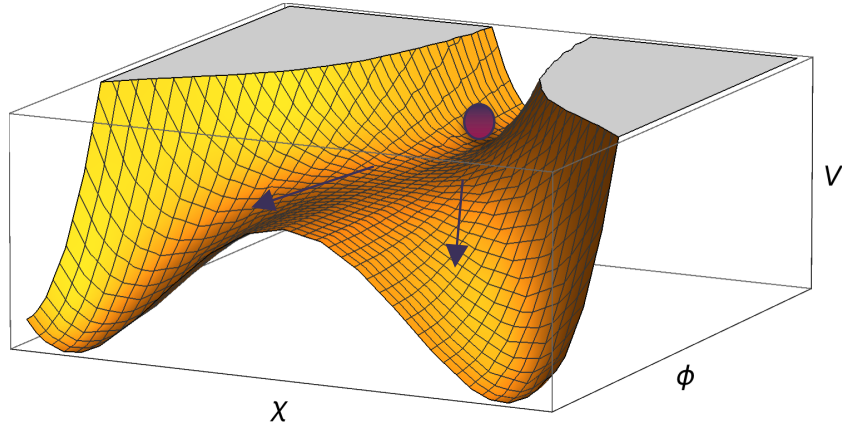


Figure 3.5: Illustration of the hybrid inflation.

with  $\chi = 0$ . Since the constant term also drives the inflation, the small value of inflaton  $\phi_i < M_{\text{pl}}$  is possible, unlike in the case of the chaotic inflation, where the potential is just

$$V = \frac{1}{2}m^2\phi^2. \quad (3.73)$$

Assuming the domination of the constant term, we obtain the following slow-roll parameters:

$$\epsilon = \frac{M_{\text{pl}}^2}{2} \left( \frac{4\lambda m^2 \phi}{M^4} \right)^2, \quad (3.74)$$

$$\eta = M_{\text{pl}}^2 \frac{4\lambda m^2}{M^4}, \quad (3.75)$$

which satisfy

$$\eta \gg \epsilon, \quad (3.76)$$

by the above assumption. Then, the inflation is realized for

$$m \ll \frac{M^2}{2\sqrt{\lambda}M_{\text{pl}}}, \quad (3.77)$$

which leads to  $\eta \ll 1$ . When  $\phi$  becomes smaller than  $\phi_c$ , the origin becomes unstable and  $\chi$  falls down to either of the following non-zero minima of the potential:

$$\phi = 0, \quad (3.78)$$

$$\chi = \pm \frac{m}{\sqrt{\lambda}}, \quad (3.79)$$



which terminates inflation. Then, we obtain the following e-folds  $N$ :

$$N = \frac{1}{M_{\text{pl}}^2} \int_{\phi_c}^{\phi_i} \frac{V}{V'} d\phi \quad (3.80)$$

$$= \frac{M^4}{4\lambda M_{\text{pl}}^2 m^2} \ln \left( \frac{\phi_i}{\phi_c} \right), \quad (3.81)$$

and  $N \gtrsim 60$  requires

$$\phi_i \gtrsim \phi_c e^{240\lambda M_{\text{pl}}^2 m^2 / M^4} \quad (3.82)$$

$$\sim \phi_c, \quad (3.83)$$

where we used Eq. (3.77), which can make the exponent sufficiently small. Therefore, we can see that the initial value of the inflaton can be smaller than  $M_{\text{pl}}$ , for sufficiently small  $\phi_c$ .

### 3.3 Generation of primordial fluctuations

In the previous section, we realized inflation through the classical dynamics of the inflaton  $\phi$ . In this section, we show that the quantum fluctuation of  $\phi$  leads to the primordial curvature perturbation, which will become the initial condition of various perturbations studied in the previous chapter.

Here we choose Newtonian gauge  $E = B = 0$ , which gives

$$\psi|_{E=B=0} = \Psi, \quad (3.84)$$

$$A|_{E=B=0} = \Phi. \quad (3.85)$$

Then, the equation of motion for quantum fluctuation  $\delta\phi$  is given by

$$\delta\phi'' + 2\mathcal{H}\delta\phi' - \left( \Delta - a^2 \frac{d^2 V}{d\bar{\phi}^2} \right) \delta\phi - \bar{\phi}'(3\Psi' + \Phi') + 2a^2 \frac{dV}{d\bar{\phi}} \Phi = 0, \quad (3.86)$$

where bar denotes the background and we used the conformal time  $d\tau \equiv a^{-1}dt$  as the time variable. We have also defined  $\mathcal{H} \equiv a'/a$ . Since the inflaton does not induce the anisotropic stress tensor  $\pi_{ij}$ , the following relation is obtained:

$$\Psi - \Phi = \frac{a^2 \pi^S}{M_{\text{pl}}^2} = 0, \quad (3.87)$$

Then, the equation of motion reduces to

$$\delta\phi'' + 2\mathcal{H}\delta\phi' - \left( \Delta - a^2 \frac{d^2 V}{d\bar{\phi}^2} \right) \delta\phi - 4\bar{\phi}'\Phi' + 2a^2 \frac{dV}{d\bar{\phi}} \Phi = 0. \quad (3.88)$$

Here we define the following variable:

$$u \equiv a \left( \delta\phi + \frac{\bar{\phi}'}{\mathcal{H}} \Psi \right), \quad (3.89)$$

which is related to the curvature perturbation as

$$\mathcal{R}_c = \frac{u}{z}, \quad (3.90)$$

where  $z \equiv a\bar{\phi}'/\mathcal{H}$ . This quantity  $u$  is called Mukhanov-Sasaki variable, whose equation of motion is derived as

$$u'' - \Delta u - \frac{z''}{z}u = 0, \quad (3.91)$$

where the redundant terms including time and spatial derivatives vanish by using the Einstein equations and Poisson equation. If we expand  $u$  as

$$u(\mathbf{x}, \tau) = \int \frac{d^3k}{(2\pi)^{3/2}} [a_{\mathbf{k}} u_k(\tau) e^{i\mathbf{k}\cdot\mathbf{x}} + \text{h.c.}], \quad (3.92)$$

the commutation relation

$$[u(\mathbf{x}, \tau), u'(\mathbf{y}, \tau)] = i\delta^3(\mathbf{x} - \mathbf{y}) \quad (3.93)$$

gives

$$[a_{\mathbf{k}}, a_{\mathbf{k}'}^\dagger] = \delta^3(\mathbf{k} - \mathbf{k}'), \quad (3.94)$$

if we normalize the mode function  $u_k$  as

$$u_k u_k'^* - u_k' u_k^* = i. \quad (3.95)$$

The equation of motion for  $u_k$  becomes

$$u_k'' + \left( k^2 - \frac{z''}{z} \right) u_k = 0. \quad (3.96)$$

The variable  $z$  and its derivatives can be written in terms of the slow-roll parameters, which gives

$$\frac{z''}{z} \simeq \frac{2 + 9\epsilon - 3\eta}{\tau^2}. \quad (3.97)$$

Then, the equation of motion becomes

$$u_k'' + \left( k^2 - \frac{\nu^2 - 1/4}{\tau^2} \right) u_k = 0, \quad (3.98)$$

with  $\nu \equiv 3/2 + 3\epsilon - \eta$ , and its solution is given as the following linear combination of the Hankel functions:

$$u_k(\tau) = A_k \sqrt{-\tau} H_\nu^{(1)}(-k\tau) + B_k \sqrt{-\tau} H_\nu^{(2)}(-k\tau). \quad (3.99)$$

Requiring the following subhorizon limit of the mode function,

$$u_k \rightarrow \frac{1}{\sqrt{2k}} e^{-ik\tau}, \quad -k\tau \gg 1 \quad (3.100)$$

we obtain

$$u_k(\tau) = \frac{\sqrt{\pi}}{2} e^{i(2\nu+1)\pi/4} \sqrt{-\tau} H_\nu^{(1)}(-k\tau), \quad (3.101)$$

whose overall normalization is given by Eq. (3.95). The superhorizon limit becomes

$$u_k \rightarrow 2^{\nu-3/2} e^{i(2\nu+1)\pi/4} \frac{\Gamma(\nu)}{\Gamma(3/2)} \frac{1}{\sqrt{2k}} (-k\tau)^{1/2-\nu}, \quad -k\tau \ll 1 \quad (3.102)$$

which gives the following power spectrum of the curvature perturbation:

$$\mathcal{P}_{\mathcal{R}_c}(k) = \frac{1}{z^2} \mathcal{P}_u(k) = \frac{1}{z^2} \frac{k^3}{2\pi^2} |u_k|^2 \quad (3.103)$$

$$= \frac{H^2}{8\pi^2 M_{\text{pl}}^2 \epsilon} \left( \frac{k}{aH} \right)^{-6\epsilon+2\eta} \quad (3.104)$$

$$\simeq \frac{H^2}{8\pi^2 M_{\text{pl}}^2 \epsilon} \Big|_{k \simeq aH}, \quad (3.105)$$

whose spectral index  $n_s$  is given by

$$n_s - 1 \equiv \frac{d \ln \mathcal{P}_{\mathcal{R}_c}(k)}{d \ln k} \quad (3.106)$$

$$\simeq -6\epsilon + 2\eta. \quad (3.107)$$

By performing the similar analysis, we can calculate the tensor perturbation generated by the inflation. The equation of motion for tensor mode

$$\ddot{h}_{ij} + 3H\dot{h}_{ij} - \frac{1}{a^2} h_{ij} = 0, \quad (3.108)$$

can be rewritten as

$$v_{ij}'' - \Delta v_{ij} - \frac{a''}{a} v_{ij} = 0, \quad (3.109)$$

where we have defined

$$v_{ij} \equiv \frac{a}{2} M_{\text{pl}} h_{ij}, \quad (3.110)$$

and used the conformal time as the time variable. We can expand  $v_{ij}$  as

$$v_{ij}(\mathbf{x}, \tau) = \int \frac{d^3 k}{(2\pi)^{3/2}} \sum_{\lambda=+, \times} \left[ \mathbf{e}_{ij}^{(\lambda)}(\mathbf{k}) a_{\mathbf{k}}^{(\lambda)} v_k(\tau) e^{i\mathbf{k} \cdot \mathbf{x}} + \text{h.c.} \right], \quad (3.111)$$

where  $\mathbf{e}_{ij}^{(\lambda)}$  denotes the polarization, which satisfies

$$\mathbf{e}_{ii}^{(\lambda)} = 0, \quad (3.112)$$

$$k_i \mathbf{e}_{ij}^{(\lambda)} = 0, \quad (3.113)$$

$$\mathbf{e}_{ij}^{(\lambda)} \mathbf{e}_{ij}^{(\lambda')} = \delta_{\lambda\lambda'}. \quad (3.114)$$

For  $\mathbf{k} = (0, 0, k)$ , for example,  $\mathbf{e}_{ij}^{(\lambda)}$  has the following form:

$$\mathbf{e}_{ij}^{(+)} = \frac{1}{\sqrt{2}} \begin{pmatrix} 1 & 0 & 0 \\ 0 & -1 & 0 \\ 0 & 0 & 0 \end{pmatrix}, \quad \mathbf{e}_{ij}^{(\times)} = \frac{1}{\sqrt{2}} \begin{pmatrix} 0 & 1 & 0 \\ 1 & 0 & 0 \\ 0 & 0 & 0 \end{pmatrix}. \quad (3.115)$$

Then, the equation for the mode function  $v_k$  becomes

$$v_k'' + \left( k^2 - \frac{a''}{a} \right) v_k = 0, \quad (3.116)$$

and using

$$\frac{a''}{a} \simeq \frac{2 + 3\epsilon}{\tau^2}, \quad (3.117)$$

it reduces to

$$v_k'' + \left( k^2 - \frac{\mu^2 - 1/4}{\tau^2} \right) v_k = 0, \quad (3.118)$$

where  $\mu \equiv \sqrt{9/4 + 3\epsilon} \simeq 3/2 + \epsilon$ . Hence, we already know the solution has the following form:

$$v_k(\tau) = \frac{\sqrt{\pi}}{2} e^{i(2\mu+1)\pi/4} \sqrt{-\tau} H_{\mu}^{(1)}(-k\tau), \quad (3.119)$$

whose superhorizon limit becomes

$$v_k \rightarrow 2^{\mu-3/2} e^{i(2\mu+1)\pi/4} \frac{\Gamma(\mu)}{\Gamma(3/2)} \frac{1}{\sqrt{2k}} (-k\tau)^{1/2-\mu}, \quad -k\tau \ll 1 \quad (3.120)$$

which gives the following power spectrum of tensor perturbation:

$$\mathcal{P}_T(k) = \frac{4}{a^2 M_{\text{pl}}^2} \mathcal{P}_v(k) = \frac{4}{a^2 M_{\text{pl}}^2} \frac{2k^3}{2\pi^2} |v_k|^2 \quad (3.121)$$

$$= \frac{2H^2}{\pi^2 M_{\text{pl}}^2} \left( \frac{k}{aH} \right)^{-2\epsilon} \quad (3.122)$$

$$\simeq \frac{2H^2}{\pi^2 M_{\text{pl}}^2} \Big|_{k \simeq aH}, \quad (3.123)$$

and its spectral index:

$$n_T \equiv \frac{d \ln \mathcal{P}_T(k)}{d \ln k}. \quad (3.124)$$

$$\simeq -2\epsilon \quad (3.125)$$

The tensor-to-scalar ratio  $r$  is given by

$$r \equiv \frac{\mathcal{P}_T}{\mathcal{P}_{\mathcal{R}_c}} \simeq 16\epsilon \quad (3.126)$$

$$\simeq -8n_T \quad (3.127)$$

$$\simeq \frac{8}{3}(1 - n_s) + \frac{16}{3}\eta. \quad (3.128)$$

The final expression is quite useful, since the predictions are usually presented in the  $n_s$ - $r$  plane.

### 3.3.1 Model dependence

Recent observations suggest the following values for the inflationary variables [13]:

$$\mathcal{P}_{\mathcal{R}_c}(k_*) \simeq 2.4 \times 10^{-9}, \quad (3.129)$$

$$n_s \simeq 0.968 \pm 0.006, \quad (3.130)$$

$$r < 0.11, \quad (3.131)$$

where  $k_* = 0.002$  Mpc is the CMB pivot scale. In the following, we will see whether these values can be obtained by the predictions from the specific inflation models.

## Chaotic inflation

In the chaotic inflation with the following potential,

$$V = \frac{1}{2}m^2\phi^2, \quad (3.132)$$

the inflationary observables can be written in terms of  $m$  and the e-folds  $N$  as follows:

$$\mathcal{P}_{\mathcal{R}_c}(k_*) \simeq \frac{m^2 N_*^2}{6\pi^2 M_{\text{pl}}^2}, \quad (3.133)$$

$$n_s \simeq 1 - \frac{2}{N_*}, \quad (3.134)$$

$$r \simeq \frac{8}{N_*}, \quad (3.135)$$

where  $N_*$  is the e-folds when the CMB pivot scale  $k_*$  crosses the horizon. The observation for the power spectrum gives

$$m \simeq 1.6 \times 10^{13} \text{ GeV} \left( \frac{N_*}{60} \right)^{-1}, \quad (3.136)$$

which is especially smaller than  $M_{\text{pl}}$ . The spectral index  $n_s$  and tensor-to-scalar ratio  $r$  becomes

$$n_s \simeq 0.97, \quad (3.137)$$

$$r \simeq 0.13, \quad (3.138)$$

for  $N_* = 60$ , for example. This choice leads to the observationally favored  $n_s$ , but deviates  $r$  from the observational value. Actually, it turned out that this model is difficult to explain the observations for any  $N_*$  (see Fig. 3.6).

## New inflation

For new inflation with the potential

$$V = V_0 - \frac{\lambda}{4}\phi^4, \quad (3.139)$$

around the origin, the observables are given as

$$\mathcal{P}_{\mathcal{R}_c}(k_*) \simeq \frac{2\lambda N_*^3}{3\pi^2}, \quad (3.140)$$

$$n_s \simeq 1 - \frac{3}{N_*}, \quad (3.141)$$

$$r \simeq \frac{V_0}{\lambda M_{\text{pl}}^4 N_*^3} < \frac{36}{N_*^3}, \quad (3.142)$$

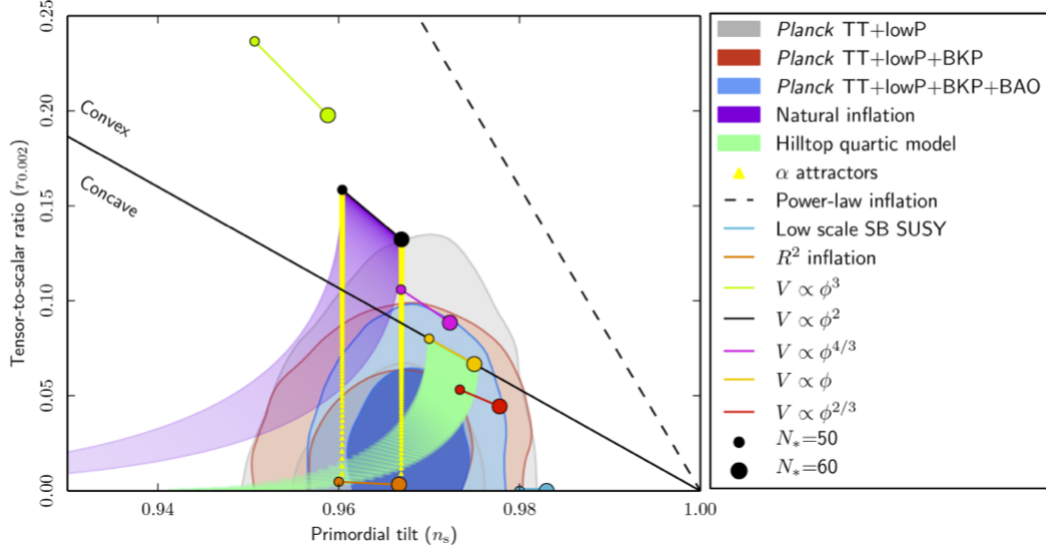


Figure 3.6: The latest Planck results [13] compared to the theoretical predictions of selected inflation models.

where we used Eq. (3.67) in the last line. Then, the observation for the power spectrum gives

$$\lambda \simeq 1.7 \times 10^{-13} \left( \frac{N_*}{60} \right)^{-3}, \quad (3.143)$$

and for  $n_s$  and  $r$ :

$$n_s \simeq 0.95, \quad (3.144)$$

$$r < 1.7 \times 10^{-4}, \quad (3.145)$$

for  $N_* = 60$ , for example. This time it is difficult to explain the observational value of  $n_s$ .

### Hybrid inflation

In the case of the hybrid inflation, the inflaton potential is given by the following form:

$$V = V_0 + \frac{1}{2} m^2 \phi^2, \quad (3.146)$$

as derived in the previous section. If we assume that  $V_0$  dominates the potential, the slow-roll parameters become

$$\epsilon = \frac{M_{\text{pl}}^2}{2} \left( \frac{m^2 \phi}{V_0} \right)^2, \quad (3.147)$$

$$\eta = M_{\text{pl}}^2 \frac{m^2}{V_0}, \quad (3.148)$$

which satisfy

$$\eta \gg \epsilon. \quad (3.149)$$

This gives the following spectral index  $n_s$  of the primordial curvature perturbation:

$$n_s \simeq 1 - 6\epsilon + 2\eta \quad (3.150)$$

$$\simeq 1 + 2\eta \quad (3.151)$$

$$= 1 + 2M_{\text{pl}}^2 \frac{m^2}{V_0} \quad (3.152)$$

$$> 1. \quad (3.153)$$

Since the observational value of  $n_s$  is smaller than unity, we find that this simple hybrid model is again ruled out by the observations.

From the above examples of the inflation models, we note that the observations actually exclude the various class of models. In Chap. 9, we will see an example that is favored by the observations, which is a recently proposed model.

### 3.4 Reheating

So far, we saw that the inflaton classically drives the inflation and its quantum fluctuation becomes the seed of the primordial perturbations. After the inflation, the inflaton oscillates around the origin (Fig. 3.7), and eventually decay into the SM particles in order to realize our hot universe, which is called reheating. This can be described by the following equations:

$$\frac{d\rho_\phi}{dt} = -3H\rho_\phi - \Gamma\rho_\phi, \quad (3.154)$$

$$\frac{d\rho_r}{dt} = -4H\rho_r + \Gamma\rho_\phi, \quad (3.155)$$



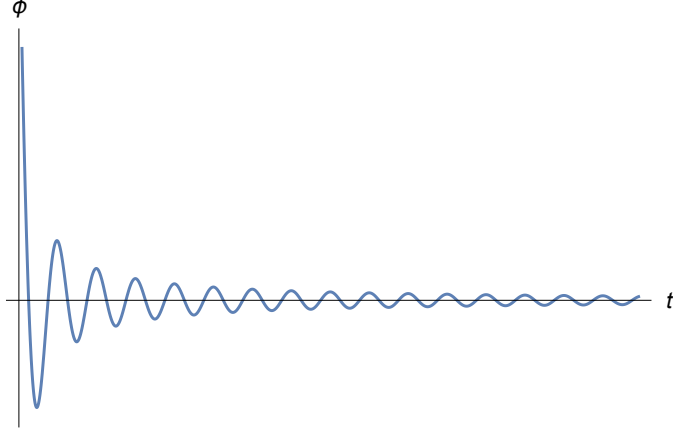


Figure 3.7: The coherent oscillation of the inflaton after the inflation. The amplitude is damped due to the cosmic expansion.

where  $\rho_\phi$  and  $\rho_r$  denote the energy density of the inflaton and radiation, respectively, and  $\Gamma$  is the decay rate of the inflaton. These can be solved as

$$\rho_\phi(t) = \rho_\phi(t_{\text{end}}) \left( \frac{a(t_{\text{end}})}{a(t)} \right)^3 e^{-\Gamma(t-t_{\text{end}})}, \quad (3.156)$$

$$\rho_r(t) = a^{-4}(t) \int_{t_{\text{end}}}^t a^4(t') \Gamma \rho_\phi(t') dt' \quad (3.157)$$

$$= \rho_\phi(t_{\text{end}}) \Gamma a^3(t_{\text{end}}) a^{-4}(t) \int_{t_{\text{end}}}^t a(t') e^{-\Gamma(t'-t_{\text{end}})} dt' \quad (3.158)$$

Before the reheating completes,  $\Gamma t \sim \Gamma/H < 1$  is satisfied, hence the integral is easily performed as

$$\rho_r(t) \sim \Gamma H M_{\text{pl}}^2 \quad (3.159)$$

$$\propto a^{-3/2}, \quad (3.160)$$

where we used  $a \propto t^{2/3}$  and  $\rho_\phi \sim H^2 M_{\text{pl}}^2$ . The temperature can be obtained from  $\rho_r \sim T^4$  as

$$T \sim (\Gamma H M_{\text{pl}}^2)^{1/4}. \quad (3.161)$$

Note that this temperature of subdominant plasma decreases slowly as  $t^{-1/4}$ , compared to the dominant case  $T \propto t^{1/2}$ . We illustrate this behavior of the temperature in Fig. 3.8.

The reheating completes when  $\Gamma \sim H$ , and the temperature at that time is defined as the reheating temperature  $T_{\text{RH}}$ , which is given as

$$T_{\text{RH}} \sim \Gamma^{1/2}, \quad (3.162)$$

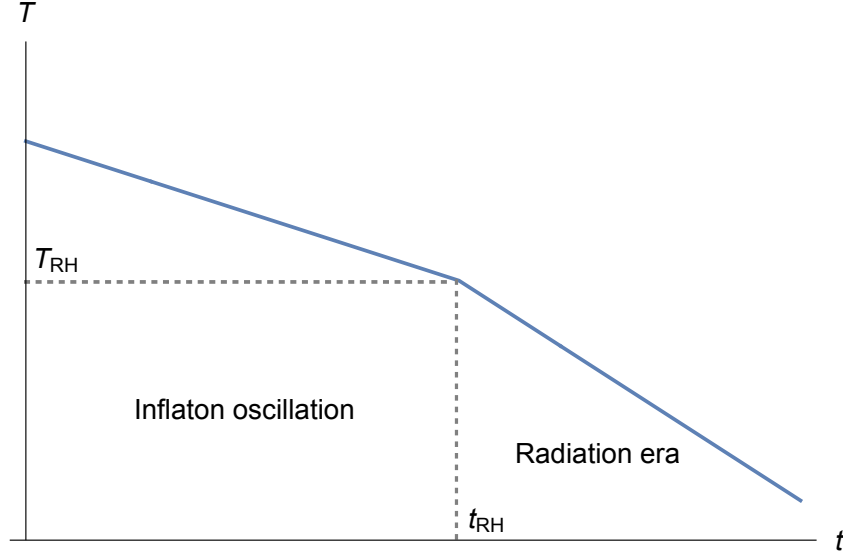


Figure 3.8: Behavior of the temperature after inflation.

using  $H \sim T_{\text{RH}}^2$ .

The decay of the inflaton  $\phi$  is described by the interactions of the following forms:

$$\mathcal{L} \supset g\sigma\phi\chi\chi, \quad y\phi\bar{\psi}\psi, \quad (3.163)$$

where  $\chi$  and  $\psi$  denote the scalar and fermion, respectively, which give the following decay rates:

$$\Gamma(\phi \rightarrow \chi\chi) \simeq \frac{g^2\sigma^2}{8\pi m_\phi} \left(1 - \frac{4m_\chi^2}{m_\phi^2}\right)^{1/2} \quad (3.164)$$

$$\simeq \frac{g^2\sigma^2}{8\pi m_\phi}, \quad (3.165)$$

$$\Gamma(\phi \rightarrow \psi\bar{\psi}) \simeq \frac{y^2 m_\phi}{8\pi} \left(1 - \frac{4m_\psi^2}{m_\phi^2}\right)^{1/2} \quad (3.166)$$

$$\simeq \frac{y^2 m_\phi}{8\pi}, \quad (3.167)$$

where we assumed  $m_\chi, m_\psi \ll m_\phi$ .

### 3.5 Reheating temperature and e-folds

The reheating temperature determines the beginning of radiation-dominated era and affects the redshift of the CMB pivot scale  $k_*$ , which in turn gives the informations on the time when  $k_*$  crossed the horizon during inflation, usually described by the e-folds  $N_*$ . In this section, we derive the relation between the reheating temperature  $T_{\text{RH}}$  and the e-folds  $N_*$ :

The CMB pivot scale  $k_*$  is given as

$$k_* = \frac{a_*}{a_0} H_* \quad (3.168)$$

$$= \frac{a_{\text{RH}}}{a_0} \frac{a_{\text{end}}}{a_{\text{RH}}} \frac{a_*}{a_{\text{end}}} H_*. \quad (3.169)$$

Then, the definition of the e-folds gives

$$\frac{a_*}{a_{\text{end}}} = e^{-N_*}. \quad (3.170)$$

The energy density just before the reheating is

$$\rho_\phi(t_{\text{RH}}) = \left( \frac{a_{\text{end}}}{a_{\text{RH}}} \right)^3 \rho_\phi(t_{\text{end}}) \quad (3.171)$$

$$= \left( \frac{a_{\text{end}}}{a_{\text{RH}}} \right)^3 3H_{\text{end}}^2 M_{\text{pl}}^2, \quad (3.172)$$

where we used  $\rho_\phi(t_{\text{end}}) = 3H_{\text{end}}^2 M_{\text{pl}}^2$ . If we assume the instantaneous reheating, this becomes equal to

$$\rho_r \simeq \frac{\pi^2}{30} g_* T_{\text{RH}}^4, \quad (3.173)$$

which is the energy density of the radiation just after the reheating. This leads to

$$\frac{a_{\text{end}}}{a_{\text{RH}}} \simeq \left( \frac{\pi^2 g_* T_{\text{RH}}^4}{90 H_{\text{end}}^2 M_{\text{pl}}^2} \right)^{1/3}. \quad (3.174)$$

Finally, using the entropy conservation, we obtain

$$\frac{a_{\text{RH}}}{a_0} = \left( \frac{s_0}{s_{\text{RH}}} \right)^{1/3} \quad (3.175)$$

$$= \left( \frac{45 s_0}{2\pi^2 g_* T_{\text{RH}}^3} \right)^{1/3}, \quad (3.176)$$

which gives

$$k_* = \left( \frac{45s_0}{2\pi^2 g_* T_{\text{RH}}^3} \right)^{1/3} \left( \frac{\pi^2 g_* T_{\text{RH}}^4}{90 H_{\text{end}}^2 M_{\text{pl}}^2} \right)^{1/3} e^{-N_*} H_*. \quad (3.177)$$

If we use the present value of the entropy density  $s_0 \simeq 2.8 \times 10^3 \text{ cm}^{-3}$ , we finally obtain the following relation:

$$N_* = 52.6 - \ln \left( \frac{k_*}{0.001 \text{ Mpc}^{-1}} \right) + \frac{1}{3} \ln \left( \frac{T_{\text{RH}}}{10^{10} \text{ GeV}} \right) - \frac{2}{3} \ln \left( \frac{H_{\text{end}}}{10^{10} \text{ GeV}} \right) + \ln \left( \frac{H_*}{10^{10} \text{ GeV}} \right), \quad (3.178)$$

which especially becomes

$$N_* = 52.6 - \ln \left( \frac{k_*}{0.001 \text{ Mpc}^{-1}} \right) + \frac{1}{3} \ln \left( \frac{T_{\text{RH}}}{10^{10} \text{ GeV}} \right) + \frac{1}{3} \ln \left( \frac{H_I}{10^{10} \text{ GeV}} \right), \quad (3.179)$$

if the Hubble rate  $H$  is nearly constant  $H_I$  during the inflation.

# Chapter 4

## Affleck-Dine mechanism

In this chapter, we review the Affleck-Dine mechanism, where baryon asymmetry in the universe (BAU) is generated through the phase dynamics of a baryonic scalar field after inflation. For the baryonic scalar field, the flat directions in MSSM are used, since it must have large VEV in order to generate the sufficient amount of BAU. The dynamics of the flat direction is governed by the negative Hubble-induced mass term, which comes from SUSY breaking effect, and non-renormalizable terms in the superpotential, which stabilizes the flat direction. We will see that this dynamics properly generates the BAU.

### 4.1 Baryogenesis

Since the Affleck-Dine mechanism is proposed in the context of baryogenesis, we briefly comment on the basic issues. In Chap. 2, we saw that in order to explain the observed abundances of elements, the redundancy of matter to anti-matter is required, which implies the following baryon asymmetry at BBN:

$$\eta_B = \frac{n_B}{s} \sim 10^{-10}, \quad (4.1)$$

where  $n_B, s$  denote baryon number density and entropy density, respectively. This means that the baryon asymmetry has existed since early universe, whose generation is called baryogenesis. In order to generate the baryon asymmetry in the early universe, several conditions must be satisfied, which we summarize in the following.

#### 4.1.1 Sakharov's conditions

In 1967, Andrei Sakharov proposed three necessary conditions for baryogenesis. In this subsection, we review those conditions, which generically apply to the

mechanisms for baryogenesis, besides the Affleck-Dine mechanism.

### Baryon number violation

First, in order to generate the baryon number, we need an elementary process that violates the baryon number. In the SM, the baryon number is violated due to the quantum anomaly, and baryon number changing can be realized through the transition between topological vacuums. It is known that this transition rate is unreasonably small, but by thermally hopping to the intermediate configuration called sphaleron [36], the transition can be efficient, which is known to be in equilibrium for the temperature of  $10^2 \text{ GeV} \lesssim T \lesssim 10^{13} \text{ GeV}$ . However, in order to generate the net baryon asymmetry, the violation towards matter must be more efficient than anti-matter, which is especially not the case in thermal equilibrium. This leads to the following other conditions.

### C, CP violation

We consider Dirac fermions  $X, Y, X_B$  with baryon charge  $(0, 0, 1)$ , and assume the baryon number violating process  $X \rightarrow Y + X_B$ . However, if the charge conjugation  $C$  is conserved,

$$\Gamma(X \rightarrow Y + X_B) \propto |\langle Y, X_B | e^{-iHt} | X \rangle|^2 \quad (4.2)$$

$$= |\langle Y, X_B | C^{-1} C e^{-iHt} C^{-1} C | X \rangle|^2 \quad (4.3)$$

$$= |\langle Y^c, X_B^c | e^{-iHt} | X^c \rangle|^2, \quad (4.4)$$

which leads to

$$\Gamma(X^c \rightarrow Y^c + X_B^c) = \Gamma(X \rightarrow Y + X_B), \quad (4.5)$$

where  $^c$  denotes the charge conjugation. This means that the production rate of positive baryon number is equal to that of negative baryon number, hence no asymmetry.

The CP can be defined for left-handed Weyl fermions, which we define as  $x, y, x_B$  with baryon charge  $(0, 0, 1)$ . Then, the same reasoning applies to the baryon number violating process  $x \rightarrow y + x_B$ , if we assume the CP conservation:

$$\Gamma(x \rightarrow y + x_B) \propto |\langle y, x_B | e^{-iHt} | x \rangle|^2 \quad (4.6)$$

$$= |\langle y, x_B | (CP)^{-1} C P e^{-iHt} (CP)^{-1} C P | x \rangle|^2 \quad (4.7)$$

$$= |\langle \bar{y}, \bar{x}_B | e^{-iHt} | \bar{x} \rangle|^2, \quad (4.8)$$

which gives

$$\Gamma(\bar{x} \rightarrow \bar{y} + \bar{x}_B) = \Gamma(x \rightarrow y + x_B), \quad (4.9)$$

where the bar denotes the anti-particle. This, again, implies no net baryon asymmetry.

Thus, we can conclude that C, CP must be violated in order to generate the baryon asymmetry. The SM violates C due to the chiral feature of  $SU(2)_L$  gauge symmetry. The CP transformations of Weyl fermion  $\chi$  and complex scalar  $\phi$  are given as  $\chi \rightarrow \chi^\dagger$  and  $\phi \rightarrow \phi^*$ , respectively, hence the complex phase in the Lagrangian will violate the CP. In the SM, CP is violated since there exists a complex phase in the CKM matrix. However, this CP violating phase is known to be too small to generate a sufficient amount of the baryon asymmetry of the universe.

### Departure from the equilibrium

Even if the above two conditions are satisfied, the baryon asymmetry is washed out by inverse processes in thermal equilibrium. This is equivalent to the relaxation of the system towards the thermal distribution:  $\rho(H) \sim e^{-H/T}$ , where  $\rho$  and  $H$  denote the density matrix and hamiltonian, respectively. We can show that the baryon asymmetry in this environment becomes zero:

$$\langle B \rangle = \text{Tr} [e^{-H/T} B] \quad (4.10)$$

$$= \text{Tr} [e^{-H/T} B (CPT) (CPT)^{-1}] \quad (4.11)$$

$$= -\text{Tr} [e^{-H/T} (CPT) B (CPT)^{-1}] \quad (4.12)$$

$$= -\text{Tr} [(CPT) e^{-H/T} B (CPT)^{-1}] \quad (4.13)$$

$$= -\text{Tr} [e^{-H/T} B] \quad (4.14)$$

$$= 0. \quad (4.15)$$

Thus, for baryogenesis, the system must depart from the equilibrium, or deviate from the thermal distribution  $e^{-H/T}$ .

In the following sections, we will see that these conditions for the baryogenesis are properly satisfied in Affleck-Dine mechanism and can generate a sufficient amount of baryon asymmetry of the universe.

## 4.2 Flat directions in MSSM

In MSSM, there exist many flat directions, due to the highly symmetric feature of the theory. For instance, we consider the following direction:

$$(u^c)_1^R = (d^c)_1^G = (d^c)_2^B \equiv \frac{1}{\sqrt{3}}\phi \quad (4.16)$$

where upper and lower index denote color and flavor, respectively. This direction is F-flat, since there is no F-term for this direction in MSSM. We can easily see that the D-term also vanishes:

$$D_3^a \propto (u^c)_1^{R*} T^a (u^c)_1^R + (d^c)_1^{G*} T^a (d^c)_1^G + (d^c)_2^{B*} T^a (d^c)_2^B \quad (4.17)$$

$$= \frac{1}{3} |\phi|^2 \text{Tr}[T^a] = 0, \quad (4.18)$$

$$D_1 \propto -\frac{2}{3} ((u^c)_1^R)^2 + \frac{1}{3} ((d^c)_1^G)^2 + \frac{1}{3} ((d^c)_2^B)^2 = 0. \quad (4.19)$$

We present the flat directions in MSSM [37] in App. C. The flat direction  $\phi$ , which is also called Affleck-Dine (AD) field, obtains the potential due to the SUSY breaking and higher-order terms, which governs the dynamics of the AD field. We discuss this issue in the next section.

## 4.3 Dynamics of Affleck-Dine field and baryogenesis

In the previous section, we saw that there exist many flat directions in MSSM. In the real world, however, SUSY is broken, whose mediation to the AD field induces the potential. The SUSY breaking can be mediated through gravitational, or SM gauge interaction, and each mechanism gives different forms of the potential. In this section, we pursue the dynamics of the AD field in each case. For the stabilization, we will also take into account the higher-order term in superpotential of the form  $W(\phi) = \lambda \phi^n / n M_*^{n-3}$ , with  $M_*$  cut-off scale. For  $u^c d^c d^c$  direction, for instance, this can be realized by  $W = 3^3 \lambda (u^c d^c d^c)^2 / 6 M_*^3$ , which corresponds to the case of  $n = 6$ .



### 4.3.1 Gravity mediation case

When SUSY is broken by the F-term, it can be mediated to the AD field through the following gravitational interactions:

$$\mathcal{L} \supset c_X \int d^2\theta d^2\bar{\theta} \frac{1}{M_{\text{pl}}^2} X^\dagger X \phi^\dagger \phi = c_X \frac{|F_X|^2}{M_{\text{pl}}^2} |\phi|^2, \quad (4.20)$$

$$\mathcal{L} \supset a_X \int d^2\theta \frac{X}{M_{\text{pl}}} W(\phi) + \text{h.c.} = a_X \frac{F_X}{M_{\text{pl}}} W(\phi) + \text{h.c.}, \quad (4.21)$$

where  $X$  is the SUSY breaking field and  $c_X, a_X$  are coupling constants. If we assume F-term inflation, the inflaton plays the role of  $X$ , besides the breaking sector in the present universe. During inflation,  $|F_I|^2 \sim V(I) \sim H^2$ , hence the AD potential is given in the following form:

$$V(\phi) = m_\phi^2 |\phi|^2 + \left( a_g \frac{\lambda}{n M_*^{n-3}} m_{3/2} \phi^n + \text{h.c.} \right) + c_H H^2 |\phi|^2 + \left( a_H \frac{\lambda}{n M_*^{n-3}} H \phi^n + \text{h.c.} \right) + \frac{\lambda^2}{M_*^{2n-6}} |\phi|^{2(n-1)}, \quad (4.22)$$

where  $m_\phi, m_{3/2}$  are soft mass and gravitino mass, respectively, which are nearly the same in the gravity mediation case. We also included  $|W'(\phi)|^2 = \lambda^2 |\phi|^{2(n-1)} / M_*^{2n-6}$ . If we take  $c_H < 0$ , we obtain the negative Hubble-induced mass, which dominates over the soft mass since  $H > m_\phi$  during inflation. This leads to the following non-zero VEV of  $\phi$ .

$$\phi \sim (H M_*^{n-3})^{1/(n-2)}, \quad (4.23)$$

which is almost constant, since  $H \simeq \text{const.}$ . The phase of  $\phi$  is determined by the Hubble-induced A-term, since  $H > m_{3/2} \sim m_\phi$ . After inflation, the Hubble rate decreases as  $H \simeq 2/3t$ , since the inflaton oscillation dominates the universe. When the Hubble rate becomes  $H \sim m_\phi$ , the AD field starts to oscillate about the origin. The phase dynamics also begins since the A-term proportional to  $m_{3/2}$  becomes efficient. The maximal rotation is obtained if there is a  $\pi/2$  difference in the phase of  $a_g$  and  $a_H$ :  $\arg(a_g) = \arg(a_H) \pm \pi/2$ . In Fig. 4.1, we present an example of AD dynamics in gravity mediation case, where we set  $M_* = M_{\text{pl}}$ ,  $m_\phi = 1$  TeV,  $n = 6$ ,  $\lambda = 1$ ,  $a_H = 1$ ,  $a_g = i$ .

We examine if this dynamics of the AD field can generate sufficient amount of BAU. The baryon number density is given by

$$n_B = ib(\dot{\phi}^* \phi - \phi^* \dot{\phi}), \quad (4.24)$$

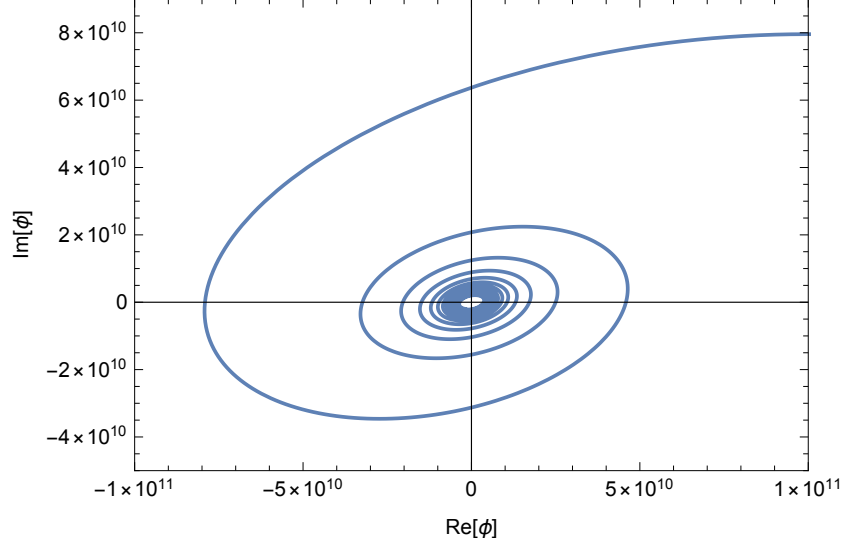


Figure 4.1: An example of AD dynamics in the gravity mediation case.

where  $b$  denotes baryon charge of the AD field. Using the equation of motion for  $\phi$  given as

$$\ddot{\phi} + 3H\dot{\phi} + V'(\phi) = 0, \quad (4.25)$$

we obtain the following equation for  $n_B$ .

$$\dot{n}_B + 3Hn_B = 2b \operatorname{Im}[\phi V'(\phi)]. \quad (4.26)$$

After the onset of the oscillation  $t_{\text{osc}}$ ,  $\phi$  damps as  $\phi \propto a^{-3/2} \propto t^{-1}$ , hence the baryon number is almost fixed at  $t_{\text{osc}}$ . Integrating Eq. (4.26) to  $t_{\text{osc}}$ , we obtain the following baryon number density:

$$n_B \simeq n_B(t_{\text{osc}}) \simeq a_{\text{osc}}^{-3} \int^{t_{\text{osc}}} 2ba^3 \operatorname{Im}[\phi V'] dt \quad (4.27)$$

$$\sim \frac{2b}{H_{\text{osc}} M_*^{n-3}} m_{3/2} |\phi_{\text{osc}}|^n \sin[\arg(a_g + n\theta_{\text{osc}})] \quad (4.28)$$

$$\sim b m_{3/2} \phi_{\text{osc}}^2 \sin[\arg(a_g + n\theta_{\text{osc}})] \quad (4.29)$$

$$\sim b m_{3/2} (H_{\text{osc}} M_*^{n-3})^{2/(n-2)} \sin[\arg(a_g + n\theta_{\text{osc}})], \quad (4.30)$$

where we used Eq. (4.23) and that the rotation is driven by the A-term proportional to  $m_{3/2}$ . Thus, the baryon asymmetry is given as follows.

$$\eta_B \equiv \frac{n_B}{s} = \frac{3T_{\text{RH}}}{4} \frac{n_B(T_{\text{RH}})}{\rho_{\text{RH}}} = \frac{3T_{\text{RH}}}{4} \frac{n_B}{\rho_{\text{inf}}} \bigg|_{\text{osc}} \sim \frac{m_{3/2} T_{\text{RH}} M_*^{2(n-3)/(n-2)}}{4H_{\text{osc}}^{(2n-6)/(n-2)} M_{\text{pl}}^2}, \quad (4.31)$$

where  $T_{\text{RH}}$ ,  $\rho_{\text{RH}}$  denote the reheating temperature and radiation energy at reheating, respectively, and we used  $\rho_{\text{inf}} \simeq 3M_{\text{pl}}^2 H_{\text{osc}}^2$ , and assumed that the phase factor is  $\mathcal{O}(1)$ . For  $u^c d^c d^c$  direction,  $n = 6$ , and we can estimate the baryon asymmetry as

$$\eta_B \sim 10^{-10} \left( \frac{T_{\text{RH}}}{10^2 \text{ GeV}} \right) \left( \frac{m_\phi}{1 \text{ TeV}} \right)^{-1/2} \left( \frac{M_*}{M_{\text{pl}}} \right)^{3/2}, \quad (4.32)$$

where we used  $H_{\text{osc}} \simeq m_\phi \sim m_{3/2}$ . We can see that sufficient amount of BAU can be generated, even for very low reheating temperature, or after significant dilution after inflation.

In the next section, we study the AD dynamics when the SUSY breaking is mediated through the gauge interactions: gauge mediation case, which gives different potential to the AD field.

### 4.3.2 Gauge mediation case

In the previous section, we studied the dynamics of the AD field in the gravity mediation case and saw that it can generate the sufficient baryon asymmetry of the universe. In the gauge mediation case, SUSY breaking is mediated through gauge fields and messenger fields, which have gauge charge, and especially the soft mass is determined by the messenger mass scale  $M_m$ :  $m_\phi \sim F/M_m$ , which is typically very low,  $M_m \ll M_{\text{pl}}$ , unless there is a large hierarchy between  $\sqrt{F}$  and  $M_m$ . Thus, for large enough  $\phi$ , the gauge fields gain masses of  $\sim g|\phi| > M_m$ , and the mediation is suppressed. This leads to a smaller soft mass and this appears as the flat feature of the potential for large  $\phi$ , which is known to be

$$V_{\text{gauge}}(\phi) \sim M_F^4 \left( \log \left( \frac{|\phi|^2}{M_m^2} \right) \right)^2, \quad (4.33)$$

where the scale  $M_F$  is defined as

$$M_F \simeq \frac{\sqrt{gkF}}{4\pi}, \quad (4.34)$$

where  $g$  generically denotes the gauge coupling and  $k$  is the Yukawa coupling between messengers and the breaking sector [38]. The gravity mediation effect can still exist in the gauge mediation model (Fig. 4.2), which gives the potential  $V_{\text{grav}} \sim m_{3/2}^2 |\phi|^2$ , and gauge mediation effect dominates when

$$V_{\text{gauge}} > V_{\text{grav}}, \quad (4.35)$$

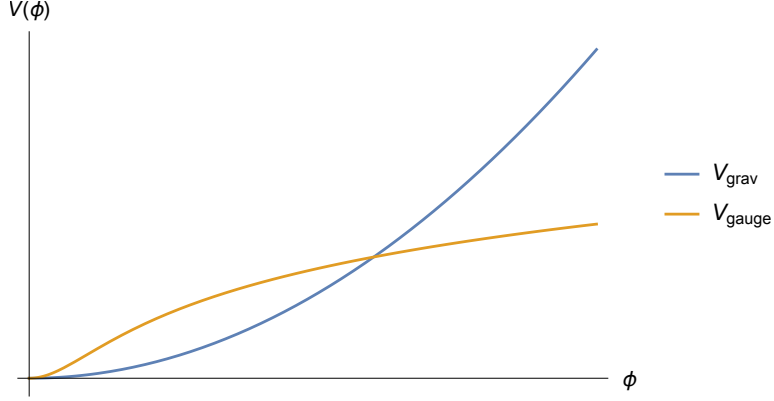


Figure 4.2: The potential in the gauge mediation model.

which is satisfied for

$$\phi_{\text{osc}} < \phi_{\text{eq}} \sim \sqrt{2} M_F^2 / m_{3/2}. \quad (4.36)$$

In this case, the AD field begins the oscillation when  $|c_H| H^2 \phi \sim V'_{\text{gauge}}$ , which gives

$$H_{\text{osc}}^2 \sim \frac{M_F^4}{\phi_{\text{osc}}^2}, \quad (4.37)$$

where Eq. (4.23) still holds for  $\phi_{\text{osc}}$ .

Since the A-term still comes from gravity mediation effect, the baryon asymmetry is still given as Eq. (4.31):

$$\eta_B \sim \frac{m_{3/2} T_{\text{RH}} M_*^{2(n-3)/(n-2)}}{4 H_{\text{osc}}^{(2n-6)/(n-2)} M_{\text{pl}}^2}. \quad (4.38)$$

However, we see from Eq. (4.36) that the following hierarchy exists:

$$m_{3/2} < H_{\text{osc}}, \quad (4.39)$$

hence the baryogenesis is less efficient than the case of the maximal rotation  $m_{3/2} \sim H_{\text{osc}}$ , with a more elliptic trajectory. In Fig. 4.3, we present an example of the dynamics of the AD field, where we set  $M_* = M_{\text{GUT}}$ ,  $m_\phi = 100$  TeV,  $m_{3/2} = 100$  keV  $\sim 10^{-2} H_{\text{osc}}$ ,  $n = 6$ ,  $\lambda = 1$ ,  $a_H = 1$ ,  $a_g = i$ . The parameter  $\epsilon \equiv m_{3/2}/H_{\text{osc}}$  is called ellipticity parameter. Nevertheless, for the proper parameters, the baryon asymmetry in the universe can be generated: Substituting Eq. (4.37) for  $H_{\text{osc}}$ , Eq. (4.38) becomes

$$\eta_B \sim \frac{m_{3/2} T_{\text{R}}}{M_{\text{pl}}^2} \left( \frac{M_*}{M_F} \right)^{4(n-3)/(n-1)}, \quad (4.40)$$

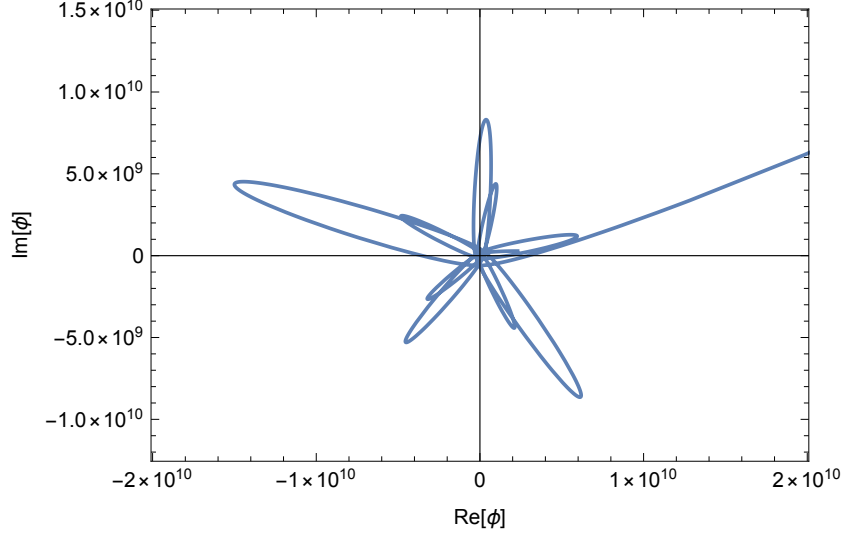


Figure 4.3: An example of AD dynamics in the gauge mediation case.

where we also used Eq. (4.23). For  $u^c d^c d^c$  direction, which is the case  $n = 6$ , it is estimated as

$$\eta_B \sim 10^{-10} \left( \frac{T_{\text{RH}}}{10^3 \text{ GeV}} \right) \left( \frac{m_{3/2}}{10^2 \text{ MeV}} \right) \left( \frac{M_F}{10^8 \text{ GeV}} \right)^{-12/5} \left( \frac{M_*}{M_{\text{pl}}} \right)^{12/5}, \quad (4.41)$$

where again sufficient amount of baryon asymmetry can be generated.

If the dynamics of the AD field begins at sufficiently large amplitude, its oscillation is governed by the gravity mediation potential, and the baryon asymmetry will be the same as the previous gravity mediation case, with  $m_\phi$  substituted by  $m_{3/2}$ : The baryon asymmetry is given as follows:

$$\eta_B \sim 10^{-10} \left( \frac{T_{\text{RH}}}{10^2 \text{ GeV}} \right) \left( \frac{m_{3/2}}{100 \text{ keV}} \right)^{-1/2} \left( \frac{M_*}{M_{\text{GUT}}} \right)^{3/2}, \quad (4.42)$$

for the case of the  $u^c d^c d^c$  direction ( $n = 6$ ).

# Chapter 5

## Q-balls

In the previous chapter, we saw that the AD mechanism gives homogeneous condensate of AD field, which may lead to sufficient amount of BAU. However, this condensate is unstable against the spatial fragmentation, and becomes localized spherical objects, called Q-balls, whose stability is guaranteed by the conservation of baryon number<sup>1</sup>. In this chapter, we review some general properties of the Q-ball solution, and study the profiles in the gravity (gauge) mediation case.

### 5.1 Q-ball solutions

#### 5.1.1 General properties

In this section, we review some general properties of the Q-ball [3], which is a stable configuration of a complex scalar field with a fixed conserved global  $U(1)$  charge, such as baryon number. Consider the following Lagrangian.

$$\mathcal{L} = \partial_\mu \Phi^* \partial^\mu \Phi - V(|\Phi|) \quad (5.1)$$

where  $V(|\Phi|)$  is a scalar potential. We renormalize the field as

$$\Phi \equiv \frac{1}{\sqrt{2}} \phi, \quad (5.2)$$

for later convenience. The global  $U(1)$  charge density  $q$  is given by

$$q = \frac{1}{2i} \left( \phi^* \dot{\phi} - \phi \dot{\phi}^* \right). \quad (5.3)$$

---

<sup>1</sup>The higher-order operator that violates the baryon number used in AD mechanism is now negligible, since the amplitude of the AD field has decreased due to the cosmic expansion.

Q-ball is defined as a solution that minimizes the energy of the system with a fixed  $U(1)$  charge. Using the Lagrange multiplier method, we minimize the following function:

$$E_\omega \equiv E + \omega \left[ Q - \frac{1}{2i} \int d^3x (\phi^* \dot{\phi} - \phi \dot{\phi}^*) \right] \quad (5.4)$$

where  $E$  is the energy, which is given as

$$E = \int d^3x \left[ \frac{1}{2} (|\dot{\phi}|^2 + |\nabla \phi|^2) + V(\phi) \right]. \quad (5.5)$$

We rewrite Eq. (5.4) as

$$E_\omega = \int d^3x \frac{1}{2} |\partial_t \phi - i\omega \phi|^2 + \int d^3x \left[ \frac{1}{2} |\nabla \phi|^2 + V_\omega(\phi) \right] + \omega Q, \quad (5.6)$$

$$V_\omega(\phi) \equiv V(\phi) - \frac{1}{2} \omega^2 |\phi|^2, \quad (5.7)$$

and by minimizing the first term, we obtain the following time dependence of  $\phi$ :

$$\phi(x, t) = e^{i\omega t} \phi(x). \quad (5.8)$$

Then, we seek for the lowest energy spherical configuration  $\phi(r)$ , which satisfies the following equation.

$$\frac{d^2 \phi}{dr^2} + \frac{2}{r} \frac{d\phi}{dr} + \left[ \omega^2 \phi(r) - \frac{\partial V(\phi)}{\partial \phi} \right] = 0, \quad (5.9)$$

with the following boundary conditions:

$$\frac{d\phi}{dr}(0) = 0, \quad \phi(\infty) = 0. \quad (5.10)$$

For examining the existence of the solution, the analogy with the classical dynamics of a point mass is useful, where we make the following redefinitions.

$$r \rightarrow t, \quad (5.11)$$

$$-V_\omega(\phi) = \frac{1}{2} \omega^2 \phi^2 - V(\phi). \quad (5.12)$$

Then, Eq. (5.9) becomes

$$\ddot{\phi} + \frac{2}{t} \dot{\phi} + \frac{\partial}{\partial \phi} (-V_\omega) = 0, \quad (5.13)$$

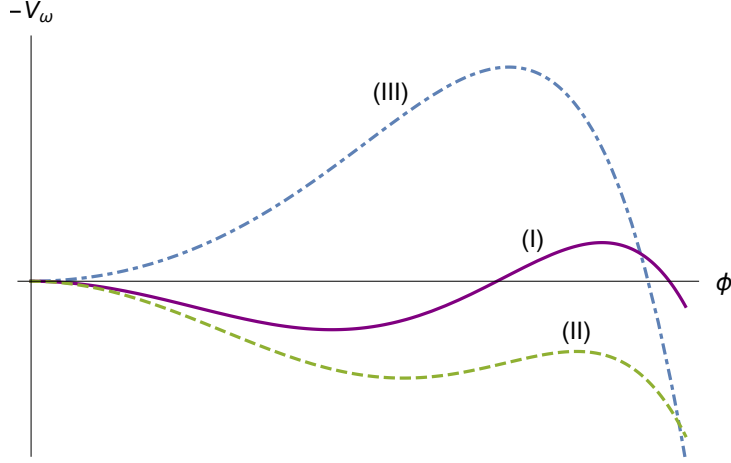


Figure 5.1: Illustration of the shapes of the potential  $-V_\omega(\phi)$  depending on  $\omega$ . (I) :  $\omega_0^2 < \omega^2 < m_\Phi^2$ , (II) :  $\omega^2 < \omega_0^2$ , (III) :  $\omega^2 > m_\Phi^2$ . The potential of type (I) gives a proper Q-ball solution.

which is analogous to the equation of motion of a classical point mass under the potential  $-V_\omega$  and the friction proportional to the velocity. The boundary conditions Eq. (5.10) become the conditions that the point mass is initially at rest and asymptotes toward the origin. For this kind of dynamics, the potential  $-V_\omega$  should have a proper shape (see Fig. 5.1), which is described by the following conditions:

$$\max[-V_\omega(\phi)] > 0, \quad (5.14)$$

$$-V_\omega''(0) < 0. \quad (5.15)$$

The first condition gives the point mass the sufficient energy to reach the origin, and the second gives the proper stopping force at the origin. These conditions are translated into those on  $\omega$  as

$$\omega_0^2 < \omega^2 < m_\Phi^2, \quad (5.16)$$

where  $\omega_0^2 \equiv \min[2V(\phi)/\phi^2]$  and  $m_\Phi^2 \equiv V''(0)$ . Thus, we see that the following relation must hold:

$$\omega_0^2 < m_\Phi^2, \quad (5.17)$$

that is, the potential must be shallower than quadratic. This is a necessary condition that it is energetically favorable when  $\phi$  condensates, since  $\omega_0$  corresponds



to the minimum of effective mass in presence of non-zero VEV of  $\phi$ . This is the existence condition of the Q-ball solution.

The following relation will also be useful:

$$\frac{dE}{dQ} = \omega, \quad (5.18)$$

which can be easily proved by varying the energy in the following way:

$$\begin{aligned} \delta E &= \int d^3x [\omega \delta\omega \phi^2 + \omega^2 \phi \delta\phi - \Delta\phi \delta\phi + V'(\phi) \delta\phi] \\ &= \omega \int d^3x [\delta\omega \phi^2 + 2\omega \phi \delta\phi] \\ &= \omega \delta Q, \end{aligned} \quad (5.19)$$

where we used Eq. (5.9). Thus, the condition Eq. (5.16) means

$$\omega_0 < \frac{dE}{dQ} < m_\Phi, \quad (5.20)$$

which implies that  $\phi$  energetically favors to condensate in Q-ball, rather than to exist as an individual particle. We will see later that this holds for electrically charged Q-balls as well.

### 5.1.2 Thin-wall approximation

If we consider the following thin-wall profile for the Q-ball (Fig. 5.2),

$$\phi = \begin{cases} \phi_0, & r < R \\ 0, & r > R \end{cases} \quad (5.21)$$

then the charge and energy of the Q-ball are given by

$$Q = \omega \phi_0^2 V_Q, \quad (5.22)$$

$$E = V_Q \left[ \frac{1}{2} \omega^2 \phi_0^2 + V(\phi_0) \right], \quad (5.23)$$

where  $V_Q$  denotes the volume of the Q-ball:  $V_Q \equiv 4\pi R^3/3$ .

Then, we can eliminate  $\omega$  by combining the above, which leads to

$$E = \frac{1}{2} \frac{Q^2}{\phi_0^2 V_Q} + V(\phi_0) V_Q, \quad (5.24)$$

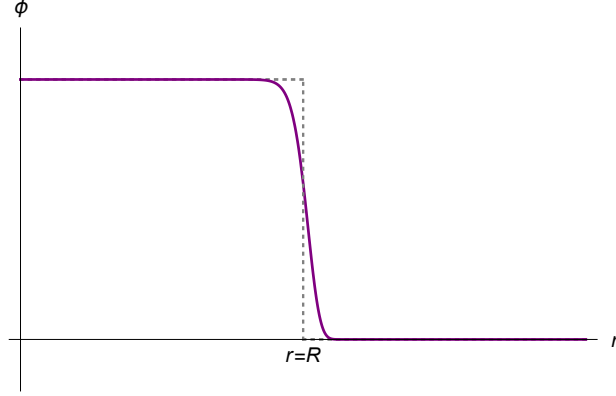


Figure 5.2: Illustration of the thin-wall profile of the Q-ball.

which must be minimized by  $V_Q$  as follows:

$$V_Q = \frac{Q}{\sqrt{2\phi_0^2 V(\phi_0)}}, \quad (5.25)$$

$$E = Q \sqrt{\frac{2V(\phi_0)}{\phi_0^2}}. \quad (5.26)$$

Finally, choosing the  $\phi_0$  that minimizes the energy gives

$$Q = V_Q \phi_0^2 \sqrt{\min \left[ \frac{2V(\phi_0)}{\phi_0^2} \right]}, \quad (5.27)$$

$$E = Q \sqrt{\min \left[ \frac{2V(\phi_0)}{\phi_0^2} \right]}. \quad (5.28)$$

Using  $\omega_0^2 = \min [2V(\phi_0)/\phi_0^2]$ , which is defined above, these become the following simple formulas:

$$Q = \omega_0 \phi_0^2 V_Q, \quad (5.29)$$

$$E = \omega_0 Q. \quad (5.30)$$

This in particular gives

$$\omega = \omega_0, \quad (5.31)$$

using  $\omega = dE/dQ$ , which implies that this is the maximally stable profile in that  $\omega$  becomes its minimum.

### 5.1.3 Q-balls in SUSY

#### Gravity mediation case

We saw that Q-ball solutions exist under certain conditions. However, the profile of a Q-ball is completely determined when we specify the potential  $V(\phi)$ . Since the Q-balls are AD condensates formed after the AD mechanism, we will consider the AD potential in the previous chapter. We will only need renormalizable  $U(1)$  invariant terms, due to the small amplitude and baryon number conservation, which gives only the soft mass term in the gravity mediated case. This quadratic potential does not allow the Q-ball solution, but if we take into account 1-loop correction coming from SUSY breaking, the potential can become shallower than quadratic, if the correction gives a negative contribution. The AD potential with 1-loop correction is given as

$$V(\phi) \simeq m_\phi^2(\mu)|\phi|^2 \left( 1 + K \log \left( \frac{|\phi|^2}{\mu^2} \right) \right), \quad (5.32)$$

where  $\mu$  is the renormalization scale and the parameter  $K$  is known to take the values of  $|K| \sim 0.01-0.1$  [39]. For negative  $K$ , the potential becomes shallower than quadratic, which allows the Q-ball solutions [40]. The Q-ball solution is derived by solving Eq. (5.9), and if we set  $\mu = \phi(0)$ , we can obtain the following simple gaussian profile:

$$\phi(r) = \phi(0) \exp[-r^2/(2R^2)], \quad (5.33)$$

where  $R \simeq |K|^{-1/2} m_\phi^{-1}$  characterizes the size of the Q-ball.

We also give the expressions for the baryon charge and energy of a gravity mediation type Q-ball:

$$Q \simeq 2\pi^{3/2} \omega \phi_0^2 R^3, \quad (5.34)$$

$$E \simeq \omega Q, \quad (5.35)$$

$$\omega = \frac{dE}{dQ} \simeq m_\phi(\phi_0), \quad (5.36)$$

with  $\phi_0 \equiv \phi(0)$ . Since  $dm_\phi(\mu)/d \ln \mu \sim K m_\phi(\mu)$  and  $K < 0$ , the mass  $m_\phi$  becomes smaller in the Q-ball, than the outside of the Q-ball:  $m_\phi(\phi_0) < m_\phi(\text{EW scale})$ , which implies that  $\phi$  energetically favors to condensate in the Q-ball.

#### Gauge mediation case

In the gauge mediation case, the AD potential is mainly given by the soft mass term, just as in the gravity mediation case. However, as mentioned in the previous

chapter, the soft mass is suppressed for energy scale larger than messenger scale and the potential becomes flat. If we approximate the potential as  $V = V_0 = \text{const.}$ , there exists the following analytic solution [7]:

$$\phi = \begin{cases} \phi_0 \sin(\omega r)/\omega r, & r < R \equiv \pi/\omega \\ 0, & r > R \end{cases} \quad (5.37)$$

whose baryon charge and energy are given as

$$Q = \phi_0^4 V_0^{-1}, \quad (5.38)$$

$$E = \frac{4\pi\sqrt{2}}{3} V_0^{1/4} Q^{3/4}. \quad (5.39)$$

This naive formula is known to fit well to the realistic case as

$$Q \simeq \zeta^{-4} \phi_0^4 M_F^{-4}, \quad (5.40)$$

$$E \simeq \frac{4\pi\sqrt{2}}{3} \zeta M_F Q^{3/4}, \quad (5.41)$$

where  $\zeta \sim \mathcal{O}(1)$  is a numerical factor [41, 42].

Then, from  $dE/dQ = \omega$ , we obtain

$$\omega \simeq \sqrt{2}\pi\zeta M_F Q^{-1/4}. \quad (5.42)$$

This implies that for a sufficiently large charge,  $dE/dQ$  may become smaller than the baryon mass  $\sim \text{GeV}$ , which kinematically forbids the decay of a baryonic Q-ball, guaranteeing its stability. This makes the Q-ball a dark matter candidate. Requiring the proper amount of Q-ball to explain the DM abundance, gives the observational constraint on the model. While the flat direction is neutral under the gauge interactions, there exists a detectable process of the Q-ball. In this process, called KKST process [8], a Q-ball absorbs a proton and emits a pion of  $\sim \text{GeV}$  through gluino exchange, which occurs since the baryon dissociates due to the  $SU(3)$  breaking inside the Q-ball. The Q-ball DM scenario in gauge mediation model is studied in Ref. [43], applying observational constraints including those on KKST process from IceCube, BAKSAN, etc.

Here we comment on another kind of stable Q-ball that can be realized in the gauge mediation model. As pointed out in the previous chapter, for a sufficiently large amplitude, the AD oscillation is governed by the gravity mediation potential:  $\sim m_{3/2}|\phi|^2$ , and this leads to the gravity mediation type Q-balls with  $m_\phi$  substituted by  $m_{3/2}$ . Then, by virtue of the hierarchy between the soft mass and gravitino mass  $m_\phi > m_{3/2}$  coming from the low breaking scale, the Q-balls can be

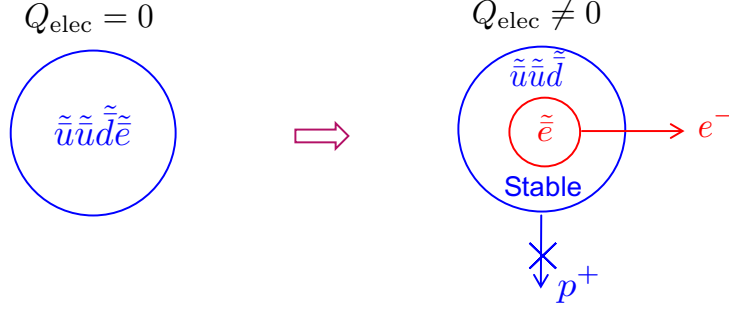


Figure 5.3: Illustration of the realization of charged Q-ball from  $B$  and  $L$  flat direction.

stable against the decay by realizing  $\omega \simeq m_{3/2} < \text{GeV}$ , which is a big difference from the ordinary gravity mediation type Q-balls. This new kind of stable Q-ball in the gauge mediation case is called New-type Q-ball, which will also be of our interest in the context of the Q-ball DM scenario.

While we saw the stability of the Q-balls in the gauge mediation model, for a leptonic Q-ball, however, the lepton charge must be larger in order to be stable against the decay, due to the smaller mass of lepton. Hence, if we consider a flat direction consisting not only of a baryonic but also of a leptonic component, such as  $u^c u^c d^c e^c$  direction, the leptonic component of Q-ball can decay into charged leptons, while the baryonic component is stable (Fig. 5.3). This induces the electric charge to the Q-ball, which forces us to take into account the gauge field configuration, since it must have non-zero configuration due to the Gauss' law, especially  $\sim Q_e/4\pi r$  at infinity, where  $Q_e$  denotes the electric charge induced to the Q-ball. This object is called charged (gauged) Q-ball, whose properties will be pursued in the following chapters. While this charged Q-ball in the gauge mediation can also be a DM candidate by virtue of the stability of the baryonic component, it is detectable through the electromagnetic processes. Since this is categorized as charged dark matter, it must clear the various observational constraints besides the DM abundance, such as BBN, bullet cluster, etc. We expect that these are safely satisfied due to the extremely heavy mass of the Q-ball (typically  $10^{20}$ - $10^{30}$  GeV), which leads to very small number density in order to satisfy the DM abundance. However, we will see later that the constraint from the direct detection of the charged DM flux is quite severe and the significant region of the model parameters is excluded, compared to the neutral Q-ball DM scenario [9, 10, 11]. This implies that a small improvement of the sensitivity either may detect the charged Q-ball DM, or gives a stronger constraint on the model. This charge Q-ball DM scenario in gauge mediation model will be one of the main issues in this thesis, which we will discuss in Chap. 7.

## 5.2 Q-ball formation after the AD mechanism

In the previous section, we studied the Q-ball solutions, especially the profiles of gravity (gauge) mediation type Q-balls and their properties. In this section, we examine the growth of the instability of AD field, which fragments into Q-balls, and estimate the typical charge of each formed Q-ball. We parametrize the AD field  $\Phi$  as

$$\Phi = \frac{1}{\sqrt{2}} R e^{i\Omega}, \quad (5.43)$$

whose equations of motion are given as follows:

$$\ddot{\Omega} + 3H\dot{\Omega} - \frac{1}{a^2(t)}\Delta\Omega + \frac{2\dot{R}}{R}\dot{\Omega}\frac{2}{a^2(t)R}(\partial_i\Omega)(\partial^i R) = 0, \quad (5.44)$$

$$\ddot{R} + 3H\dot{R} - \frac{1}{a^2(t)}\Delta R - \dot{\Omega}^2 R + \frac{1}{a^2(t)}(\partial_i\Omega)^2 R + \frac{\partial V}{\partial R} = 0. \quad (5.45)$$

If we decompose  $R$ ,  $\Omega$  into the background and linear fluctuations as

$$R = \phi(t) + \delta\phi(\mathbf{x}, t) \quad (5.46)$$

$$\Omega = \theta(t) + \delta\theta(\mathbf{x}, t), \quad (5.47)$$

the equations for the fluctuations become

$$\ddot{\delta\phi} + 3H\dot{\delta\phi} - \left(2\dot{\theta}(t)\phi(t)\dot{\delta\theta} + \delta\phi\dot{\theta}(t)^2\right) - \frac{1}{a^2(t)}\Delta\delta\phi + V''(\phi(t))\delta\phi = 0, \quad (5.48)$$

$$\phi(t)\ddot{\delta\theta} + 3H\left(\dot{\theta}(t)\delta\phi + \dot{\delta\theta}\phi(t)\right) + 2\left(\dot{\phi}(t)\dot{\delta\theta} + \dot{\delta\phi}\dot{\theta}(t)\right) - \frac{1}{a^2(t)}\phi(t)\Delta\delta\phi = 0. \quad (5.49)$$

We adopt the following parametrization.

$$\phi(t) = \left(\frac{a_{\text{osc}}}{a(t)}\right)^{3/2} \phi_{\text{osc}}, \quad (5.50)$$

$$\delta\phi = \left(\frac{a_{\text{osc}}}{a(t)}\right)^{3/2} \delta\phi_{\text{osc}} e^{i(S(t)+\mathbf{k}\cdot\mathbf{x})}, \quad (5.51)$$

$$\delta\theta = \delta\theta_{\text{osc}} e^{i(S(t)+\mathbf{k}\cdot\mathbf{x})}, \quad (5.52)$$

where we assumed matter domination due to the inflaton oscillation. Then, Eq. (5.48, 5.49) reduce to

$$\begin{pmatrix} i\ddot{S} - \dot{S}^2 + V''(\phi) - \dot{\theta}^2 + k^2/a^2 & -2i\dot{\theta}\dot{S}\phi \\ 2i\dot{\theta}\dot{S} & (i\ddot{S} - \dot{S}^2 + k^2/a^2)\phi \end{pmatrix} \begin{pmatrix} \delta\phi \\ \delta\theta \end{pmatrix} = 0, \quad (5.53)$$

whose condition for non-trivial solutions  $\delta\phi$ ,  $\delta\theta$  is obtained as follows.

$$\begin{vmatrix} i\ddot{S} - \dot{S}^2 + V''(\phi) - \dot{\theta}^2 + k^2/a^2 & -2i\dot{\theta}\dot{S}\phi \\ 2i\dot{\theta}\dot{S} & (i\ddot{S} - \dot{S}^2 + k^2/a^2)\phi \end{vmatrix} = 0, \quad (5.54)$$

which gives

$$\left(i\ddot{S} - \dot{S}^2 + V'' - \dot{\theta}^2 + \frac{k^2}{a^2}\right) \left(i\ddot{S} - \dot{S}^2 + \frac{k^2}{a^2}\right) - 4\dot{\theta}^2 \dot{S}^2 = 0. \quad (5.55)$$

Defining  $S \equiv -i\alpha(t)$ ,  $\dot{\alpha}^2 \equiv X$ , we obtain the following equation for  $X$ :

$$X^2 + \left(2\frac{k^2}{a^2} + 3\dot{\theta}^2 + V''\right)X + \frac{k^2}{a^2} \left(\frac{k^2}{a^2} + V'' - \dot{\theta}^2\right) = 0, \quad (5.56)$$

which must have the positive solution, for the instability to grow exponentially. The existence condition of the solution is

$$\frac{k^2}{a^2} + V'' - \dot{\theta}^2 < 0, \quad (5.57)$$

and the maximally growing mode is given as

$$\frac{k_{\max}^2}{a^2} = \frac{1}{16\dot{\theta}^2} \left(-V'' - V''\dot{\theta}^2 + 7\dot{\theta}^4\right), \quad (5.58)$$

which corresponds to the typical size of the formed Q-balls. In the following subsection, we will make use of these formulas for the gravity (gauge) mediation case and estimate the typical size and charge of the formed Q-balls in each case.

### 5.2.1 Gravity mediation case

Using the following gravity mediation potential,

$$V(\phi) \simeq m_\phi^2(\mu)|\phi|^2 \left(1 + K \log \left(\frac{|\phi|^2}{\mu^2}\right)\right), \quad (5.59)$$

and assuming the maximal rotation:  $\dot{\theta}^2 \sim m_{\text{eff}}^2 \sim m_\phi^2 (1 + K + K \log(|\phi|^2/\mu^2))$ , we obtain the following instability band:

$$0 \lesssim \frac{k^2}{a^2} \lesssim 2m_\phi^2|K|, \quad (5.60)$$

whose maximal growth mode becomes

$$\frac{k_{\max}^2}{a^2} \simeq m_\phi^2|K|, \quad (5.61)$$

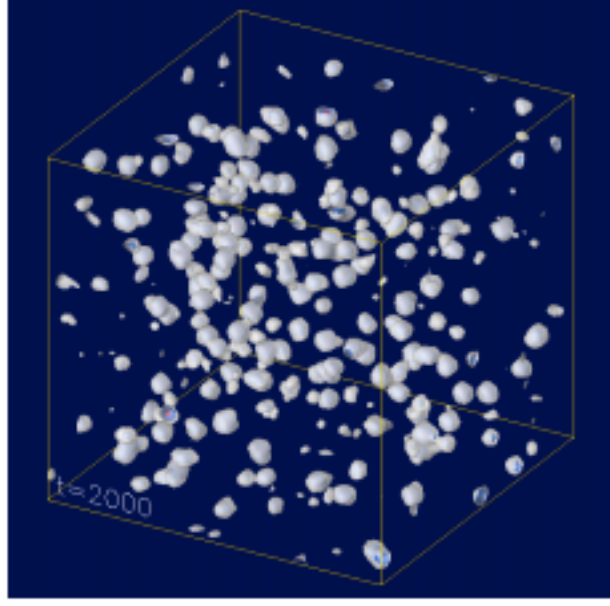


Figure 5.4: A result of numerical simulation of Q-ball formation [44].

which coincides with the size of the gravity mediation type Q-ball, which was derived in the previous chapter.

The typical charge of the formed Q-balls is estimated as follows.

$$Q \simeq \frac{4}{3}\pi R^3 \times n_B(t_{\text{form}}) \quad (5.62)$$

$$\simeq \frac{4}{3}\pi \left( \frac{k_{\text{max}}}{a_{\text{form}}} \right)^{-3} \left( \frac{a_{\text{osc}}}{a_{\text{form}}} \right)^3 n_B(t_{\text{osc}}) \quad (5.63)$$

$$\sim \alpha |K|^{-3/2} \left( \frac{\phi_{\text{osc}}}{m_\phi} \right)^2, \quad (5.64)$$

where  $\alpha \equiv (a_{\text{osc}}/a_{\text{form}})^3$  and we used Eq. (4.29):  $n_B(t_{\text{osc}}) \sim m_{3/2}\phi_{\text{osc}}^2$ ,  $H_{\text{osc}} \sim m_{3/2} \sim m_\phi$ . It is difficult to analyze the dilution factor  $\alpha$ , while numerical simulations [44, 45] (Fig. 5.4) suggest that

$$Q \sim \beta \left( \frac{\phi_{\text{osc}}}{m_\phi} \right)^2, \quad (5.65)$$

with  $\beta \sim 2 \times 10^{-2}$  for  $|K| = 0.1$  and maximal rotation of AD field, whose behavior is consistent with the above estimation.

Then, in the case of  $n = 6$ , for instance, we obtain the following estimation for



the typical charge of the formed Q-balls.

$$Q \sim 10^{21} \left( \frac{m_\phi}{\text{TeV}} \right)^{-3/2} \left( \frac{M_*}{M_{\text{pl}}} \right)^{3/2}, \quad (5.66)$$

where we used Eq. (4.23).

### 5.2.2 Gauge mediation case

Just as in the gravity mediation case, using the gauge mediation potential Eq. (4.33) and assuming the maximal rotation, we can again obtain the following growth mode:

$$\frac{k_{\text{max}}^2}{a^2} \sim \frac{M_F^4}{\phi^2}, \quad (5.67)$$

where, again, we can see the correspondence between the growth mode and the size of the gauge mediation type Q-ball in the previous chapter. Then, we can estimate the typical charge of the formed Q-balls as

$$Q \simeq \frac{4}{3} \pi R^3 \times n_B(t_{\text{form}}) \quad (5.68)$$

$$\sim \left( \frac{M_F^4}{\phi_{\text{form}}^2} \right)^{-3/2} \left( \frac{a_{\text{osc}}}{a_{\text{form}}} \right)^3 n_B(t_{\text{osc}}) \quad (5.69)$$

$$\sim \alpha^4 \epsilon \left( \frac{\phi_{\text{osc}}}{M_F} \right)^4, \quad (5.70)$$

where we used  $n_B(t_{\text{osc}}) \sim m_{3/2} \phi_{\text{osc}}^2$ ,  $H_{\text{osc}}^2 \sim M_F^4 / \phi_{\text{osc}}^2$ , and  $\epsilon = m_{3/2} / H_{\text{osc}}$ . We also used  $\phi \propto a^{-3}$ , coming from the virial relation for the oscillation under the logarithmic potential. Numerical simulations [45] suggest that

$$Q \sim \beta \left( \frac{\phi_{\text{osc}}}{M_F} \right)^4, \quad (5.71)$$

with  $\beta \sim 6 \times 10^{-5}$  for  $\epsilon \lesssim 0.06$ . For  $n = 6$ , this gives

$$Q \sim 10^{24} \left( \frac{m_{3/2}}{\text{MeV}} \right) \left( \frac{M_F}{10^6 \text{ GeV}} \right)^{-4} \left( \frac{M_*}{M} \right)^3, \quad (5.72)$$

where again we used Eq. (4.23).

If the gravity mediation effect dominates over the gauge mediation effect, new-type Q-balls are expected to be formed, as pointed out in the previous section, whose typical charge becomes the same formula as in the case of gravity mediation with  $m_\phi \rightarrow m_{3/2}$ . We will use these formulas for the typical charge of gauge mediation- and new-type Q-balls in Chap. 7.

# Chapter 6

## Charged Q-balls

In the previous chapter, we reviewed Q-ball solution and its properties, which from now on we call global Q-ball, since it is the lowest-energy configuration in the global  $U(1)$  theory. However, our main interest is the electrically charged Q-ball, which is expected to have gauge field configuration due to the Gauss' law. This charged Q-ball, which is also called gauged Q-ball, is a generalization of global Q-ball solution to the local  $U(1)$  complex scalar theory, whose existence was originally pointed out in Ref. [46]. In this chapter, we briefly review on the charged (gauged) Q-ball solution and its basic properties.

### 6.1 Charged Q-ball solution and its properties

We consider a local  $U(1)$  theory of a complex scalar field, whose Lagrangian is given as

$$\mathcal{L} = (D_\mu \Phi)^* D^\mu \Phi - V(\Phi) - \frac{1}{4} F_{\mu\nu} F^{\mu\nu}, \quad (6.1)$$

$$D_\mu \equiv \partial_\mu - ieA_\mu \quad (6.2)$$

where  $V(\Phi)$  is a scalar potential. We set an ansatz that parametrizes the scalar field in the same way as the case of global Q-ball:

$$\Phi \equiv \frac{1}{\sqrt{2}} \phi, \quad (6.3)$$

$$\phi(x, t) = e^{i\omega t} \phi(r). \quad (6.4)$$

We also give an ansatz for the gauge field as follows.

$$A_0 = A_0(r), \quad (6.5)$$

$$A_i = 0, \quad (6.6)$$

since we want a spherical electrostatic solution. The equations of motion then give the following equations for the profile:

$$\frac{d^2\phi}{dr^2} + \frac{2}{r} \frac{d\phi}{dr} + \phi g^2 - \frac{dV}{d\phi} = 0, \quad (6.7)$$

$$\frac{d^2g}{dr^2} + \frac{2}{r} \frac{dg}{dr} - e^2 \phi^2 g = 0, \quad (6.8)$$

where we have defined  $g \equiv \omega - eA_0$ . In order to find a localized solution, we set the following boundary conditions,

$$\phi(\infty) = 0, \quad \frac{d\phi}{dr}(0) = 0, \quad (6.9)$$

$$g(\infty) = \omega, \quad \frac{dg}{dr}(0) = 0, \quad (6.10)$$

which also give the boundary condition for the gauge field to vanish at infinity. Eq. (6.8) can be rewritten as

$$(r^2 g')' = e^2 r^2 \phi^2 g, \quad (6.11)$$

which actually implies that the absolute value of  $g$  always increases.

Then, we can do some analogy with the classical point mass, in a similar way as in the case of global Q-ball. If we treat  $r$  as a time variable, Eq. (6.7) becomes the classical equation of motion under the potential  $-V_g \equiv -V + \frac{1}{2}g^2\phi^2$ . Since  $g^2$  monotonically increases, the effective mass term  $g^2\phi^2/2$  lifts up the potential along with the time, playing the role of a time-varying external force. This can make the particle reach the origin, which is necessary due to the boundary condition Eq. (6.9). However, the boundary condition also states that the point mass must asymptote to the origin, which corresponds to the localization condition of the solution. Hence, we need the proper stopping force at the origin, which leads to

$$m_\Phi > \omega, \quad (6.12)$$

where  $m_\Phi^2 \equiv V''(0)$ . This is the existence condition of the charged (gauged) Q-ball solution.

Note that while Eq. (6.12) partly coincides with the existence condition of the global Q-ball, there is no condition corresponding to Eq. (5.14), which was necessary to give sufficient energy to reach the origin. This is because the potential is lifted up by the external force, which drives the motion to the origin. This especially allows the non-monotonic profile, since the point mass can reach the origin even if it initially moves away from the origin. This non-monotonic feature of the profile can be understood as the electric repulsion that pushes the scalar

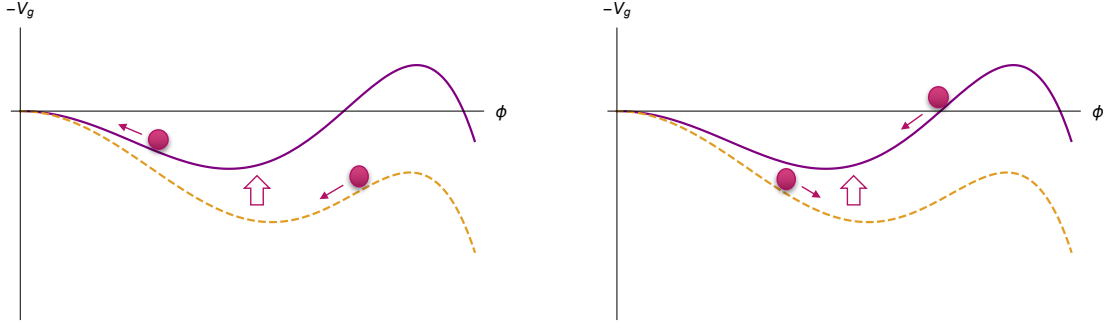


Figure 6.1: Analogy with the classical point mass

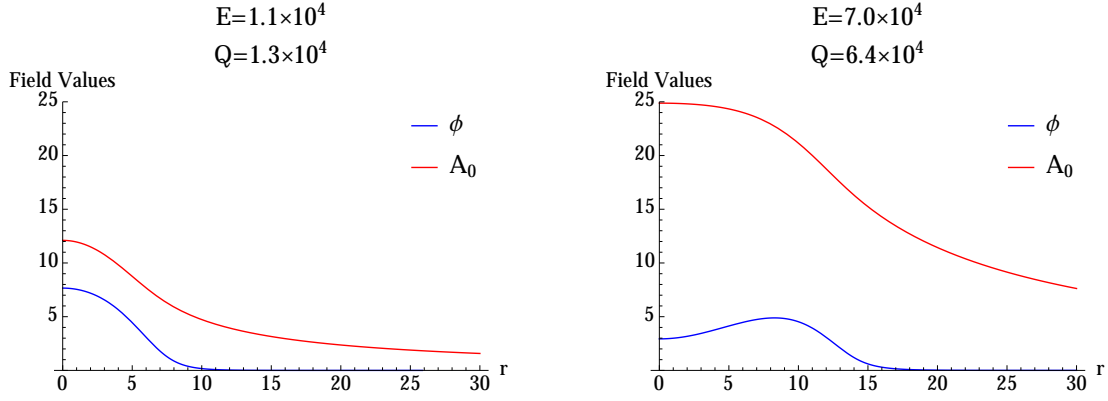


Figure 6.2: charged Q-balls in gauge mediation-like model with  $e^2 = 0.002$  and  $m_\Phi = 1$ .

field towards the surface. We show the examples of the profiles in Fig. 6.2, where indeed the non-monotonic feature arises for a larger electric charge. Here as the scalar potential, we used  $V(\Phi) = m_\Phi^4 \log[1 + \Phi^2/m_\Phi^2]$ , which is usually adopted as an approximate form of the gauge mediation potential. Since we are mainly interested in the Q-balls in the gauge mediation model due to the stability of them, we will frequently use this potential, especially in the numerical calculation.

We also show that the following relation holds for charged Q-ball as well,

$$\frac{dE}{dQ} = \omega, \quad (6.13)$$

in a similar way as for global Q-ball [47]: The energy of the charged Q-ball is given by

$$E = \int d^3x \left[ \frac{1}{2}(\nabla\phi)^2 + \frac{1}{2}(\nabla A_0)^2 + \frac{1}{2}\phi^2(\omega - eA_0)^2 + V(\phi) \right], \quad (6.14)$$

whose variation becomes

$$\begin{aligned}
\delta E &= \int d^3x \left[ -\Delta\phi\delta\phi - A_0\delta\Delta A_0 + \phi\delta\phi(\omega - eA_0)^2 + (\omega - eA_0)\delta(\omega - eA_0)\phi^2 + V'\delta\phi \right] \\
&= \int d^3x \left[ 2\phi\delta\phi(\omega - eA_0)^2 + (\omega - eA_0)\delta(\omega - eA_0)\phi^2 - A_0\delta\Delta A_0 \right] \\
&= \int d^3x \left[ (\omega - eA_0)\delta q - A_0\delta\Delta A_0 \right] \\
&= \omega\delta Q - \int d^3x \left[ eA_0\delta q + A_0\delta\Delta A_0 \right] \\
&= \omega\delta Q,
\end{aligned} \tag{6.15}$$

where we used Eqs. (6.7) and (6.8), and that the electric charge of the charged Q-ball is given by

$$Q \equiv \int q d^3x \tag{6.16}$$

$$= \int d^3x (\omega - eA_0)\phi^2. \tag{6.17}$$

Thus, we can see that this gives the relation  $dE/dQ = \omega$ , just as in the case of global Q-ball.

We comment on the size of a charged Q-ball of gauge mediation type. Since the large gauge mediation type Q-ball has following approximate analytic solution,

$$\phi(r) = \begin{cases} \phi_0 \sin \omega r / \omega r, & (r \leq R \equiv \pi/\omega) \\ 0, & (r > R) \end{cases} \tag{6.18}$$

the second derivative of  $\phi$  becomes singular at  $r = R$ , which for actual Q-balls, becomes a peak of  $\phi''(r)$ . We define the size of a charged Q-ball as the point where  $\phi'''(r) = 0$  as well, even if the profile is somewhat pushed outward by the electric repulsion, as shown in Fig. 6.3. Indeed, we can see that  $\phi''(r = R)$  becomes singular for a large charged Q-ball, just as for the global Q-ball, even when the Coulomb potential has a non-negligible effect on the profile.

Adopting the above identification of the size of a charged Q-ball, we present  $\omega$  and the size  $R$  as a function of  $Q$  in Fig. 6.4. We can see that in contrast to the behavior of  $\omega$  for global Q-balls, which is denoted by a dashed line,  $\omega$  increases as the charge grows, due to electric repulsion. We also plot Coulomb energy at the surface of Q-ball,  $e^2 Q / 4\pi R$  by a dotted line, whose contribution also becomes large as charge grows. However, we see that the Coulomb energy stays smaller than  $\omega$ , due to the growth of  $\omega$ , and also of  $R$  by electric repulsion, which we illustrate in Fig. 6.4 (Right).

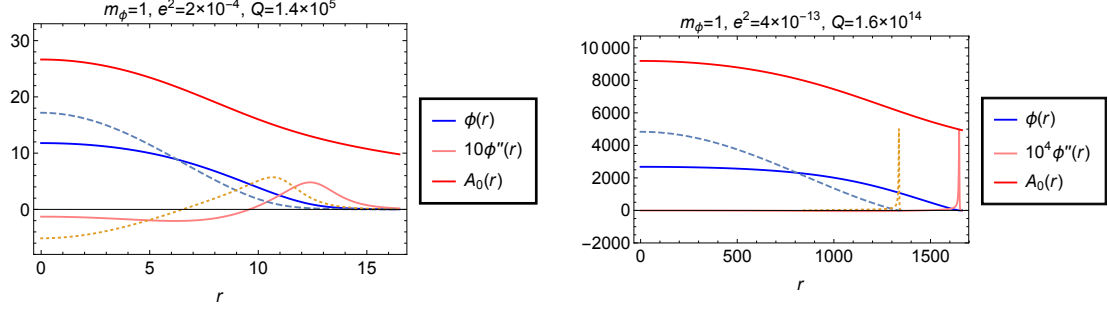


Figure 6.3: Identification of the size of the gauge mediation type charged Q-ball. The dashed line denotes the global Q-ball with the same charge. We can see that  $\phi''(r=R)$  becomes singular for a large charged Q-ball, just as for a global Q-ball, even when the Coulomb potential has a non-negligible effect on the profile.

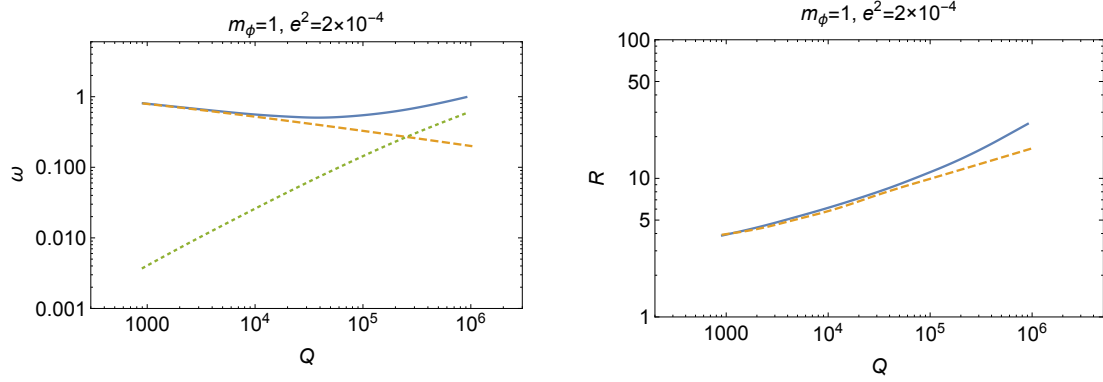


Figure 6.4: The plots of  $\omega = dE/dQ$  and  $R$  as functions of  $Q$ . We plot those for global Q-balls by dashed lines, for comparison. We see that  $\omega$  and  $R$  become large as the charge grows, due to the electric repulsion. We also present the Coulomb energy at the surface,  $e^2 Q/4\pi R$ , which is denoted by a dotted line in the left figure.

# Chapter 7

## Charged Q-ball dark matter from $B$ and $L$ direction

In the previous chapter, we reviewed some basic properties of charged Q-ball solution, which is a localized configuration consisting of a complex scalar field and  $U(1)$  gauge field. In this chapter, we consider the charged Q-ball solution with two complex scalars, in order to characterize the baryonic and leptonic components of the flat direction, which we expect to be electrically charged via the decay of leptonic component only. We numerically examine the existence of the charged Q-ball solution in our two scalar model and investigate the scenario where these charged Q-balls contribute to the main component of the dark matter in the present universe [9, 10, 11]. For the stability of the baryonic component, we consider the Q-balls in the gauge mediation model.

### 7.1 Charged Q-balls in two scalar model

We consider two complex scalar fields  $\Phi_1$ ,  $\Phi_2$ , which characterize the baryonic and leptonic component of the following  $\Phi_1\Phi_2$  flat direction,

$$\Phi_1 = \Phi_2 \equiv \Phi, \quad (7.1)$$

respectively. Then, the Lagrangian is written as follows:

$$\mathcal{L} = (D_\mu \Phi_1)^* D^\mu \Phi_1 + (D_\mu \Phi_2)^* D^\mu \Phi_2 - V(\Phi_1, \Phi_2) - \frac{1}{4} F_{\mu\nu} F^{\mu\nu}, \quad (7.2)$$

$$D_\mu \Phi_1 = (\partial_\mu - ieA_\mu) \Phi_1, \quad (7.3)$$

$$D_\mu \Phi_2 = (\partial_\mu + ieA_\mu) \Phi_2, \quad (7.4)$$

where we assigned  $\Phi_1$ ,  $\Phi_2$  the opposite electric, or local  $U(1)$  charge, since the flat direction  $\Phi_1\Phi_2$  is neutral under the gauge interaction. The baryon and lepton

charges are given as

$$B = \frac{1}{i} \int d^3x (\Phi_1^* D_0 \Phi_1 - \Phi_1 (D_0 \Phi_1)^*) \equiv \int d^3x b, \quad (7.5)$$

$$L = \frac{1}{i} \int d^3x (\Phi_2^* D_0 \Phi_2 - \Phi_2 (D_0 \Phi_2)^*) \equiv \int d^3x l, \quad (7.6)$$

where  $b$  and  $l$  are baryon and lepton number densities, which gives the total electric charge as

$$Q = B - L. \quad (7.7)$$

Note that this  $Q$  differs from that in the previous chapter, where we used  $Q$  as the baryon charge.

In order to find the charged Q-ball solution, we give the same ansatz as in the previous chapter:

$$\Phi_i \equiv \frac{1}{\sqrt{2}} \phi_i, \quad i = 1, 2 \quad (7.8)$$

$$\phi_1(x, t) = e^{i\omega_1 t} \phi_1(r), \quad (7.9)$$

$$\phi_2(x, t) = e^{i\omega_2 t} \phi_2(r), \quad (7.10)$$

$$A_i = 0, \quad (7.11)$$

$$A_0 = A_0(r). \quad (7.12)$$

Then, we obtain the following equations for the profiles,

$$\frac{d^2 \phi_1}{dr^2} + \frac{2}{r} \frac{d\phi_1}{dr} + \phi_1 (\omega_1 - eA_0)^2 - \frac{\partial V}{\partial \phi_1} = 0, \quad (7.13)$$

$$\frac{d^2 \phi_2}{dr^2} + \frac{2}{r} \frac{d\phi_2}{dr} + \phi_2 (\omega_2 + eA_0)^2 - \frac{\partial V}{\partial \phi_2} = 0, \quad (7.14)$$

$$\frac{d^2 A_0}{dr^2} + \frac{2}{r} \frac{dA_0}{dr} + e\phi_1^2 (\omega_1 - eA_0) - e\phi_2^2 (\omega_2 + eA_0) = 0, \quad (7.15)$$

where we also set the same boundary conditions as for the one scalar charged Q-ball:

$$\phi_1(\infty) = \phi_2(\infty) = 0, \quad (7.16)$$

$$\frac{d\phi_1}{dr}(0) = \frac{d\phi_2}{dr}(0) = 0, \quad (7.17)$$

$$A_0(\infty) = \frac{dA_0}{dr}(0) = 0. \quad (7.18)$$



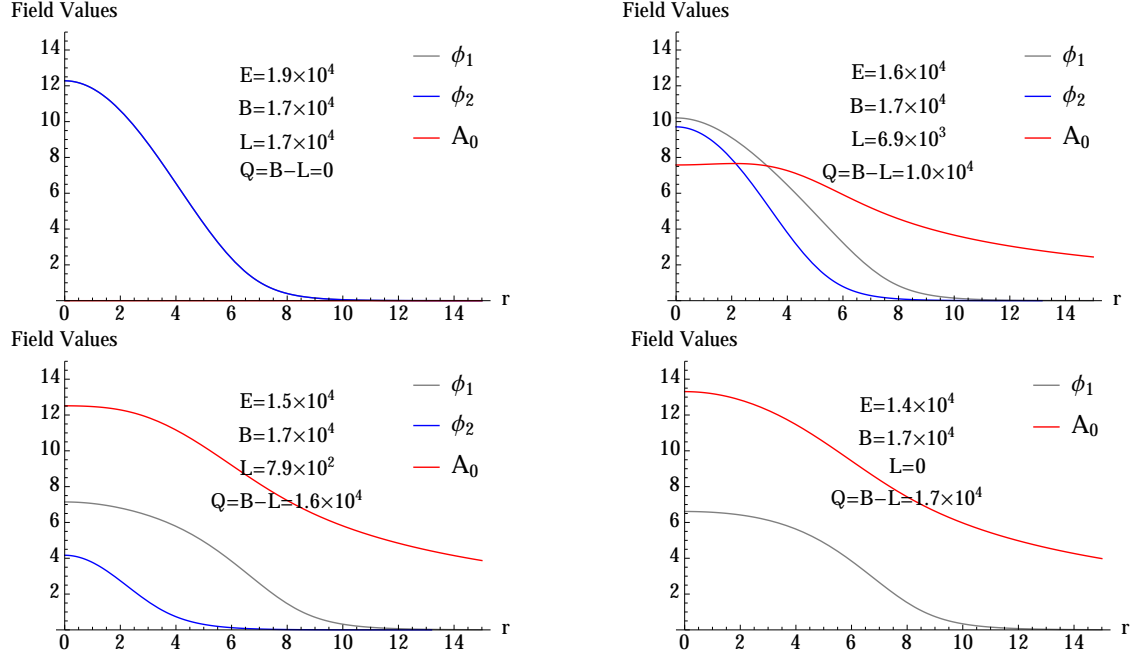


Figure 7.1: Two scalar charged Q-balls in gauge mediation model with  $e^2 = 0.002$ ,  $m_\Phi = 1$  and  $B = 1.7 \times 10^4$ .

We numerically solved the equations and confirmed the existence of the two scalar charged Q-ball solutions. In Fig. 7.1, we present the examples of the profiles with the same baryon charges and different lepton charges. Here we used the following approximate form of the gauge mediation potential:

$$V(\Phi_1, \Phi_2) = m_{\Phi_1}^4 \log \left( 1 + \frac{|\Phi_1|^2}{m_{\Phi_1}^2} \right) + m_{\Phi_2}^4 \log \left( 1 + \frac{|\Phi_2|^2}{m_{\Phi_2}^2} \right) + \frac{e^2}{2} (|\Phi_1|^2 - |\Phi_2|^2)^2, \quad (7.19)$$

where we simply assumed  $m_{\Phi_1} = m_{\Phi_2} \equiv m_\Phi$ , and we set  $e^2 = 0.002$ ,  $m_\Phi = 1$ . Note that we included the D-term, coming from the violation of D-flat condition.

We prove here

$$\left( \frac{\partial E}{\partial B} \right)_L = \omega_1, \quad (7.20)$$

$$\left( \frac{\partial E}{\partial L} \right)_B = \omega_2, \quad (7.21)$$

in the similar way as in the previous chapter, where we vary the energy

$$E = \int d^3x \left[ \frac{1}{2} (\nabla \phi_1)^2 + \frac{1}{2} (\nabla \phi_2)^2 + \frac{1}{2e^2} (e \nabla A_0)^2 + \frac{1}{2} \phi_1^2 (\omega_1 - e A_0)^2 + \frac{1}{2} \phi_2^2 (\omega_2 + e A_0)^2 + V(\phi_1, \phi_2) \right], \quad (7.22)$$

as

$$\begin{aligned}
\delta E &= \int d^3x \left[ -\Delta\phi_1\delta\phi_1 - \Delta\phi_2\delta\phi_2 - A_0\delta\Delta A_0 + \frac{\partial V}{\partial\phi_1}\delta\phi_1 + \frac{\partial V}{\partial\phi_2}\delta\phi_2 \right] \\
&+ \int d^3x \left[ \phi_1\delta\phi_1(\omega_1 - eA_0)^2 + \phi_1^2(\omega_1 - eA_0)\delta(\omega_1 - eA_0) \right] \\
&+ \int d^3x \left[ \phi_2\delta\phi_2(\omega_2 + eA_0)^2 + \phi_2^2(\omega_2 + eA_0)\delta(\omega_2 + eA_0) \right] \\
&= \int d^3x \left[ (\omega_1 - eA_0)\delta b + (\omega_2 + eA_0)\delta l - A_0\delta\Delta A_0 \right] \\
&= \omega_1\delta B + \omega_2\delta L + \int d^3x A_0 [e(-\delta b + \delta l) - \delta\Delta A_0] \\
&= \omega_1\delta B + \omega_2\delta L,
\end{aligned} \tag{7.23}$$

where we used Eqs. (7.13), (7.14), and (7.15). This can be easily generalized into the case of an arbitrary number of scalar fields.

## 7.2 Charged Q-ball dark matter scenario

In the previous section, we considered charged Q-balls in the two scalar model, in order to characterize the baryonic and leptonic components of flat direction. These can emerge through the decay of the leptonic component only, which induces the electric charge on the Q-balls. However, there is an upper bound on the electric charge of the Q-ball, which mainly comes from the Schwinger limit. We estimate this maximal value of the electric charge of the charged Q-ball. Then, we roughly pursue their evolution, especially the time of the recombination with the other light charged particles. The present relics are expected to behave as extremely heavy atom (ion)-like objects, to which we apply the currently most stringent constraint coming from the MICA direct detection.

### 7.2.1 Maximal electric charge

Here we estimate the maximal electric charge of the charged Q-ball. This upper bound is mainly due to the Schwinger limit, since the strong enough electric field near the charged Q-ball will induce the electron-positron pair-production, which will prevent further growth of the electric charge. The pair-production occurs at scale of  $\sim 1/m_e$ , and the electric field must be of about that scale. The maximal value of the electric field is known to be

$$E_S \sim \frac{m_e^2}{e}, \tag{7.24}$$

and the pair-production occurs when the electric field at the distance of  $\sim 1/m_e$  reaches this value:

$$\frac{m_e^2}{e} \sim \frac{eQ}{4\pi m_e^{-2}}, \quad (7.25)$$

which gives the following maximal electric charge of the charged Q-ball:

$$Q \sim \frac{4\pi}{e^2} = \alpha^{-1} \sim \mathcal{O}(100). \quad (7.26)$$

Here we used that the size of the Q-ball ( $\sim \text{fm}$ ), especially in our region for the DM scenario, is smaller than the Compton length  $\sim 1/m_e$  ( $\sim \text{pm}$ ), hence the electric field at  $r \sim 1/m_e$  behaves as  $\sim 1/r^2$ .

In the following, we will pursue the evolution of the charged Q-balls with the electric charge of about  $\mathcal{O}(100)$ .

### 7.2.2 Evolution of Charged Q-balls until the present

We assume that the positively charged Q-balls and negatively charged anti-Q-balls with  $|Z_Q| \sim \alpha^{-1} \sim \mathcal{O}(100)$  are formed well before the BBN, and we suppose that they account for dark matter of the universe, i.e:

$$\frac{\rho_{\text{Q-ball}}}{s} + \frac{\rho_{\text{anti-Q-ball}}}{s} = \frac{\rho_{\text{DM}}}{s} \simeq 4.4 \times 10^{-10} \text{ GeV} \quad (7.27)$$

where  $\rho_{\text{DM}}$  and  $s$  are the dark matter energy density and entropy density in the present universe, respectively. Since the Q-ball size is smaller than the Bohr radius, which is larger than the Compton scale, the charged Q-ball captures the light charged particles, just as the ordinary nucleus<sup>1</sup>. Since the number densities of (anti-) Q-balls must be extremely small in order to become the dark matter, due to their heavy masses (See footnote 1), the recombination does not affect the abundance of the other particle species and does not ruin the BBN.

Even if the usual recombination is realized, the present relics may not be completely neutral. This is because the charged Q-balls with  $Z_Q \sim +\mathcal{O}(100)$  has a smaller binding energy than that of the proton, due to the screening by orbiting electrons, so that the free electrons are mainly captured by the protons at eV. Thus, we expect that the present relics of the positively charged Q-balls can be treated as atoms or ions with  $+\mathcal{O}(1)$  charge. The negatively charged anti-Q-balls attract the nuclei including protons and heliums. However, they are expected to

---

<sup>1</sup>Since the Q-balls are extremely heavy and the number densities are very small, we can safely ignore the (Q-ball)+(anti-Q-ball) reactions. For example, the typical gauge mediation type Q-ball has the baryon charge  $B \sim 10^{30}$  and mass  $M \sim M_F B^{3/4} \sim 10^{28} \text{ GeV}$  for  $M_F \sim 10^6 \text{ GeV}$ .

collide with the core, since the Bohr radius of the nucleus is smaller than the Q-ball size. This collision leads to the annihilation of baryon charge while the electric charge remains to be  $\mathcal{O}(100)$  through the leptonic decay. However, due to the large baryon number of each Q-ball, its decrease is expected to be negligible, hence the present relics become the objects like bare nuclei with negative  $\mathcal{O}(100)$  charges.

### 7.2.3 Constraints from MICA direct detection

Since the charged Q-ball relics behave as massive atomic objects, they are detectable through the usual electromagnetic processes, unlike the global Q-balls. Various experiments that are sensitive to electromagnetic processes and the upper bounds on the flux of the charged Q-ball relics are presented in Ref. [48]. The most stringent comes from the direct detection in MICA experiment [49],

$$F \lesssim 2.3 \times 10^{-20} \text{ cm}^{-2} \text{ s}^{-1} \text{ sr}^{-1}, \quad (7.28)$$

where they reported the non-observation of any trails of heavy atom (ion)-like object in  $10^9$  years old ancient mica crystals. Since detection time effectively becomes the age of the mica, its constraint is much severer than those from other experiments. The experiment was originally designed to detect the monopole flux, which forms the bound states with  $^{27}\text{Al}$  or other elements on earth, through the monopole-dipole interaction. These bound states can be treated as massive atomic objects, which are detectable, since the detector is designed to be sensitive to atoms and ions with  $Z \gtrsim 10$ . Relics from positively charged Q-balls can also be treated as massive  $+\mathcal{O}(1)$  charged ions with  $Z \sim \mathcal{O}(100)$ , which are detectable as well. Relics from negatively charged anti-Q-balls are similar to nuclei of  $-\mathcal{O}(100)$  charges. It is not clear if the detector is sensitive to these objects, since the stopping power in the experiment is fitted to the cases of ordinary atomic objects [50]. But even if the detector is sensitive to these objects, the constraint on the mass will nearly be the same as when we ignored their flux, since the number of Q-balls and anti-Q-balls are of the same order and the detector will not be able to identify the origins of the signals, only if each stopping power has exceeded the threshold. This is also the case for monopoles, where the detector cannot identify whether  $^{27}\text{Al}$  or  $^{55}\text{Mn}$  is captured to the monopole. In any case, dark matter flux will be given as follows:

$$F \simeq \frac{\rho_{\text{DM}\odot}}{M_Q} v \quad (7.29)$$

where  $\rho_{\text{DM}\odot}$  denotes the dark matter energy density in the vicinity of the solar system, and  $v$  is the velocity of them. Then, using the observational values  $\rho_{\text{DM}\odot} \sim 0.3 \text{ GeV}/\text{cm}^3$  and  $v \sim 10^{-3}$ , we obtain the following constraint on the mass of (anti-) Q-ball relics:

$$M_Q \gtrsim 3.9 \times 10^{26} \text{ GeV}. \quad (7.30)$$

We apply this observational constraint to the model parameters, which govern the properties of Q-ball, especially its mass. Since there can be two types of Q-ball in the gauge mediation model (see Sec. 5.1.3), which can be both stable until the present, we apply the above constraint from MICA for each case in the following.

### Gauge mediation type Q-balls

The MICA constraint on the charged Q-ball mass is translated into that on the model parameter  $M_F$  and the baryon charge  $Q$  of each Q-ball, which is determined by the AD amplitude  $\phi_{\text{osc}}$  through Eq. (5.71). This AD amplitude also determines the initial energy of the Q-balls, which is diluted by the cosmic expansion until the present as

$$\frac{\rho_Q}{s} \sim \frac{3T_{\text{RH}}}{4} \frac{M_Q n_\phi / Q}{3H_{\text{osc}}^2 M_{\text{P}}^2} \sim \frac{3\pi}{2} \zeta \beta^{-1/4} T_{\text{RH}} \frac{\phi_{\text{osc}}^2}{M_{\text{P}}^2}, \quad (7.31)$$

where  $n_\phi = m_{\text{eff}} \phi_{\text{osc}}^2$ ,  $m_{\text{eff}} \simeq 2\sqrt{2}M_F^2/\phi_{\text{osc}}$ ,  $3H_{\text{osc}} \simeq m_{\text{eff}}$ , and Eq. (5.41) are used [45]. If we require this to give the present DM abundance  $\rho_{\text{DM}}/s \simeq 4.4 \times 10^{-10}$  GeV, the reheating temperature  $T_{\text{RH}}$  is related to  $\phi_{\text{osc}}$  as follows:

$$\phi_{\text{osc}} \simeq 4.3 \times 10^{12} \text{ GeV} \left( \frac{\zeta}{2.5} \right)^{-1/2} \left( \frac{\beta}{6 \times 10^{-5}} \right)^{1/8} \left( \frac{T_{\text{RH}}}{\text{GeV}} \right)^{-1/2}. \quad (7.32)$$

Then, the MICA constraint Eq. (7.30) becomes

$$T_{\text{RH}} \lesssim 4.5 \times 10^{-2} \text{ GeV} \left( \frac{\zeta}{2.5} \right)^{-1/3} \left( \frac{\beta}{6 \times 10^{-5}} \right)^{3/4} \left( \frac{M_F}{10^6 \text{ GeV}} \right)^{-4/3}, \quad (7.33)$$

where we also used Eq. (5.71). This can be shown in  $M_F$ - $T_{\text{RH}}$  plane, which we present in Fig. 7.2. The reheating temperature is plotted for  $T_{\text{RH}} > \text{MeV}$ , which is the lower bound from the BBN. The MICA constraint Eq. (7.33) corresponds to the solid line in the figure. The allowed parameter region is also determined by the additional conditions that also apply to the case of global Q-ball DM:

The horizontal dotted lines indicate the condition that the gauge mediation effect dominates the potential of the Q-ball (see Eq. (4.36)):

$$\phi_{\text{osc}} < \phi_{\text{eq}} \sim \sqrt{2}M_F^2/m_{3/2}. \quad (7.34)$$

Then, using Eq. (7.32), Eq. (7.34) becomes

$$T_{\text{RH}} \gtrsim 1.3 \times 10^{-8} \text{ GeV} g^{-2} k^{-2} \left( \frac{\zeta}{2.5} \right)^{-1} \left( \frac{\beta}{6 \times 10^{-5}} \right)^{1/4}, \quad (7.35)$$

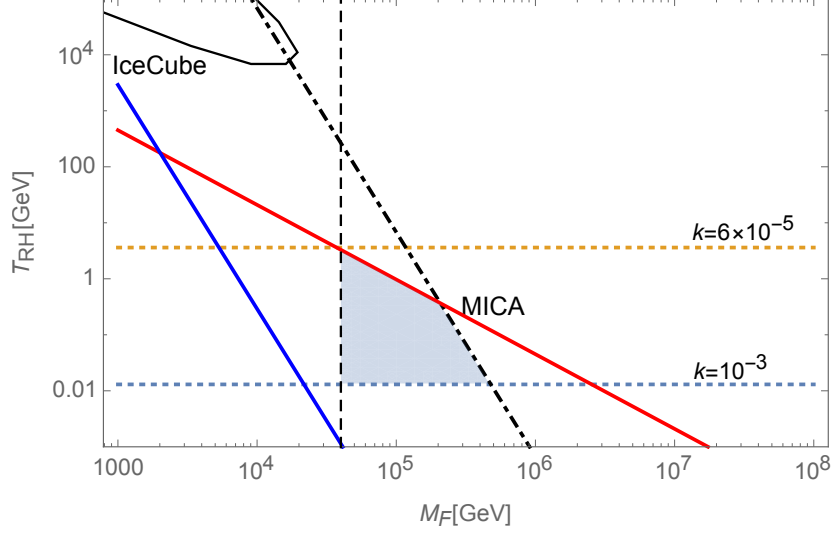


Figure 7.2: The allowed region for the gauge mediation type charged Q-ball as the dark matter (shaded region), where we adopted  $k = 10^{-3}$ . The red line shows the upper bound Eq. (7.30), the dotted lines denote the lower bound Eq. (7.35) for each value of  $k$  shown, the dashed line corresponds to the  $\Lambda_m$ -limit Eq. (7.39) with  $g = 1$ , the dashed-dotted line is the upper bound Eq. (7.43). The blue line is the lower bound Eq. (7.45). The IceCube constraint is also presented at the upper left [43].

which indeed corresponds to the horizontal dotted lines in Fig. 7.2. We adopted  $k = 10^{-3}$  as for identifying the allowed region. For  $k \lesssim 6 \times 10^{-5}$ , there is no allowed region for gauge mediation type Q-ball, so we must consider the case of gravity mediation domination, that is, the case of New-type Q-ball, where the horizontal lines will become upper bounds. We will discuss the case of New-type Q-ball in the next subsection.

It is known that the Higgs boson mass at around 126 GeV leads to [51, 52]

$$\Lambda_m \equiv \frac{kF}{M_m} \gtrsim 5 \times 10^5 \text{ GeV}. \quad (7.36)$$

Since the SUSY breaking scale is usually assumed to be small compared to the messenger mass

$$kF < M_m^2, \quad (7.37)$$

Eq. (7.36) becomes

$$\sqrt{kF} \gtrsim 5 \times 10^5 \text{ GeV}. \quad (7.38)$$

Then, using Eq. (4.34), it reduces to

$$M_F \gtrsim 4 \times 10^4 g^{1/2} \text{ GeV}, \quad (7.39)$$

which corresponds to the vertical dashed line in Fig. 7.2.

The stability against baryonic decay leads to

$$bm_p > \frac{dE}{dQ} \quad (7.40)$$

$$\begin{aligned} &\simeq \omega_0 \\ &\simeq \sqrt{2\pi}\zeta M_F Q^{-1/4}, \end{aligned} \quad (7.41)$$

which gives

$$Q \gtrsim \left( \frac{\sqrt{2\pi}\zeta M_F}{bm_p} \right)^4 \simeq 3.7 \times 10^{30} \left( \frac{\zeta}{2.5} \right)^4 \left( \frac{b}{1/3} \right)^{-4} \left( \frac{M_F}{10^6 \text{ GeV}} \right)^4. \quad (7.42)$$

Then, using Eq. (5.71) and Eq. (7.32), we obtain

$$T_{\text{RH}} \lesssim 7.5 \times 10^{-5} \text{ GeV} \left( \frac{\zeta}{2.5} \right)^{-3} \left( \frac{\beta}{6 \times 10^{-5}} \right)^{3/4} \left( \frac{b}{1/3} \right)^2 \left( \frac{M_F}{10^6 \text{ GeV}} \right)^{-4}, \quad (7.43)$$

which corresponds to the dashed-dotted line in Fig. 7.2.

Finally, since we are focusing on small Q-balls, especially compared to the Compton radius, our scenario is valid for

$$Q \lesssim \left( \frac{4\sqrt{2\pi}\zeta M_F}{m_e} \right)^4 \simeq 2.5 \times 10^{39} \left( \frac{\zeta}{2.5} \right)^4 \left( \frac{M_F}{10^6 \text{ GeV}} \right)^4, \quad (7.44)$$

which becomes

$$T_{\text{RH}} \gtrsim 2.9 \times 10^{-9} \text{ GeV} \left( \frac{\zeta}{2.5} \right)^{-3} \left( \frac{\beta}{6 \times 10^{-5}} \right)^{3/4} \left( \frac{M_F}{10^6 \text{ GeV}} \right)^{-4}, \quad (7.45)$$

where we used, again, Eqs. (5.71) and (7.32). This corresponds to the blue line in Fig. 7.2.

The observational constraint from IceCube, which probes the KKST process, is also presented at the upper left for comparison. We see that the MICA constraint is more stringent than that from IceCube, which leads to the smaller allowed region.

## New-type Q-balls

The Q-balls that are formed when the gravity mediation dominates are called the New-type Q-balls (see Sec. 5.1.3). Since their properties differ from those of gauge mediation type Q-balls, the MICA constraint on the Q-ball mass Eq. (7.30) applies to the model parameters in a different way: Here the typical charge of the Q-ball is given by Eq. (5.65) with  $m_\phi \rightarrow m_{3/2}$ , and the present abundance becomes

$$\frac{\rho_Q}{s} \sim \frac{3T_{\text{RH}}}{4} \frac{M_Q n_\phi / Q}{3H_{\text{osc}}^2 M_{\text{P}}^2} \sim \frac{9}{4} T_{\text{RH}} \frac{\phi_{\text{osc}}^2}{M_{\text{P}}^2}, \quad (7.46)$$

where  $n_\phi = m_{\text{eff}} \phi_{\text{osc}}^2$ ,  $3H_{\text{osc}} \simeq m_{\text{eff}}$ ,  $m_{\text{eff}} \simeq m_{3/2}$ , and we used Eq. (5.35) with  $m_\phi \rightarrow m_{3/2}$ . This explains the DM abundance for

$$\phi_{\text{osc}} \simeq 4.75 \times 10^{13} \text{ GeV} \left( \frac{T_{\text{RH}}}{\text{GeV}} \right)^{-1/2}. \quad (7.47)$$

Then, the MICA constraint Eq. (7.30) is translated as

$$T_{\text{RH}} \lesssim 5.79 \times 10^0 \left( \frac{m_{3/2}}{\text{GeV}} \right)^{-1} \text{ GeV}, \quad (7.48)$$

also using Eq. (5.65) with  $m_\phi \rightarrow m_{3/2}$ . This can be seen in the  $m_{3/2}$ - $T_{\text{RH}}$  plane, which we illustrate in Fig. 7.3. Here, again,  $T_{\text{RH}}$  is plotted for  $T_{\text{RH}} > \text{MeV}$ , which is the BBN constraint. The MICA constraint Eq. (7.48) is denoted by the magenta solid line in the figure. The allowed region is also determined by the additional conditions that also apply to the global Q-ball DM scenario:

The horizontal dotted lines indicate the condition that the gravity mediation effect dominates the potential of the Q-ball, which is given by

$$\phi_{\text{osc}} > \phi_{\text{eq}} \sim \sqrt{2} M_F^2 / m_{3/2}. \quad (7.49)$$

This reduces to

$$T_{\text{RH}} \lesssim 1.63 \times 10^{-6} \text{ GeV} g^{-2} k^{-2}, \quad (7.50)$$

using Eq. (7.47). In Fig. 7.3, the upper bounds on  $T_{\text{RH}}$  for  $k = 6 \times 10^{-5}$  and  $10^{-3}$  are shown.

Another condition on gravitino mass (SUSY breaking scale) comes from Eq. (7.36), the constraint from the Higgs mass, which reduces to

$$m_{3/2} \gtrsim 6.1 \times 10^{-8} k^{-1} \text{ GeV}, \quad (7.51)$$

using  $m_{3/2} \sim F/M_{\text{pl}}$ . This corresponds to the vertical dashed line in Fig. 7.3.



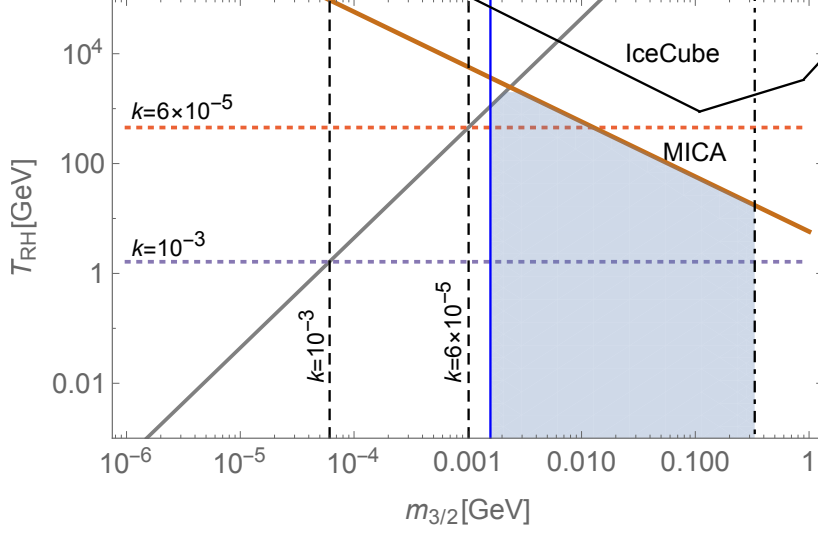


Figure 7.3: The allowed region for the new-type charged Q-ball as the dark matter (shaded region). The thick line shows the upper bound Eq. (7.48), the dotted lines denote the lower bound Eq. (7.50) for each value of  $k$  shown, the dashed line corresponds to the  $\Lambda_m$ -limit Eq. (7.51) with  $g = 1$ , for each value of  $k$  shown, the dashed-dotted line is the upper bound Eq. (7.52), and the blue line represents the lower bound Eq. (7.54). The IceCube constraint is also represented at the upper right [43].

The dashed-dotted line in Fig. 7.3 indicates following stability condition:

$$bm_p > \frac{dE}{dQ} \quad (7.52)$$

$$\simeq m_{3/2}, \quad (7.53)$$

which corresponds to the dashed-dotted line in Fig. 7.3, where we set  $b = 1/3$  for example.

Finally, the condition that the Q-balls are smaller than the Compton radius becomes

$$R_Q \sim |K|^{-1/2} m_{3/2}^{-1} < m_e^{-1}, \quad (7.54)$$

which is presented by the blue line in the figure, where we set  $K = -0.1$ .

The IceCube constraint is shown for comparison, and we see that more stringent MICA constraint makes the allowed region smaller.

## 7.3 Charged Q-ball decay rates into fermions

In the previous section, we considered charged Q-ball DM scenario, where we implicitly assumed the fast decay of the leptonic component. In order to gain some insight on this matter, we derive the decay rate of one scalar charged Q-ball into fermions [12], which is also from theoretical curiosity, since this is the first attempt to study the decay rate of the electrically charged Q-ball into other particles.

The Q-ball decay into other particles was first studied by Cohen *et al.* [53], who considered the Yukawa theory and calculated the neutrino pair production rate by leading semi-classical approximation treating the Q-ball as the classical background scalar field, where the Q-ball configuration was approximated as a step function. More realistic configurations are considered in Refs. [42, 54]. In particular, the production rates of quarks and gravitinos from the Q-balls in supersymmetric theories were derived in Ref. [42], which can be used to estimate baryon-to-dark matter ratio in gauge mediated SUSY breaking models, where the gravitino is dark matter.

Here we derive the decay rate of the charged Q-ball into fermions, using the leading semi-classical approximation in Ref. [53]. We assume that the scalar field in the Q-ball couples to fermions by Yukawa interaction. The decay rate into particles with the electric charge of the same sign is expected to be enhanced, compared to the case of a global Q-ball, which we will show is indeed the case. We also show that, on the other hand, the decay rate of the charged Q-ball is bounded from above, due to the Pauli blocking at the surface of the Q-ball, just as pointed out in the case of the global Q-ball [53], and even more suppressed due to the Coulomb potential outside the Q-ball, since it plays the role of a potential barrier for the fermions coming from the inside, as we will see later.

### 7.3.1 Setup and method

We consider the following Lagrangian,

$$\mathcal{L}_{\text{fermion}} = \chi^\dagger i\bar{\sigma}^\mu (\partial_\mu + iq_\chi e A_\mu) \chi + \eta^\dagger i\bar{\sigma}^\mu (\partial_\mu + iq_\eta e A_\mu) \eta - (g\phi^* \chi \eta + \text{h.c.}), \quad (7.55)$$

where  $\chi, \eta$  denote Weyl fermions, which couple to  $\phi$  through the Yukawa interaction, and  $\bar{\sigma}^\mu = (\mathbf{1}, -\sigma^i)$ , where  $\sigma^i$  are the Pauli matrices. We note that  $q_\chi + q_\eta = 1$  must be satisfied due to the charge conservation. Here we consider the simple case  $(q_\chi, q_\eta) = (1, 0)$ , which assigns the same sign of charge to  $\chi$ .

Then, the equations of motion are given as

$$i\bar{\sigma}^\mu (\partial_\mu + iq_\chi e A_\mu) \chi - g\phi \eta^\dagger = 0, \quad (7.56)$$

$$i\sigma^\mu (\partial_\mu - iq_\eta e A_\mu) \eta^\dagger - g\phi^* \chi = 0. \quad (7.57)$$

Since the Q-ball profile  $\phi = \phi(r)e^{i\omega t}$  is time dependent, the following modes mix with each other.

$$\chi \propto e^{-ik_+t}, \quad (7.58)$$

$$\eta^\dagger \propto e^{i(\omega-k_+)t} \equiv e^{ik_-t}. \quad (7.59)$$

If we define the fourier modes in time as  $\tilde{\chi} = \tilde{\chi}(k, \mathbf{x})$ ,  $\tilde{\eta} = \tilde{\eta}(k, \mathbf{x})$ , then, the equations of motion become

$$(k_+ + iq_\chi eA_0 - i\boldsymbol{\sigma} \cdot \nabla)\tilde{\chi} - g\phi(r)\tilde{\eta}^\dagger = 0, \quad (7.60)$$

$$(-k_- - iq_\eta eA_0 + i\boldsymbol{\sigma} \cdot \nabla)\tilde{\eta}^\dagger - g\phi(r)\tilde{\chi} = 0. \quad (7.61)$$

First, let us consider the case where  $\chi, \eta$  are free fields, whose equations of motion are

$$(k_+ - i\boldsymbol{\sigma} \cdot \nabla)\tilde{\chi} = 0, \quad (7.62)$$

$$(-k_- + i\boldsymbol{\sigma} \cdot \nabla)\tilde{\eta}^\dagger = 0. \quad (7.63)$$

Then, we can expand  $\chi, \eta^\dagger$  as follows:

$$\begin{aligned} \chi = \sum_{j,m} \int_0^\infty dk_+ & \left[ a_{\text{in}}(k_+, j, m) e^{-ik_+t} u^{(1)}(-k_+, j, m; \mathbf{x}) \right. \\ & \left. + a_{\text{out}}(k_+, j, m) e^{-ik_+t} u^{(2)}(-k_+, j, m; \mathbf{x}) + \text{terms for antiparticle} \right], \end{aligned} \quad (7.64)$$

$$\begin{aligned} \eta^\dagger = \sum_{j,m} \int_0^\infty dk_- & \left[ (-1)^{m-} c_{\text{in}}^\dagger(k_-, j, -m) e^{ik_-t} u^{(1)}(-k_-, j, m; \mathbf{x}) \right. \\ & \left. + (-1)^{m-} c_{\text{out}}^\dagger(k_-, j, -m) e^{ik_-t} u^{(2)}(-k_-, j, m; \mathbf{x}) + \text{terms for antiparticle} \right], \end{aligned} \quad (7.65)$$

using the solution of  $(k + i\boldsymbol{\sigma} \cdot \nabla)u^{(i)} = 0$ , which is given as

$$u^{(i)}(k, j, m; \mathbf{r}) \equiv \frac{k}{\sqrt{\pi}} \left[ h_{l'}^{(i)}(kr) \Phi(j, m, l') + i h_l^{(i)}(kr) \Phi(j, m, l) \right], \quad (i = 1, 2) \quad (7.66)$$

where  $(l, l') \equiv (j+1/2, j-1/2)$  and  $h_l^{(i)}$  is the Spherical Hankel functions.  $\Phi(j, m, l)$  and  $\Phi(j, m, l')$  are the Pauli spinors, which are given as

$$\Phi(j, m, l \equiv j + 1/2) \equiv \begin{pmatrix} \frac{\sqrt{j-m+1}}{\sqrt{2(j+1)}} Y_l^{m-1/2} \\ -\frac{\sqrt{j+m+1}}{\sqrt{2(j+1)}} Y_l^{m+1/2} \end{pmatrix}, \quad (7.67)$$

$$\Phi(j, m, l' \equiv j - 1/2) \equiv \begin{pmatrix} \frac{\sqrt{j+m}}{\sqrt{2j}} Y_{l'}^{m-1/2} \\ \frac{\sqrt{j-m}}{\sqrt{2j}} Y_{l'}^{m+1/2} \end{pmatrix}. \quad (7.68)$$

We also used  $\eta^\dagger = i\sigma_2(\eta_\alpha)^*$ ,  $i\sigma_2 u^{(1,2)}(k, j, m; \mathbf{x})^* = (-1)^{m+} u^{(2,1)}(k, j, -m; \mathbf{x})$ , where  $m_\pm \equiv m \pm 1/2$ .

It is naively expected that the fermions outside the charged Q-ball are described by the above solutions, but the Coulomb field  $A_0$ , which behaves as  $\sim 1/r$  outside the Q-ball, is not negligible compared to the fermion fields, which become spherical waves  $\sim e^{ikr}/r$  outside the Q-ball, coming from the asymptotic forms of the spherical Hankel functions. However, as we discuss in App. D,  $A_0$  gives only an additional phase factor  $e^{iq_{\chi,\eta} e^2 Q \log(2kr)}$  to the fermion spherical waves at infinity. Hence, the incoming and outgoing wave solutions are still valid, only corrected by the phase factors.

$a_{\text{out}}, c_{\text{out}}^\dagger$  are the superpositions of reflecting, and transmitting solutions:

$$a_{\text{out}}(k_+, j, m) = R_\chi(k_+, j) a_{\text{in}}(k_+, j, m) + T_\chi(k_+, j) (-1)^{m-} c_{\text{in}}^\dagger(k_-, j, -m), \quad (7.69)$$

$$(-1)^{m-} c_{\text{out}}^\dagger(k_-, j, -m) = T_\eta(k_-, j) a_{\text{in}}(k_+, j, m) + R_\eta(k_-, j) (-1)^{m-} c_{\text{in}}^\dagger(k_-, j, -m), \quad (7.70)$$

whose coefficients must satisfy

$$|T_\chi(k_+, j)|^2 = |T_\eta(k_-, j)|^2, \quad (7.71)$$

$$|R_\chi(k_+, j)|^2 + |T_\chi(k_+, j)|^2 = 1, \quad (7.72)$$

$$|R_\eta(k_-, j)|^2 + |T_\eta(k_-, j)|^2 = 1, \quad (7.73)$$

due to the anticommutation of the creation and annihilation operators.

If we define the vacuum  $|0_{\text{in}}\rangle$  by  $a_{\text{in}}|0_{\text{in}}\rangle = c_{\text{in}}|0_{\text{in}}\rangle = 0$  at infinity, the number of outgoing  $\chi$  becomes

$$\langle 0_{\text{in}} | a_{\text{out}}^\dagger(k_+, j, m) a_{\text{out}}(k'_+, j', m') | 0_{\text{in}} \rangle = |T_\chi(k_+, j)|^2 \delta(k_+ - k'_+) \delta_{j,j'} \delta_{m,m'}, \quad (7.74)$$

by using Eq. (7.69). Summing this over the states, the production rate  $dQ_i/dt$  is derived as

$$\frac{dQ_i}{dt} = \sum_{j=1/2} \int_0^\omega \frac{dk}{2\pi} (2j+1) |T_i(k, j)|^2, \quad (i = \chi, \eta) \quad (7.75)$$

where we averaged the particle number over the time, using  $\delta(0) = T/2\pi$ . This gives the decay rate of the charged Q-ball into the fermion species  $i$ . Note that  $\eta$  with momentum  $k_\eta$  will be produced by the same amount as  $\chi$  with momentum  $\omega - k_\eta$ , using Eq. (7.71), which is understood from the relation  $dE/dQ = \omega$  of the charged Q-balls.

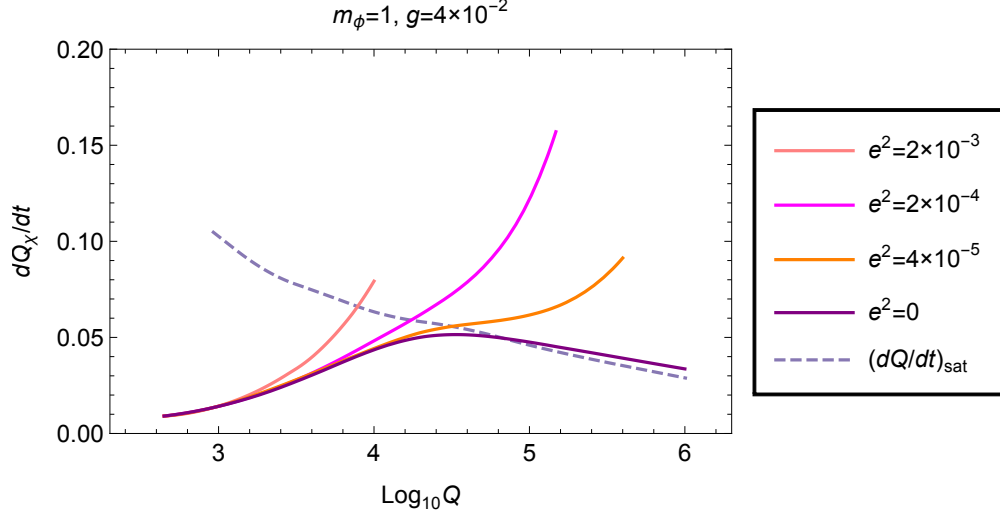


Figure 7.4: The production rates of fermions from charged Q-balls. We find the enhancement due to the electric repulsion. The dashed line denotes the saturated rates for global Q-balls. Note that for global Q-balls, the production rates saturate as the charge grows, while for charged Q-balls the saturation is not clear from the figure.

We can determine  $R_i, T_i$  by matching the solutions to the interior, where  $\phi, A_0 \neq 0$ . We can write the interior solutions as follows:

$$\tilde{\chi} = f_\chi(r)\Phi(j, m, l') + ig_\chi(r)\Phi(j, m, l), \quad (7.76)$$

$$\tilde{\eta}^\dagger = f_\eta(r)\Phi(j, m, l') + ig_\eta(r)\Phi(j, m, l), \quad (7.77)$$

where, again, we expanded the solutions by the Pauli spinors. We numerically solve for  $f_i, g_i$ , using Eq. (7.60) and (7.61), under the following boundary conditions.

$$f'_i(0) = g'_i(0) = 0, \quad (7.78)$$

which means the regularity of the solutions at the origin.

### 7.3.2 Results

In Fig. 7.4, we present the results for the production rates. Due to the electric charge of the Q-ball, the decay rate into particles with the charge of the same sign is expected to be enhanced by the repulsion, compared to the case of the global Q-ball with the same charge. We can confirm this point in the figure, where more fermions are produced for larger  $e^2$ .

On the other hand, since  $\chi$  is a fermion, the flux coming out of the surface of the Q-ball will be bounded from above by Pauli blocking. For global Q-balls, this bound is obtained by integrating the occupied phase space ( $0 < k_+ < \omega$ ) at the Q-ball surface [53]:

$$\left(\frac{dQ}{dt}\right)_{\text{sat}} \equiv \frac{\omega^3 R^2}{24\pi}, \quad (7.79)$$

which is called saturated rate. The gauge mediation type global Q-balls have the following properties (see Sec. 5.1.3):

$$\omega \propto Q^{-1/4}, \quad (7.80)$$

$$R \simeq \pi/\omega, \quad (7.81)$$

hence we see that the saturated rate has charge dependence of  $Q^{-1/4}$ , which is illustrated by a dashed line in the figure. The production rate saturates for large Yukawa coupling, or when  $g\phi_0/\omega \gg 1$ , where  $\phi_0$  is the maximal value of  $\phi$ . Thus, the large Q-ball gives large  $g\phi_0/\omega$ , which saturate the production rate.

In the case of charged Q-balls, however,  $\omega$  becomes large as the charge grows, as pointed out in the previous chapter, hence  $g\phi_0/\omega$  does not necessarily grow for a large charge. But if we consider a charged Q-ball with a given charge and large Yukawa coupling that gives  $g\phi_0/\omega \gg 1$ , we find that the production rate saturates, as we present in Fig. 7.5. We considered the charged Q-ball with large charge, in order to well-define the size of the Q-ball (see Fig. 6.3), so that we can compare the production rate to the saturated rate defined as

$$\left(\frac{dQ}{dt}\right)_{\text{sat}}^{(\text{charged})} \equiv \frac{\tilde{\omega}^3 R^2}{24\pi}, \quad (7.82)$$

where we replaced  $\omega$  in Eq. (7.79) by  $\tilde{\omega} \equiv \omega - e^2 Q/4\pi R$ , which is the maximal fermion momentum at the surface of Q-ball. However, we note that the saturated rate is rather larger than predicted by the classical formula. The reason is given as follows: Since the classically produced fermions are “accelerated” by the Coulomb potential outside the Q-ball ( $\sim 1/r$ ), their momentum at infinity becomes  $e^2 Q/4\pi R < k < \omega$ . However, the fermions with momentum of  $0 < k < e^2 Q/4\pi R$  are also produced (see Fig. 7.6), which gives the discrepancy in Fig. 7.5.

This production of forbidden momentum can be understood as a tunneling effect. For large Yukawa coupling, the fermions mainly feel  $\phi$  inside the Q-ball, which we confirmed numerically as well, and feel the Coulomb potential suddenly at  $r = R$ . This phenomenon is similar to that the saturated fermions with  $0 < k < e^2 Q/4\pi R$  that are mainly produced by  $\phi$  bump into the potential barrier at  $r = R + \Delta R$  ( $\Delta R \ll R$ ), whose similarity is again numerically confirmed. This

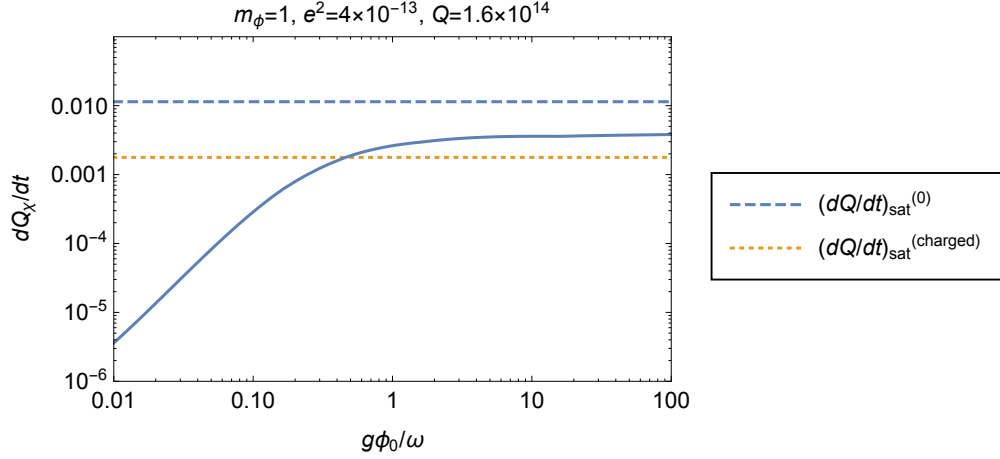


Figure 7.5: The production rate from a charged Q-ball as a function of  $g\phi_0/\omega$ . we see that the production rate saturates for  $g\phi_0/\omega \gg 1$ . We considered a charged Q-ball with large charge, which well-defines the Q-ball size as mentioned in the previous chapter, so that we can easily compare the production rate to the classical saturated rate, which is illustrated by a dotted line. We find that the saturated rate is larger than the classical formula, since the fermions with classically forbidden momenta are produced at infinity through the quantum tunneling, where the Coulomb potential outside the Q-ball plays the role of the potential barrier for fermions coming from inside. We can find that the production rate is indeed suppressed compared to the saturated rate without the Coulomb barrier outside.

implies that the fermions with  $0 < k < e^2 Q/4\pi R$  are produced by the tunneling effect, which, in particular, must be suppressed than the following saturated rate:

$$\left(\frac{dQ}{dt}\right)_{\text{sat}}^{(0)} \equiv \frac{\omega^3 R^2}{24\pi}, \quad (7.83)$$

which is without the Coulomb barrier outside the Q-ball. This can be verified in Fig. 7.5 as well. Hence, we are led to conclude that the decay rate of the charged Q-ball is upperly bounded by the Pauli blocking at the surface, and furtherly suppressed by the Coulomb potential outside, which plays the role of an effective potential barrier for the fermion flux coming from the inside.

Finally, we illustrate the production rates when  $g\phi_0/\omega \ll 1$  in Fig. 7.7. We consider the charged Q-balls of small Coulomb potential  $e^2 Q/4\pi R \ll \omega$ , and normalize the production rates by the classical saturated rates  $(dQ/dt)_{\text{sat}}^{(\text{charged})}$ , given by Eq. (7.82). Since the values of the saturated rates are between  $(dQ/dt)_{\text{sat}}^{(\text{charged})}$  and  $(dQ/dt)_{\text{sat}}^{(0)}$ , the normalized rate is expected to saturate close to unity for  $e^2 Q/4\pi R \ll \omega$ , which can be verified in the figure. Even for such small Coulomb

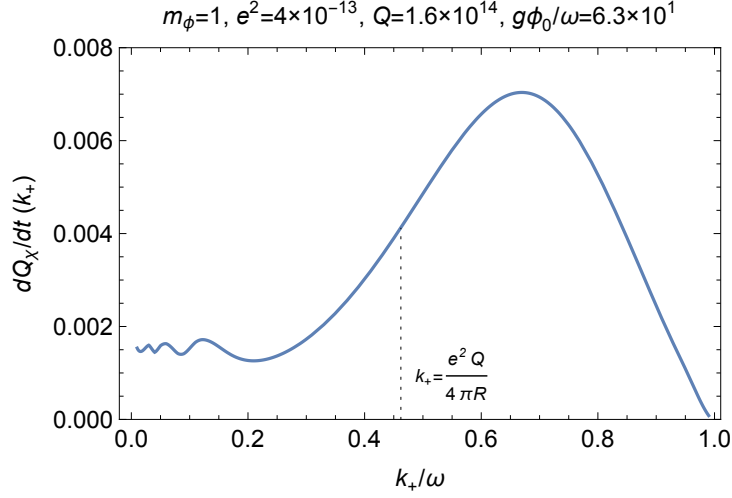


Figure 7.6: The production rate as a function of momentum normalized by  $\omega$ . One can see the production of the classically forbidden momenta.

potential, there exist differences in the production rates when  $g\phi_0/\omega \ll 1$ , depending on  $e^2$  and  $Q$ . One can see the normalized production rates are enhanced as  $e^2$  or  $Q$  grows. In the previous work on the global Q-ball decay rates [42], the authors pointed out that the normalized production rate is enhanced if  $\phi$  has a large value near the surface. The similar understanding may be possible for the charged Q-ball, since the electric repulsion deforms the profile and pushes the charge towards the surface of the Q-ball.

## 7.4 Brief summary

We considered a nearly equal number of charged Q-balls and anti-Q-balls with the charge of  $\alpha^{-1} \sim \mathcal{O}(100)$ , and discussed their evolution and the present relics, which we expect to behave as massive atomic objects, and detectable through electromagnetic processes. The MICA direct detection experiment gives the most stringent constraint on the flux of the relics, since the detection time is extremely long which is essentially the age of the mica. For gauge mediation type Q-balls, we translated the MICA constraint into that on the gauge mediation model parameter  $M_F$  and reheating temperature  $T_{\text{RH}}$ , which leads to the smaller allowed region. For New-type Q-balls, the MICA constraint reduces to that on the gravitino mass  $m_{3/2}$  and  $T_{\text{RH}}$ , where we also found the significant reduction of the allowed parameter region.

We implicitly assumed the fast decay of the leptonic component, so that the electrically charged Q-balls are formed in the early universe. In order to gain some



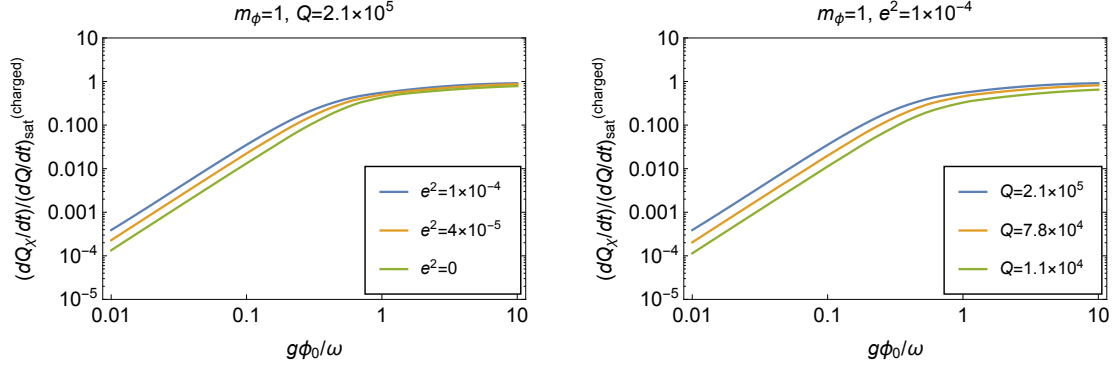


Figure 7.7: The production rates as a function of  $g\phi_0/\omega$ , normalized by the classical saturated rates. One can see the enhancement of the production rates when  $g\phi_0/\omega \ll 1$ , for large  $e^2$  or  $Q$ . This can be understood from the analogy to the global Q-ball case, where the production rate enhances if  $\phi$  has a large value near the surface, which coincides with our case since the electric repulsion deforms the profile of the charged Q-ball and the charge is pushed towards the surface.

insight on this matter, we derived the decay rate of one scalar charged Q-ball into fermions, using the semi-classical method in Ref. [53]. The decay rate into particles with the charge of the same sign is expected to be enhanced, compared to the case of the global Q-ball. We found that indeed more particles come out from the surface of the charged Q-ball, compared to the case of the global Q-ball, due to the electric repulsion. We found that the production rates from each charged Q-ball also saturate when the Yukawa interaction becomes strong, just as in the case of the global Q-ball. However, the saturated rate is somewhat larger than the one predicted by the classical formula, which is obtained by integrating the fully occupied phase space ( $0 < k_+ < \omega - e^2 Q/4\pi R$ ), at the surface of the Q-ball. The disagreement arises since the fermions with classically forbidden momenta are produced by the quantum effect. We found that the production can be interpreted as a tunneling effect, where the fermions, which are mainly produced by  $\phi$  due to the strong Yukawa interaction, come out as a saturated flux, and immediately bump into the Coulomb barrier and tunnel through it. The production must be suppressed compared to the saturated rate when the Coulomb barrier outside does not exist, which is also confirmed.

We also found the enhancement of the normalized production rates for  $g\phi_0/\omega \ll 1$  when  $e^2$  or  $Q$  becomes large, which can be explained by the analogy to the case of the global Q-ball, where the normalized production rate enhances if  $\phi$  has a large value near the surface, since the electric repulsion deforms the profile of the charged Q-ball and pushes the charge outward.

We comment on the decay of the leptonic component in the charged Q-ball

DM scenario. The Q-balls in the cosmological context, are usually very large, with the charge of  $10^{20}$  to  $10^{30}$ . Thus, it is likely that  $g\phi_0/\omega \gg 1$  unless the Yukawa coupling  $g$  is extremely small, which means that the production rates of leptons are saturated. We also note that the electric charge of the Q-ball can grow only until  $Q \sim \mathcal{O}(100)$  mainly due to the Schwinger effect, which leads to nearly the same size and the maximal momentum of the outgoing particle as in the case of the global Q-ball. Hence, the saturated rate hardly changes from that for the global Q-ball, which is typically of GeV order, thus we conclude that the decay is sufficiently fast, and our assumption was reasonable.

# Chapter 8

## I-balls

The second issue of this thesis is the inflaton fragmentation into localized solitons, which are called I-balls. In this chapter, we review some basic properties of I-balls. It is known that in a periodic dynamics, such as coherent oscillation, there is a conserved quantity called adiabatic invariant  $I$ . The I-ball is defined as the lowest energy real scalar configuration under the conservation of the adiabatic invariant. In the following sections, we derive the I-ball solution by minimizing the energy with fixed  $I$ . Even if we can obtain the equation for I-ball solution, certain conditions must be satisfied in order for the localized solution to exist, which become those on the potential of the scalar field, just as in the case of Q-ball (see Sec. 5.1). We discuss the existence conditions of the I-ball solution.

### 8.1 I-ball solution and its existence conditions

We consider a real scalar theory with the following potential.

$$V = \frac{1}{2}m^2\phi^2 + \delta V, \quad (8.1)$$

where  $\delta V$  denotes the small deviation from quadratic potential. Then,  $\phi$  is approximately given by the following form,

$$\phi(\mathbf{x}, t) \simeq \Phi(\mathbf{x}) \cos mt, \quad (8.2)$$

due to the domination of quadratic term. In the periodic dynamics, the area surrounded by the one-period trajectory in the phase space is constant, which is given as follows:

$$I \equiv \oint \pi_i d\phi_i \sim \frac{1}{m} \overline{\dot{\phi}_i^2} \quad (8.3)$$

$$= \frac{1}{m} \int d^3x \overline{\dot{\phi}^2}, \quad (8.4)$$

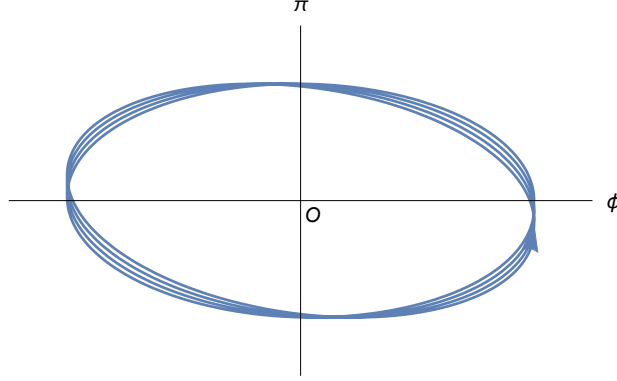


Figure 8.1: Illustration of adiabatic deviation from periodicity.

where  $\pi(= \dot{\phi})$  and bar represent the canonical momentum of  $\phi$  and the time-average over a period, respectively, and we temporarily have written the spatial integral as the summation of the degree of freedom. This quantity is known to be conserved for adiabatic deviation from the periodicity (Fig. 8.1), which is called adiabatic invariant.

We can find the I-ball solution by minimizing the energy with a fixed  $I$ . Using Lagrange multiplier method, we minimize the following quantity:

$$\overline{E_{\tilde{\omega}}} \equiv \overline{E} + \tilde{\omega} \left[ I - \frac{1}{m} \int d^3x \overline{\dot{\phi}^2} \right] \quad (8.5)$$

$$= \int d^3x \left[ \frac{1}{2} \left( 1 - 2\frac{\tilde{\omega}}{m} \right) \overline{\dot{\phi}^2} + \frac{1}{2} \overline{(\nabla\phi)^2} + \overline{V} \right] + \tilde{\omega} I \quad (8.6)$$

$$\simeq \frac{1}{4} \int d^3x \left[ (\nabla\Phi)^2 + m^2 \left( \left( 1 - 2\frac{\tilde{\omega}}{m} \right) \Phi^2 + 4\overline{V}(\Phi) \right) \right] + \tilde{\omega} I, \quad (8.7)$$

where we used the following averaged quantities.

$$\overline{\dot{\phi}^2} \simeq \frac{1}{2} m^2 \Phi^2, \quad (8.8)$$

$$\overline{\phi^n} \simeq c_n \Phi^n, \quad (8.9)$$

with  $(c_2, c_4, c_6, \dots) = (1/2, 3/8, 5/16, \dots)$ . Then, the minimization gives the equation for  $\Phi$ :

$$\Delta\Phi - m^2 \left( 1 - 2\frac{\tilde{\omega}}{m} \right) \Phi - 2\frac{d\overline{V}(\Phi)}{d\Phi} = 0. \quad (8.10)$$

Since we are seeking for the spherical solution, this equation reduces to

$$\frac{d^2}{dr^2}\Phi + \frac{2}{r} \frac{d}{dr}\Phi + \frac{dV_{\Phi}}{d\Phi} = 0, \quad (8.11)$$

where we defined the effective potential for  $\Phi$  as

$$V_\Phi \equiv -2\bar{V}(\Phi) - \frac{m^2}{2} \left(1 - 2\frac{\tilde{\omega}}{m}\right) \Phi^2. \quad (8.12)$$

The condition of spatial localization gives the following boundary conditions:

$$\frac{d}{dr}\Phi(r=0) = 0, \quad \Phi(r=\infty) = 0. \quad (8.13)$$

Then, just as in the case of Q-ball, the analogy with the classical dynamics of point mass will be useful for examining the existence of the solution, where we treat  $r$  as a time variable:

$$r \rightarrow t. \quad (8.14)$$

Then, Eq. (8.11) becomes

$$\ddot{\Phi} + \frac{2}{t}\dot{\Phi} + \frac{dV_\Phi}{d\Phi} = 0, \quad (8.15)$$

which is equivalent to the equation of motion of a classical point mass under the potential  $V_\Phi$  and the friction proportional to the velocity. Eq. (8.13) describes that the point mass is initially at rest and asymptotes to the origin. This constrains the potential  $V_\Phi$  in shape, which is given by the following conditions:

$$\max[V_\Phi] > 0, \quad (8.16)$$

$$V_\Phi''(0) < 0, \quad (8.17)$$

where the first condition gives the sufficient energy to reach the origin, while the second gives the stopping force at the origin. The effective potential can be rewritten as the quadratic term plus higher-order correction:

$$V_\Phi = -m^2 \left(1 - \frac{\tilde{\omega}}{m}\right) \Phi^2 - 2\bar{\delta V}(\Phi), \quad (8.18)$$

which gives

$$V_\Phi''(0) = -2m^2 \left(1 - \frac{\tilde{\omega}}{m}\right). \quad (8.19)$$

Therefore, the second condition Eq. (8.16) can be satisfied for a suitable choice of Lagrange multiplier  $\tilde{\omega}$ . Then, however, the first condition gives a constraint on  $\bar{\delta V}$  as

$$\bar{\delta V} < 0, \quad (8.20)$$

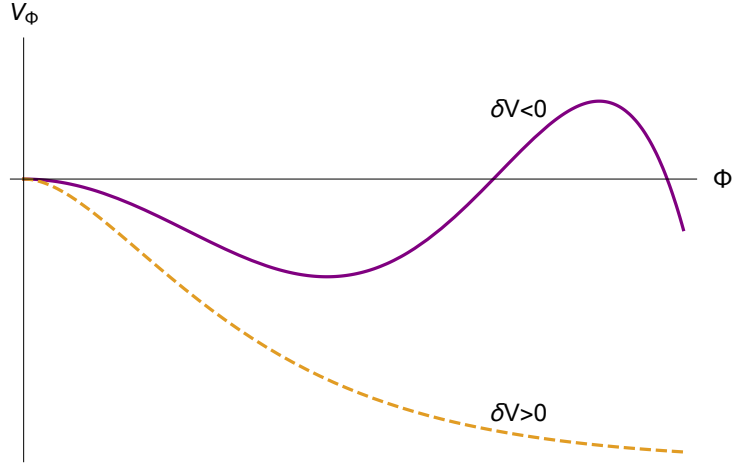


Figure 8.2: The illustration of the existence condition of the I-ball solution. The potential shallower than quadratic ( $\delta V < 0$ ) is required.

since otherwise the potential  $V_\Phi$  will be negative for every  $\Phi$ , which does not satisfy Eq. (8.16). This is the existence condition of the I-ball solution, which coincides with the heuristically known condition that the potential must be shallower than quadratic for the formation of the I-balls [55]. We illustrate this condition on the potential shape in Fig. 8.2.

## Chapter 9

# I-ball formation in E-models of $\alpha$ -attractors

Recent observations of cosmic background radiation (CMB) [13] have excluded the various class of models, including single power-law potential models, through the combined constraints on the spectral index  $n_s$  and the tensor-to-scalar ratio  $r$ .

A new class of inflationary models that is consistent with the observations, was recently proposed [14, 15, 16]. These models, called  $\alpha$ -attractors, are categorized into two subclasses: T-models and E-models, which are characterized by the following potentials,

$$V_T(\phi) = V_0 \tanh^{2n} \left( \frac{\phi}{\sqrt{6\alpha} M_{\text{pl}}} \right), \quad (9.1)$$

$$V_E(\phi) = V_0 \left( 1 - e^{-\sqrt{\frac{2}{3\alpha}} \frac{\phi}{M_{\text{pl}}}} \right)^{2n}, \quad (9.2)$$

respectively. Since the potential is shallower than quadratic,  $\phi$  is expected to fragment into I-balls, as pointed out in the previous chapter. It was reported that the I-balls are formed in the case of T-models, for  $n = 1$ ,  $\alpha \lesssim \alpha_{\text{th}}^T \sim 10^{-4}$  [25, 26]. This is because the negative higher-order (than quartic) terms induce the negative pressure on the inflaton. In the case of E-models, however, the existence of the cubic term is crucial which makes the potential asymmetric and flatter than quadratic only for  $\phi > 0$ , which may lead to a different phenomenon from the T-models. The I-ball formation in the Starobinsky model was studied in Ref. [56], which corresponds to the case  $(n, \alpha) = (1, 1)$  of the E-models. The authors concluded that while lumps are formed in Minkowski space, if one considers the cosmic expansion, inflaton damps quickly so that the negative pressure is inefficient and the fluctuation cannot grow non-linear. However, if we consider a smaller  $\alpha$ , the negative pressure can be efficient longer, and the instability can

grow non-linear to form the I-balls [27]. We treat  $\phi$  in linear approximation and examine whether the fluctuation grows for small  $\alpha$ . In order to follow the non-linear dynamics, we also performed the lattice simulations in 1D, 2D, 3D.

## 9.1 Model

The great consistency of  $\alpha$ -attractors with the observations comes from the flatness of the potential in the large field regime  $\phi/\sqrt{\alpha} \gg 1$ . This flatness originates from the pole in the kinetic term e.g.,

$$\mathcal{L} \supset -\frac{3\alpha(\partial\tau)^2}{4\tau^2} - V(\tau), \quad (9.3)$$

where  $\tau$  denotes a real scalar field. Once we use the canonically normalized field  $\phi$ , which is related to  $\tau$  as  $\tau = -\exp(\sqrt{\frac{2}{3\alpha}}\frac{\phi}{M_{\text{pl}}})$ , the potential in the large field regime is exponentially stretched and becomes sufficiently flat for the inflation.

The  $\alpha$ -attractors are currently categorized into two subclasses: T-models and E-models. The E-models are characterized by the following asymmetric potential [57, 58],

$$V_{\text{E}}(\phi) = \frac{3}{4}m^2M_{\text{pl}}^2\alpha \left(1 - e^{-\sqrt{\frac{2}{3\alpha}}\frac{\phi}{M_{\text{pl}}}}\right)^{2n}, \quad (9.4)$$

which becomes asymptotically flat for  $\phi \gtrsim \sqrt{\alpha}M_{\text{pl}}$ . Note that it reduces to the shape of the Starobinsky potential for  $(n, \alpha) = (1, 1)$ . In Fig. 9.1, we illustrate the potential for different  $\alpha$  with  $n = 1$ , which is the case we will consider in the following.

We discuss the Inflationary observables predicted by the  $\alpha$ -attractors. The power spectrum and the spectral index of primordial perturbation are given as follows:

$$\mathcal{P}_\zeta \equiv \frac{V}{24\pi^2\epsilon M_{\text{pl}}^4} \simeq \frac{N^2 m^2}{24\pi^2 M_{\text{pl}}^2}, \quad (9.5)$$

$$n_s \equiv 1 - 6\epsilon + 2\eta \simeq 1 - \frac{2}{N}, \quad (9.6)$$

$$r \equiv 16\epsilon \simeq \frac{12\alpha}{N^2}, \quad (9.7)$$

where we assumed  $N \gg 1, \alpha$ . Here we used the following relation for the  $e$ -folds  $N$  to  $\phi$ :

$$N = -\int_{t_{\text{end}}}^{t(\phi)} dt H \simeq \frac{3}{4}\alpha e^{\sqrt{\frac{2}{3\alpha}}\frac{\phi}{M_{\text{pl}}}}. \quad (9.8)$$



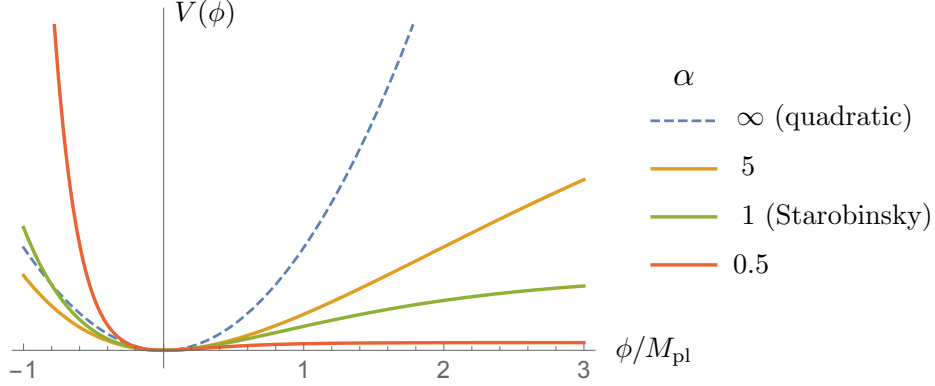


Figure 9.1: E-model potentials ( $n = 1$ ) for different  $\alpha$ . Note that  $\alpha = 1$  corresponds to the Starobinsky model.

The latest Planck results [13] gives the power spectrum of the curvature perturbation at the CMB scale  $k_* \simeq 0.002 \text{ Mpc}^{-1}$  as

$$\mathcal{P}_\zeta(k_*) \simeq 2.4 \times 10^{-9}, \quad (9.9)$$

which leads to

$$m \simeq 1.4 \times 10^{-5} M_{\text{pl}} \left( \frac{N_*}{55} \right)^{-1}. \quad (9.10)$$

The spectral index and the tensor-to-scalar ratio are also constrained as

$$n_s = 0.968 \pm 0.006, \quad r < 0.11 \quad (\text{Planck 2015}), \quad (9.11)$$

which are in a good agreement with the predictions from the E-models of  $\alpha$ -attractors:

$$n_s \simeq 0.964, \quad r = 4\alpha \times 10^{-3}, \quad (N_* = 55) \quad (9.12)$$

for  $\alpha \lesssim \mathcal{O}(10)$ . In Fig. 9.2, we present the predictions from the E-models for several  $\alpha$  in the  $(n_s, r)$  plane.

It is worth to mention the predictions from the T-models. Since the potential for the large field is similar to the E-models, their predictions on the primordial perturbation coincide for  $\alpha \ll N$ , which means that the two models nearly degenerate in the  $(n_s, r)$  plane. The coherent oscillation after inflation is driven by different potential, and in particular, the condition for the fragmentation in E-models differs from that in T-models, as we will see later.

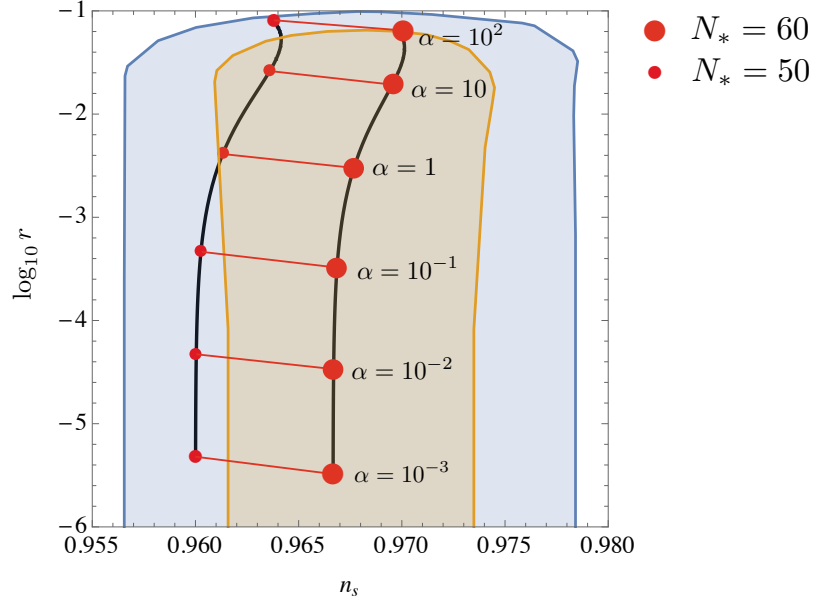


Figure 9.2: The predictions from the E-models ( $n = 1$ ) for several  $\alpha$ . Note that  $\alpha = 1$  corresponds to the Starobinsky model.

Finally, we give the inflaton field at the end of the inflation  $\phi_{\text{end}}$ , which will be used in the following sections. The inflation end is defined by the condition  $\epsilon, |\eta| \sim 1$ . Then the field value of the inflaton is given as

$$\phi_{\text{end}} \simeq \sqrt{\frac{3\alpha}{2}} M_{\text{Pl}} \log \left[ \sqrt{\frac{4}{3\alpha}} + 1 \right]. \quad (9.13)$$

We set  $\phi_{\text{end}}$  as the initial condition of the coherent oscillation after inflation. In the strict sense, the oscillation amplitude is larger than  $\phi_{\text{end}}$ , due to the non-zero velocity:  $\dot{\phi}_{\text{end}} \neq 0$ . However, inflaton damps to  $\phi_{\text{end}}$  by the expansion in a short time scale compared to that of the fragmentation of  $\phi$ :  $\mathcal{O}(100)m^{-1}$ , as we will find in the following. Since the fragmentation will be more efficient for a larger amplitude, our choice will be a rather conservative one.

## 9.2 I-ball solution and its profile

As we mentioned in the previous chapter, I-ball are defined as the solutions which minimize the one-period averaged energy, with a fixed adiabatic invariant  $I$ . In the

E-models, while the dynamics is governed by harmonic oscillation, the asymmetric correction by the cubic term plays an important role in the I-ball formation, which may complicate the analysis on the energy. In this section, we derive the I-ball profile using an alternative method, called  $\epsilon$ -expansion [59, 60, 61], where one directly finds the solution in the small-amplitude approximation. The analytic solutions exist only for 1+1 dimension, which we will adopt in the following.

The equation of motion is given as follows:

$$\frac{d^2\phi}{dt^2} - \frac{d^2\phi}{dx^2} + V'(\phi) = 0, \quad (9.14)$$

with

$$V'(\phi) = \sqrt{\frac{3\alpha}{2}} m^2 M_{\text{pl}} e^{-\sqrt{\frac{2}{3\alpha}} \frac{\phi}{M_{\text{pl}}}} \left( 1 - e^{-\sqrt{\frac{2}{3\alpha}} \frac{\phi}{M_{\text{pl}}}} \right). \quad (9.15)$$

Assuming the small  $\phi/\sqrt{\alpha}M_{\text{pl}}$ , we define the parameter  $\epsilon$  as

$$\epsilon \equiv \frac{\Phi}{\sqrt{\alpha}M_{\text{pl}}}, \quad (9.16)$$

where  $\Phi$  denotes the amplitude of the harmonic oscillation. We use the following rescaled variables,

$$\tau \equiv mt \sqrt{1 - A\epsilon - B\epsilon^2 + \mathcal{O}(\epsilon^3)}, \quad (9.17)$$

$$\chi \equiv mx (\epsilon + \mathcal{O}(\epsilon^2)), \quad (9.18)$$

and expand  $\phi$  as

$$\frac{\phi}{\sqrt{\alpha}M_{\text{pl}}} \equiv \epsilon\phi_1 + \epsilon^2\phi_2 + \epsilon^3\phi_3 + \mathcal{O}(\epsilon^4). \quad (9.19)$$

Then, Eq. (9.14) is decomposed as

$$\phi_{1\tau\tau} + \phi_1 = 0, \quad (9.20)$$

$$\phi_{2\tau\tau} + \phi_2 = A\phi_{1\tau\tau} + \frac{3}{\sqrt{6}}\phi_1^2, \quad (9.21)$$

$$\phi_{3\tau\tau} + \phi_3 = B\phi_{1\tau\tau} + \phi_{1\chi\chi} + A\phi_{2\tau\tau} + \sqrt{6}\phi_1\phi_2 - \frac{7}{9}\phi_1^3, \quad (9.22)$$

where we also expanded Eq. (9.15). If we use the solution of Eq. (9.20), which is given as

$$\phi_1(\chi, \tau) \equiv f(\chi) \cos(\tau), \quad (9.23)$$

Eqs. (9.21, 9.22) reduce to

$$\phi_{2\tau\tau} + \phi_2 = -Af \cos(\tau) + \frac{3}{\sqrt{6}} f^2 \cos^2(\tau), \quad (9.24)$$

$$\phi_{3\tau\tau} + \phi_3 = -Bf \cos(\tau) + f_{\chi\chi} \cos(\tau) + A\phi_{2\tau\tau} + \sqrt{6}f \cos(\tau)\phi_2 - \frac{7}{9}f^3 \cos^3(\tau). \quad (9.25)$$

Since we are seeking for the stable solution, we eliminate the secular term in Eq. (9.24) by  $A = 0$ , which gives  $\phi_2$  as follows:

$$\phi_2 = f^2 \left[ \frac{\sqrt{6}}{4} - \frac{\sqrt{6}}{12} \cos(2\tau) \right]. \quad (9.26)$$

Then, Eq. (9.25) reduces to

$$\phi_{3\tau\tau} + \phi_3 = \left[ f_{\chi\chi} - Bf + \frac{2}{3}f^3 \right] \cos(\tau) - \frac{4}{9}f^3 \cos(3\tau). \quad (9.27)$$

Here, again, the stability of the solution requires the first term to cancel:

$$f_{\chi\chi} - Bf + \frac{2}{3}f^3 = 0. \quad (9.28)$$

This gives the profile of the solution as follows:

$$f(\chi) = f(0) \operatorname{sech} \left[ \frac{1}{\sqrt{3}} f(0) \chi \right]. \quad (9.29)$$

If we also solve Eq. (9.27), the additional corrections are obtained, which leads to the following perturbative solution:

$$\begin{aligned} \phi \simeq \sqrt{\alpha} M_{\text{pl}} \left[ \frac{\sqrt{6}}{4} \left( \frac{\Phi}{\sqrt{\alpha} M_{\text{pl}}} \right)^2 + \frac{\Phi}{\sqrt{\alpha} M_{\text{pl}}} \cos(\tau) \right. \\ \left. - \frac{\sqrt{6}}{12} \left( \frac{\Phi}{\sqrt{\alpha} M_{\text{pl}}} \right)^2 \cos(2\tau) + \frac{1}{18} \left( \frac{\Phi}{\sqrt{\alpha} M_{\text{pl}}} \right)^3 \cos(3\tau) \right] + \mathcal{O}(\epsilon^4), \end{aligned} \quad (9.30)$$

where  $\Phi$  and  $\tau$  are

$$\Phi \equiv \Phi(0) \operatorname{sech} \left[ \frac{\Phi(0)}{\sqrt{3\alpha} M_{\text{pl}}} mx \right], \quad (9.31)$$

$$\tau = \sqrt{1 - \frac{1}{3} \left( \frac{\Phi}{\sqrt{\alpha} M_{\text{pl}}} \right)^2} mt. \quad (9.32)$$

Note that the asymmetric property appears as a second order correction. We compare these analytic profiles with those obtained by 1D lattice simulations in Sec. 9.4.

### 9.3 Linear instability analysis

The E-model potential is asymmetric due to the cubic term, which makes it flatter than quadratic for  $\phi > 0$ . This may induce the negative pressure on  $\phi$ , which leads to its fragmentation into the I-balls. In this section, we perform the linear instability analysis and examine the growth of the fluctuation for small  $\alpha$ .

First, we divide  $\phi$  into the background  $\phi_0(t)$  and the linear fluctuation  $\delta\phi(\mathbf{x}, t)$ . Then, the following equation of motion for  $\phi$

$$\ddot{\phi} + 3H\dot{\phi} - \frac{1}{a^2}\Delta\phi + V'(\phi) = 0, \quad (9.33)$$

is decomposed into

$$\ddot{\phi}_0 + 3H\dot{\phi}_0 + V'(\phi_0) = 0, \quad (9.34)$$

$$\delta\ddot{\phi}_k + 3H\delta\dot{\phi}_k + \left[\frac{k^2}{a^2} + V''(\phi_0)\right]\delta\phi_k = 0, \quad (9.35)$$

where  $a$  and  $\delta\phi_k$  denote the scale factor and the Fourier modes of  $\delta\phi(\mathbf{x}, t)$ , respectively, and the potential derivatives are given as follows:

$$V'(\phi) = \sqrt{\frac{3\alpha}{2}}m^2M_{\text{pl}}e^{-\sqrt{\frac{2}{3\alpha}}\frac{\phi}{M_{\text{pl}}}}\left(1 - e^{-\sqrt{\frac{2}{3\alpha}}\frac{\phi}{M_{\text{pl}}}}\right), \quad (9.36)$$

$$V''(\phi) = -m^2e^{-\sqrt{\frac{2}{3\alpha}}\frac{\phi}{M_{\text{pl}}}}\left(1 - 2e^{-\sqrt{\frac{2}{3\alpha}}\frac{\phi}{M_{\text{pl}}}}\right). \quad (9.37)$$

If we ignore cosmic expansion and assume the small field regime, we obtain the perturbative background just as in the previous section:

$$\begin{aligned} \phi_0 \simeq \sqrt{\alpha}M_{\text{pl}} & \left[ \frac{\sqrt{6}}{4} \left( \frac{\Phi_0}{\sqrt{\alpha}M_{\text{pl}}} \right)^2 + \frac{\Phi_0}{\sqrt{\alpha}M_{\text{pl}}} \cos(\tau) \right. \\ & \left. - \frac{\sqrt{6}}{12} \left( \frac{\Phi_0}{\sqrt{\alpha}M_{\text{pl}}} \right)^2 \cos(2\tau) + \frac{1}{18} \left( \frac{\Phi_0}{\sqrt{\alpha}M_{\text{pl}}} \right)^3 \cos(3\tau) \right], \end{aligned} \quad (9.38)$$

where  $\Phi_0$  is now a constant and  $\tau$  becomes

$$\tau = \sqrt{1 - \frac{2}{3} \left( \frac{\Phi_0}{\sqrt{\alpha}M_{\text{pl}}} \right)^2} mt, \quad (9.39)$$

which is given by Eq. (9.28) with  $f_{\chi\chi} = 0$ .

Then, Eq. (9.35) becomes the following Mathieu equation:

$$\begin{aligned} \frac{d^2}{dT^2} \delta\phi_k + \frac{1}{1 - (2/3)(\Phi_0/\sqrt{\alpha}M_{\text{pl}})^2} \left[ 4 \left( \frac{k}{ma} \right)^2 + 4 - \frac{4}{3} \left( \frac{\Phi_0}{\sqrt{\alpha}M_{\text{pl}}} \right)^2 \right. \\ \left. - 4\sqrt{6} \left( \frac{\Phi_0}{\sqrt{\alpha}M_{\text{pl}}} \right) \cos(2T) \right] \delta\phi_k \simeq 0, \end{aligned} \quad (9.40)$$

with  $T \equiv \tau/2$  and ignoring the cosmic expansion. This has an instability mode at

$$4 \left( \frac{k}{ma} \right)^2 + 4 - \frac{4}{3} \left( \frac{\Phi_0}{\sqrt{\alpha}M_{\text{pl}}} \right)^2 \simeq 4, \quad (9.41)$$

that is

$$\frac{k}{ma} \simeq \frac{1}{\sqrt{3}} \frac{\Phi_0}{\sqrt{\alpha}M_{\text{pl}}} \lesssim \frac{1}{\sqrt{3}} \simeq 0.58. \quad (9.42)$$

For  $\alpha = 1$ , however, it was concluded that the instability cannot sufficiently grow due to the quick damping of the inflaton [56]. The smaller  $\alpha$  may lead to the more efficient resonance since the Hubble rate  $H$  becomes smaller, which is proportional to  $\sqrt{\alpha}$ . We numerically solved Eq. (9.35) and found that indeed the instability grows for small  $\alpha$ , whose threshold is estimated as  $\alpha_{\text{th}}^{\text{E}} \sim 10^{-3}$ . In Fig. 9.3, we illustrate an example of instability growth for  $\alpha = 8 \times 10^{-4}$ . We set the following initial conditions:

$$\phi_i = \phi_{\text{end}} (\simeq 0.13M_{\text{pl}}), \quad (9.43)$$

$$\delta\phi_i = \mathcal{O}(10^{-5})\phi_{\text{end}}. \quad (9.44)$$

We see from the figure that the peak roughly coincides with the estimation Eq. (9.42).

The threshold  $\alpha_{\text{th}}^{\text{E}}$  is somewhat larger than that in T-models, which is reported to be about  $10^{-4}$  [25, 26]. This is expected to come from the difference in the potentials, where the negative quartic term flatten the potential in the T-models, while the cubic term plays that role in the E-models. The difference of  $\phi_{\text{end}}$  in each model is also expected to be relevant.

## 9.4 Lattice simulations

Since the non-linear dynamics is important in the I-ball formation, we performed the lattice simulation using the modified version of *LatticeEasy* [28], which is a C++ program originally designed to simulate the scalar evolution in the expanding

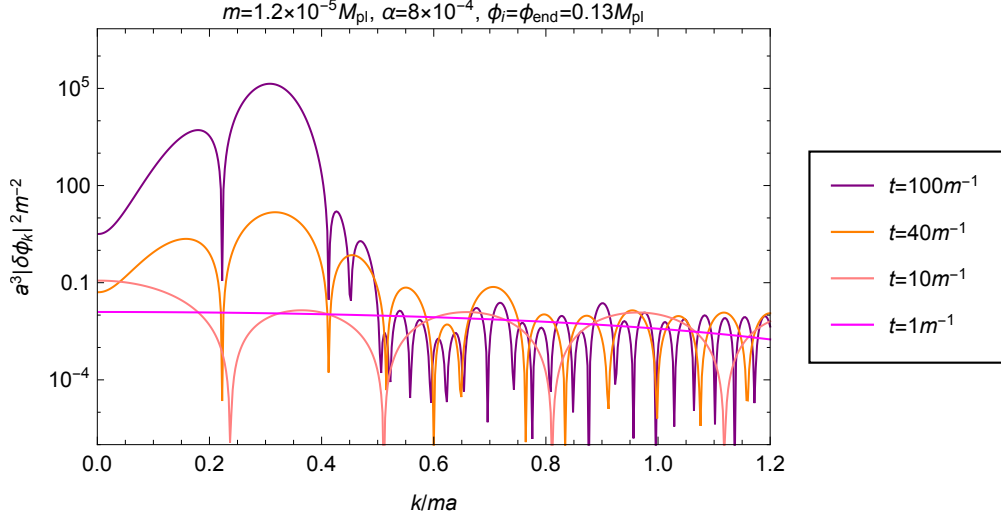


Figure 9.3: Instability bands for  $\alpha = 8 \times 10^{-4}$ ,  $\phi_i = \phi_{\text{end}} = 0.13 M_{\text{pl}}$ , which are evaluated at various times. We note that they agree with the estimation in Eq. (9.42).

	$N_{\text{grid}}$	$Lm$	$m\Delta t$
1D	1024	50	0.04
2D	$256^2$	50	0.1
3D	$128^3$	50	0.2

Table 9.1: Parameter settings for simulations.

universe. We use the leapfrog method and the Central-Difference formulas of second order for the integration.

We normalize the initial scale factor to unity, and define the Hubble rate  $H$  as

$$H = \sqrt{\frac{\langle \rho \rangle}{3M_{\text{pl}}^2}}, \quad (9.45)$$

where  $\langle \rangle$  denotes the lattice average and  $\rho$  is the energy density of the inflaton:

$$\rho = \frac{1}{2} \dot{\phi}^2 + \frac{1}{a^2} (\nabla \phi)^2 + V(\phi). \quad (9.46)$$

In Table 9.1, we present the parameter settings for the simulations, where  $N_{\text{grid}}$ ,  $L$ ,  $\Delta t$  are the number of grids, box size, and time step, respectively. In the program we

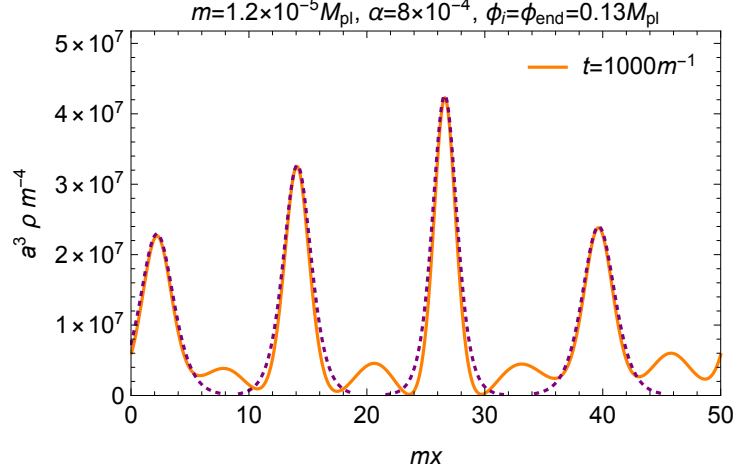


Figure 9.4: 1D lattice simulation result with  $\alpha = 8 \times 10^{-4}$ ,  $\phi_i = \phi_{\text{end}} \simeq 0.13M_{\text{pl}}$ , where we set  $N_{\text{grid}} = 1024$ ,  $Lm = 50$ . We plotted the comoving energy density at  $t = 1000m^{-1}$ , and fit the analytic profiles obtained in Sec. 9.2 to the peaks, which gives a good agreement.

used the following rescaled program variables:

$$\phi_{\text{pr}} \equiv \phi/\phi_{\text{end}}, \quad (9.47)$$

$$V_{\text{pr}} \equiv V/(m\phi_{\text{end}})^2, \quad (9.48)$$

$$t_{\text{pr}} \equiv mt, \quad (9.49)$$

$$\mathbf{x}_{\text{pr}} \equiv m\mathbf{x}, \quad (9.50)$$

where  $\mathbf{x}$ ,  $t$  denote spacetime coordinates.

In Fig. 9.4, we present the 1D simulation result, where we plotted energy density  $\rho$  after the formation. We estimate the formation time as  $t_{\text{form}} \sim O(100)m^{-1}$ . We fitted the energy density of analytic solution Eq. (9.30) to the peaks in the figure, where we can see the agreement. In Figures 9.5 and 9.6, we give the 2D and 3D simulation results, respectively, where we also plot the energy density after the fragmentation. In Fig. 9.6, we plot the energy iso-surfaces for  $a^3\rho = 5.9 \times 10^7 m^4$  and  $a^3\rho = 1.8 \times 10^8 m^4$ , where one can indeed identify the localized objects, I-balls.

## 9.5 Implications

We have confirmed that coherent oscillation of the inflaton fragments into the I-balls for small  $\alpha$ , especially for  $\alpha \lesssim 10^{-3}$ . Here we comment on their cosmological



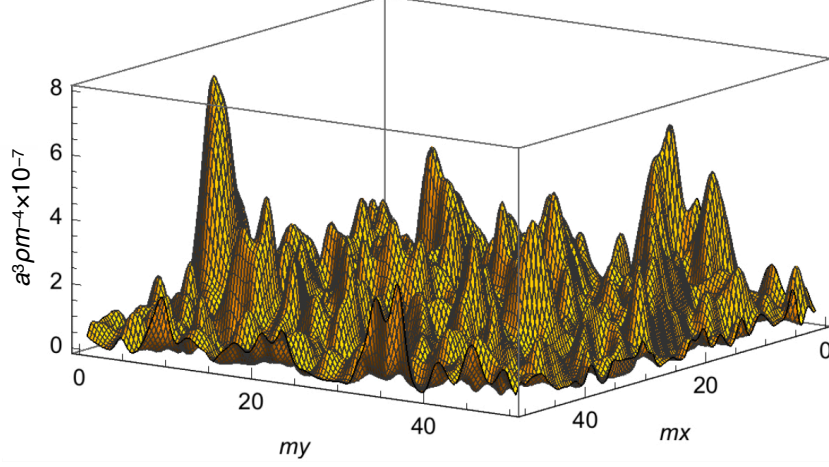


Figure 9.5: 2D lattice simulation result with  $\alpha = 8 \times 10^{-4}$  and  $\phi_i = \phi_{\text{end}} = 0.13M_{\text{pl}}$ , where we set  $N_{\text{grid}} = 256^2$ ,  $Lm = 50$ . We plotted the comoving energy density normalized by  $10^7 m^4$  at  $t = 2 \times 10^4 m^{-1}$ .

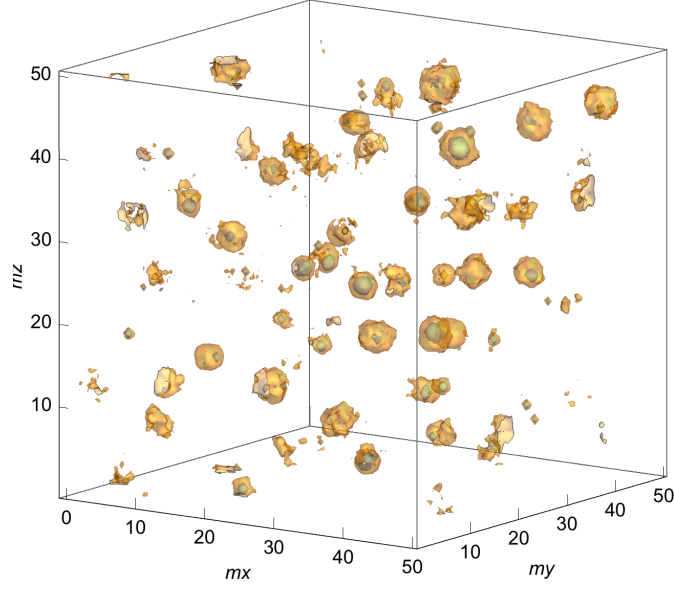


Figure 9.6: 3D lattice simulation result with  $\alpha = 8 \times 10^{-4}$  and  $\phi_i = \phi_{\text{end}} = 0.13M_{\text{pl}}$ , where we set  $N_{\text{grid}} = 128^3$ ,  $Lm = 50$ . We plotted the energy iso-surfaces for  $a^3\rho = 5.9 \times 10^7 m^4$  and  $a^3\rho = 1.8 \times 10^8 m^4$ , at  $t = 2 \times 10^4 m^{-1}$ .

implications<sup>1</sup>.

---

<sup>1</sup>The discussion here is partly based on Ref. [62], where we also examined I-ball formation in another model.

Inflaton fragmentation into I-balls can generate the gravitational waves (GWs) through the anisotropic stress tensor, and it is of interest whether their frequency  $f$  is in the currently observable range. Since  $\mathcal{O}(1-10)$  I-balls are formed per horizon, naively expected is that the frequency coincides with the Hubble scale at that time:

$$f \sim H_{\text{end}} \sim m\sqrt{\alpha} \lesssim 10^{36} \text{ Hz}, \quad (9.51)$$

where we used  $m \sim 10^{13} \text{ GeV}$  and  $\alpha \lesssim 10^{-3}$ . Then, this is redshifted until present, which can be estimated as

$$\begin{aligned} f_0 &= \frac{a_{\text{end}}}{a_0} f = \frac{a_{\text{end}}}{a_R} \frac{a_R}{a_0} f \\ &\lesssim 10^7 \text{ Hz} \times \left( \frac{\Gamma}{H_{\text{end}}} \right)^{1/6}, \end{aligned} \quad (9.52)$$

where  $\Gamma$  is the decay rate of inflaton (I-ball) and  $a_0$  and  $a_R$  represent the scale factors at present and the time of reheating, respectively, and we used  $a_R/a_0 \simeq 5.5 \times 10^{-32} \sqrt{M_{\text{pl}}/\Gamma}$  and  $a_R/a_{\text{end}} \simeq (\rho_R/\rho_{\text{end}})^{-1/3} \simeq (H_{\text{end}}/\Gamma)^{2/3}$ . This is way higher than the currently observable range of frequency [63, 64, 65], which leads us to conclude that it is quite generally difficult to generate the GWs in the observable range, through the inflaton fragmentation into I-balls.

The inflaton fragmentation alters the reheating process into the decay process of the localized objects, which may change the time when the reheating completes. These are studied in the context of Q-balls [66], where the reheating occurs through the surface effect, since the Q-ball core has a large expectation value. The I-balls, however, is a real scalar configuration and oscillates at the center as well, hence the reheating occurs over the volume. While there are some studies in particular situations, the general decaying properties of I-balls are not known well. There can be self-decay through the self-interactions  $\phi^n$  [67], and also the decay into other light particles if the proper couplings exist. In particular, it was reported that the decay into the scalar particles is exponentially enhanced due to the Bose stimulation [68], which can be understood as a spatially localized preheating. These processes must occur before the BBN.

The difference in the reheating process may also affect the predictions on the inflationary observables. As we see from Eq. (9.5, 9.6, 9.7), the predictions on the primordial perturbation depend on  $N_*$ , the  $e$ -folds at CMB pivot scale. While it is naively assumed to be  $50 \sim 60$ , it will completely be determined by the reheating temperature, which gives the beginning of the radiation era and affects the redshift of the CMB pivot scale. This implies that the I-ball formation may alter inflationary predictions through the reheating temperature.

The difference between E-models and T-models can be important. As we pointed out, the predictions from these models degenerate for  $\alpha \ll N_*$  and for

the same reheating temperatures. However, the difference arises in the conditions for the fragmentation:  $\alpha_{\text{th}}^{\text{T}} \sim 10^{-4}$ ,  $\alpha_{\text{th}}^{\text{E}} \sim 10^{-3}$ , which implies the possibility of the resolution of the degeneracy in the inflationary predictions through  $N_*$ . This also applies to other UV-motivated inflation models that predict the small tensor mode and degenerate with the  $\alpha$ -attractors for small  $\alpha$ : polyinstanton inflation ( $\alpha \sim 10^{-3}$ ) [69], Kähler moduli inflation ( $\alpha \sim 10^{-8}$ ) [70], for instance.

One expected difference in the reheating process from the usual scenario is that the universe is reheated in the spatially localized manner, and only after the locally generated radiation completely diffuses throughout the space, we get the spatially homogeneous radiation era. If we define the reheating temperature  $T_{\text{RH}}$  to be the temperature when such spatially homogeneous radiation is first realized, we find that there is an upper bound on this temperature, coming from the requirement of the efficient diffusion of the radiation.

Assume that we indeed have reached an era of homogeneous radiations. Then the diffusion length  $l_{\text{d}}$  of the photons at that time should be larger than the distance  $l_{\text{I-I}}$  between the localized I-balls:

$$l_{\text{d}} \gtrsim l_{\text{I-I}}. \quad (9.53)$$

The diffusion length  $l_{\text{d}}$  during the time  $t \sim H^{-1}$  is estimated as

$$\frac{l_{\text{d}}}{H^{-1}} \sim \sqrt{\frac{H}{\alpha_s^2 T}}, \quad (9.54)$$

where  $\alpha_s$  is the structure constant for the radiation. The distance  $l_{\text{I-I}}$  between the I-balls is given by

$$\frac{l_{\text{I-I}}}{H^{-1}} \sim N_{\text{I}}^{-1/3} \sim N_{\text{I,form}}^{-1/3} \left( \frac{H}{H_{\text{form}}} \right)^{1/3}, \quad (9.55)$$

where  $N_{\text{I}}$  denotes the total number of I-balls in the horizon, and  $_{\text{form}}$  refers to the quantities at the formation time of the I-balls. Plugging in Eqs. (9.54) and (9.55) into Eq. (9.53) and using  $H \sim T_{\text{RH}}^2/M_{\text{pl}}$ , we thus obtain the upper bound on the reheating temperature:

$$T_{\text{RH}} \lesssim 10^8 \text{ GeV} \alpha_s^{-6} N_{\text{I,form}}^2 \left( \frac{H_{\text{form}}}{10^{13} \text{ GeV}} \right)^2. \quad (9.56)$$

Since  $H_{\text{form}}$  has the same order of magnitude  $H_{\text{end}} \sim m\sqrt{\alpha}$ , as expected from the flatness of the potential (we have also checked this in the numerical simulations), it reduces to

$$T_{\text{RH}} \lesssim 10^8 \text{ GeV} \alpha_s^{-6} N_{\text{I,form}}^2 \alpha \left( \frac{m}{10^{13} \text{ GeV}} \right)^2. \quad (9.57)$$

Thus, we can see that for small  $\alpha$  and for  $\alpha_s \sim 1$ , the upper bound on the temperature for the usual radiation domination becomes severe: For instance,  $\alpha \lesssim 10^{-4}$  gives  $T_{\text{RH}} \lesssim 10^4$  GeV.

Again, we note that  $T_{\text{RH}}$  defined here is the temperature at the onset of the standard homogeneous radiation era; the cosmological scenario before this time can potentially be altered from the usual scenarios, due to the localization of the radiation produced from the I-balls. For instance, the temperature at the energy core, which will coincide with the location of the I-balls, may be higher than predicted by the usual perturbative decay rate of the inflaton, which in turn may lead to the localized thermal leptogenesis.

## 9.6 Brief summary

Recently proposed  $\alpha$ -attractors are categorized into two subclasses: T-models and E-models, which are favored by the observations, due to the flatness of the potentials. This flatness makes the inflaton fragment into the I-balls, which is the second issue of this thesis. We investigated the possibility of the formation of I-balls in E-models. By using the linear instability analysis, and also performing the lattice simulation, we concluded that the I-balls are formed for small  $\alpha$ , whose threshold is also obtained as  $\alpha_{\text{th}}^{\text{E}} \sim 10^{-3}$ . This value is rather larger than in the case of T-models, which is about  $\alpha_{\text{th}}^{\text{T}} \sim 10^{-4}$ . This difference is due to the different behavior in the potential, especially the cubic term in the E-models, which is absent in the T-models. Inflaton fragmentation produces the GWs through the anisotropic stress tensor. However, since its frequency is naively expected to be about the horizon scale (inverse) at that time, it may be challenging to coincide with the currently observable range. Indeed, our estimation suggests that it is quite generally difficult to produce the GWs in the observable range through the inflaton fragmentation, even after the redshift until present. The inflaton fragmentation can alter the reheating process from the usual perturbative one, which may affect the cosmological scenarios such as baryogenesis, gravitino production. The inflationary predictions on observables  $n_s$  and  $r$  can also be changed, since the e-folds  $N_*$  for the CMB pivot scale is related to the reheating temperature. We pointed out a specific change in the reheating that the plasma is locally generated, which must efficiently diffuse to realize the usual homogeneous radiation era. We gave the upper bound on the temperature for the usual radiation domination, which can be severe for small  $\alpha$ . For higher temperature, it is expected that the spatial gradient of temperature exists due to the inefficient diffusion of the radiation from the locations of the I-balls.

# Chapter 10

## Conclusions

The non-topological solitons can have various implications in cosmology. In this thesis, we studied the charged soliton dark matter scenario. As a specific candidate, we considered charged Q-balls in the two scalar model and studied the possibility of realization of charged Q-balls from  $B$  and  $L$  direction through the leptonic decay only. We found an upper bound on the electric charge of charged Q-ball coming from the Schwinger limit, which we estimated as  $\mathcal{O}(100)$ . We considered charged Q-balls and anti-Q-balls with the charge of  $\mathcal{O}(100)$  and studied the relics in the present universe, which we concluded to be massive atomic objects. These relics are detectable by the usual electromagnetic processes, unlike the global Q-balls. The most stringent constraint on the charged Q-ball relics comes from the MICA direct detection, where the authors reported non-detection of the trail of massive atomic object in  $10^9$  years old ancient mica crystal, whose stringency is due to the long detection time: the age of the mica. The constraint is translated into that on the model parameters and reheating temperature, once we require the present relics to be the dark matter. As a result, we found that the MICA constraint is severer than that from IceCube, which probes neutral Q-ball process, or KKST process, which leads to the smaller allowed region.

We derived the decay rate of the charged Q-ball into fermions, using the semi-classical approximation. We confirmed that the decay rate into particles with the charge of the same sign is enhanced compared to the case of the global Q-ball, due to the electric repulsion. On the other hand, we found that the decay rates saturate for sufficiently strong Yukawa interaction, just as in the case of the global Q-ball. However, the saturated rate is somewhat larger than that is predicted by the classical formula, which is obtained as the integration of fully occupied phase space at the surface of the Q-ball. We found that the disagreement can be interpreted as a tunneling effect, where the fermions, which are mainly produced by  $\phi$  due to the strong Yukawa interaction, come out as a saturated flux, and immediately bump into the Coulomb barrier and tunnel through it. We confirmed

the suppression compared to the saturated rate when the Coulomb barrier outside does not exist. We also found the enhancement of the production rate normalized by saturated rate for  $g\phi_0/\omega \ll 1$  when  $e^2$  or  $Q$  becomes large, which is analogous to the case of the global Q-ball, where the production rate enhances when  $\phi$  is large near the surface, since the electric repulsion of the charged Q-ball deforms the profile and pushes the charge to the surface.

In our charged Q-ball DM scenario, we implicitly assumed the sufficiently fast decay of the leptonic component, which forms the charged Q-balls in the early universe. Since these Q-balls are formed after the AD mechanism with very large charge, typically larger than  $10^{20}$ , the production rates are expected to be saturated. Furthermore, the maximal electric charge is only about  $\mathcal{O}(100)$ , hence the size and the maximal momentum of the outgoing particle at the surface of the Q-ball are nearly the same as in the case of the global Q-ball. Thus, the saturated rate almost coincides with that of the global Q-ball, which is typically known to be of the order of GeV. This validates our assumption that the decay of the charged Q-balls is sufficiently fast.

Due to the stability of the baryonic component and very small amount of leptonic decay, the baryon asymmetry in the universe can only be generated through the evaporation of Q-balls due to the temperature effects. However, very low reheating temperature is realized in the Q-ball DM scenario, hence the generated baryon number is too small to explain the baryon asymmetry in the universe [71]. Baryogenesis will be possible if we use another flat direction.

As the second topic of this thesis on the non-topological solitons, we studied inflaton fragmentation into I-balls in E-models of  $\alpha$ -attractors.  $\alpha$ -attractors are favored by the observations due to the asymptotic flatness of the potentials, which can lead to the I-ball formation. By using the linear instability analysis and performing the lattice simulation, we confirmed that the I-balls are formed for  $\alpha \lesssim \alpha_{\text{th}}^{\text{E}} \sim 10^{-3}$ . This is somewhat larger than the case of T-models,  $\alpha_{\text{th}}^{\text{T}} \sim 10^{-4}$ , which may come from the different behavior in the potential, especially the cubic term in the E-models, which is absent in the T-models.

I-ball formation from the inflaton induces the anisotropic stress tensor and generates the GWs. However, we concluded that due to the coincidence of the frequency to the horizon scale at the formation time, it may be difficult to be in the observable range. The inflaton fragmentation into I-balls may also alter the cosmological scenario after the inflation, especially the reheating process into the SM radiation, which in turn will affect the various temperature-dependent events including baryogenesis, the production of dangerous relics, etc. It may also affect the inflationary observables  $n_s$  and  $r$ , since the e-folds  $N_*$  depends on the post-inflationary events through the reheating temperature. We discussed that the locally generated plasma may not efficiently diffuse to realize the usual homogeneous

radiation-dominated universe. We derived an upper bound for the temperature of the usual homogeneous radiation-dominated universe, requiring the efficient diffusion of the locally produced radiation at that temperature. We found that the upper bound can be quite serious for small  $\alpha$ . If the temperature is higher, there will be the spatial gradient of temperature, since the locally generated radiation will not diffuse rapidly throughout the space, whose details will be pursued in the near future.

# Acknowledgements

I would like to thank my supervisor Masahiro Kawasaki for his guidance and supports. Despite my ignorance and immaturity, he always encouraged me and led me to this moment. I admire his academic attitudes and I will pursue them throughout the rest of my academic career. Masahiro Ibe, who is also a faculty member of the same group, always gave me deep academic advice and kindly answered my elementary questions. This thesis is gratefully examined by Jun'ichi Yokoyama, Hitoshi Murayama, Kipp Cannon, Masayuki Nakahata, and Masato Shiozawa. I also appreciate lots of advice from my seniors. Masaki Yamada, being my first collaborator, gave me not only the academic, but also every kind of practical knowledge that is necessary in this field. He always gave me a positive feedback for an even very elementary progress I made. Naoyuki Takeda was a very tolerant and open person and always helped me in getting used to the lab life. I express the same gratitude to all the other seniors and colleagues including Taku Hayakawa and Tasuku Aizawa. I would like to thank my collaborators. Kunio Kaneta and Naoya Kitajima, who are also my seniors, helped me to experience for the first time the Korean academic community, besides the research itself. Hyungjin Kim and Chang Sub Shin are my first collaborators in Korea, who were very open-minded people and kindly accepted me into the project. I would like to thank Fuminori Hasegawa for extensive discussions throughout this year and collaborating with me. He always shared many fruitful ideas with me, which helped me to approach to a decent level in this field. I would like to thank Masahito Yamazaki for the collaboration, and also for the advice and encouragements in my doctoral course. Finally, I would like to thank my family, especially my parents, who have always guided me into the constant learning of the valuable things in life and especially supported my pursuit of this field of study.



# Appendix A

## Notations

- We adopt the following natural unit:

$$c = 3.0 \times 10^8 \text{ m s}^{-1} = 1, \quad (\text{A.1})$$

$$\hbar = 6.6 \times 10^{-16} \text{ eV s} = 1, \quad (\text{A.2})$$

$$k_B = 8.6 \times 10^{-5} \text{ eV K}^{-1} = 1, \quad (\text{A.3})$$

where  $c, \hbar, k_B$  denote the speed of light, the Dirac constant, and the Boltzmann constant, respectively.

- We write the reduced Planck mass as

$$M_{\text{pl}} = (\hbar c / 8\pi G)^{1/2} = (8\pi G)^{-1/2} = 2.4 \times 10^{18} \text{ GeV}, \quad (\text{A.4})$$

where  $G$  is the Newton constant.

- We write the Cartesian coordinates as  $(x, y, z)$ .
- We write the spherical polar coordinates as  $(r, \theta, \phi)$ .
- Latin indices  $i, j, k, \dots$  run over the three spatial indices 1, 2, 3.
- Greek indices  $\mu, \nu, \dots$  run over the four spacetime indices 0, 1, 2, 3, with 0 the time component.
- The sign of the metric is chosen as  $(+, -, -, -)$ .
- The bold characters  $\mathbf{p}, \mathbf{k}$ , etc. denote the three-vectors.
- The normal characters  $p, k$ , etc. denote the norm of the three-vectors  $\mathbf{p}, \mathbf{k}$ , etc.
- $\nabla$  is the three-dimensional gradient.

- $\Delta$  is the three-dimensional Laplacian.
- The power spectrum of the operator  $\mathcal{O}(\mathbf{x})$  is defined as

$$\mathcal{P}_{\mathcal{O}}(k) = \frac{k^3}{2\pi^2} P_{\mathcal{O}}(k), \quad (\text{A.5})$$

where

$$P_{\mathcal{O}}(k) = \int d^3x \langle \mathcal{O}(\mathbf{x}) \mathcal{O}(\mathbf{y}) \rangle e^{-i\mathbf{k} \cdot (\mathbf{x} - \mathbf{y})}. \quad (\text{A.6})$$

# Appendix B

## Geometry in the expanding spacetime

In this chapter, we summarize the geometric formulas, including the Christoffel symbols, Ricci tensor, and Ricci scalar, in the perturbed Friedmann-Robertson-Walker metric.

### B.1 Geometry in FRW metric

The cosmological principle states that the universe is nearly homogeneous and isotropic, which gives the Friedmann-Robertson-Walker (FRW) metric with small fluctuations. In this section, we summarize the geometric structure in the FRW metric, or at zeroth-order.

#### B.1.1 Metric

We consider the following FRW metric:

$$ds^2 = g_{\mu\nu} dx^\mu dx^\nu \tag{B.1}$$

$$= dt^2 - a^2(t) \left[ \frac{dr^2}{1 - Kr^2} + r^2 (d\theta^2 + \sin^2 \theta d\phi^2) \right], \tag{B.2}$$

which is determined by the cosmological principle. We wrote the scale factor as  $a(t)$ , and the constant  $K$  gives the spatial curvature of the universe.

### B.1.2 Christoffel symbols

The Christoffel symbols for a given metric  $g_{\mu\nu}$  is defined as follows:

$$\Gamma_{\alpha\beta}^{\mu} \equiv \frac{1}{2}g^{\mu\nu} \left( \frac{\partial g_{\alpha\nu}}{\partial x^{\beta}} + \frac{\partial g_{\beta\nu}}{\partial x^{\alpha}} - \frac{\partial g_{\alpha\beta}}{\partial x^{\nu}} \right), \quad (\text{B.3})$$

whose components are listed below. We give the formulas for spherical polar coordinates  $(r, \theta, \phi)$ , and flat Cartesian coordinates  $(x, y, z)$ .

#### Spherical polar coordinates

First, the components having the time indices are given as follows:

$$\Gamma_{00}^0 = \Gamma_{0i}^0 = \Gamma_{i0}^0 = \Gamma_{00}^i = 0, \quad (\text{B.4})$$

$$\Gamma_{ij}^0 = -\frac{\dot{a}}{a}g_{ij}, \quad (\text{B.5})$$

$$\Gamma_{0j}^i = \Gamma_{j0}^i = \frac{\dot{a}}{a}\delta_j^i, \quad (\text{B.6})$$

and the spatial components become

$$\Gamma_{rr}^r = \frac{Kr}{1 - Kr^2}, \quad (\text{B.7})$$

$$\Gamma_{\theta\theta}^r = -r(1 - Kr^2), \quad (\text{B.8})$$

$$\Gamma_{\phi\phi}^r = -r(1 - Kr^2)\sin^2\theta, \quad (\text{B.9})$$

$$\Gamma_{r\theta}^r = \Gamma_{\theta r}^r = \Gamma_{\theta\phi}^r = \Gamma_{\phi\theta}^r = \Gamma_{\phi r}^r = \Gamma_{r\phi}^r = 0, \quad (\text{B.10})$$

$$\Gamma_{r\theta}^{\theta} = \Gamma_{\theta r}^{\theta} = \frac{1}{r}, \quad (\text{B.11})$$

$$\Gamma_{\phi\phi}^{\theta} = -\sin\theta\cos\theta, \quad (\text{B.12})$$

$$\Gamma_{rr}^{\theta} = \Gamma_{\phi r}^{\theta} = \Gamma_{r\phi}^{\theta} = \Gamma_{\theta\theta}^{\theta} = \Gamma_{\theta\phi}^{\theta} = \Gamma_{\phi\theta}^{\theta} = 0, \quad (\text{B.13})$$

$$\Gamma_{\phi r}^{\phi} = \Gamma_{r\phi}^{\phi} = \frac{1}{r}, \quad (\text{B.14})$$

$$\Gamma_{\theta\phi}^{\phi} = \Gamma_{\phi\theta}^{\phi} = \frac{\cos\theta}{\sin\theta}, \quad (\text{B.15})$$

$$\Gamma_{rr}^{\phi} = \Gamma_{r\theta}^{\phi} = \Gamma_{\theta r}^{\phi} = \Gamma_{\theta\theta}^{\phi} = \Gamma_{\phi\phi}^{\phi} = 0. \quad (\text{B.16})$$

### Flat Cartesian coordinates

The Christoffel symbols for flat ( $K = 0$ ) Cartesian coordinates are given as follows:

$$\Gamma_{00}^0 = \Gamma_{0i}^0 = \Gamma_{i0}^0 = \Gamma_{00}^i = \Gamma_{jk}^i = 0, \quad (\text{B.17})$$

$$\Gamma_{ij}^0 = -\frac{\dot{a}}{a}g_{ij}, \quad (\text{B.18})$$

$$\Gamma_{0j}^i = \Gamma_{j0}^i = \frac{\dot{a}}{a}\delta_j^i. \quad (\text{B.19})$$

### B.1.3 Ricci tensor and scalar

The Ricci tensor is defined as follows:

$$R_{\mu\nu} \equiv \frac{\partial \Gamma_{\mu\nu}^\alpha}{\partial x^\alpha} - \frac{\partial \Gamma_{\mu\alpha}^\nu}{\partial x^\alpha} + \Gamma_{\beta\alpha}^\alpha \Gamma_{\mu\nu}^\beta - \Gamma_{\beta\nu}^\alpha \Gamma_{\mu\alpha}^\beta, \quad (\text{B.20})$$

whose components are calculated as

$$R_{00} = -3\frac{\ddot{a}}{a} \quad (\text{B.21})$$

$$R_{0i} = R_{i0} = 0, \quad (\text{B.22})$$

$$R_{ij} = -\left[\frac{\ddot{a}}{a} + 2\left(\frac{\dot{a}}{a}\right)^2 + 2\frac{K}{a^2}\right]g_{ij}. \quad (\text{B.23})$$

The Ricci scalar is defined by contracting the Ricci tensor:

$$R \equiv g^{\mu\nu}R_{\mu\nu} \quad (\text{B.24})$$

$$= -6\left[\frac{\ddot{a}}{a} + \left(\frac{\dot{a}}{a}\right)^2 + \frac{K}{a^2}\right]. \quad (\text{B.25})$$

Finally, we also give the three-dimensional Ricci tensor and scalar:

$$R_{ij}^{(d=3)} = -\frac{2K}{a^2}g_{ij}, \quad (\text{B.26})$$

$$R^{(d=3)} = -\frac{6K}{a^2}, \quad (\text{B.27})$$

where we can see that the constant  $K$  indeed gives the three-dimensional curvature.

## B.2 Geometry in perturbed metric

In this section, we give the geometric formulas for the perturbed FRW metric.

### B.2.1 Metric

We consider the following perturbed FRW metric:

$$ds^2 = (\bar{g}_{\mu\nu} + \delta g_{\mu\nu}) dx^\mu dx^\nu \quad (\text{B.28})$$

$$= (1 + 2A)dt^2 - 2a(\partial_i B - S_i)dt dx^i - a^2 [(1 - 2\psi)\delta_{ij} + 2\partial_i \partial_j E + \partial_i F_j + \partial_j F_i + h_{ij}] dx^i dx^j, \quad (\text{B.29})$$

with  $\partial_i S_i = \partial_i F_i = \partial_i h_{ij} = h_{ii} = 0$ , where  $\bar{g}_{\mu\nu}$  and  $\delta g_{\mu\nu}$  denote the background FRW metric and perturbed metric, respectively. We summarize the first-order terms for Christoffel symbols, Ricci tensor and scalar in the following.

### B.2.2 Christoffel symbols

The perturbations of the Christoffel symbols are given as follows:

$$\delta\Gamma_{\alpha\beta}^\mu = \frac{1}{2}\delta g^{\mu\nu} \left( \frac{\partial \bar{g}_{\alpha\nu}}{\partial x^\beta} + \frac{\partial \bar{g}_{\beta\nu}}{\partial x^\alpha} - \frac{\partial \bar{g}_{\alpha\beta}}{\partial x^\nu} \right) + \frac{1}{2}\bar{g}^{\mu\nu} \left( \frac{\partial \delta g_{\alpha\nu}}{\partial x^\beta} + \frac{\partial \delta g_{\beta\nu}}{\partial x^\alpha} - \frac{\partial \delta g_{\alpha\beta}}{\partial x^\nu} \right), \quad (\text{B.30})$$

whose components are listed below, where we plugged in the background FRW metric  $\bar{g}_{\mu\nu}$  (inverse  $\bar{g}^{\mu\nu}$ ).

$$\delta\Gamma_{00}^0 = \frac{1}{2}\partial_0 \delta g_{00}, \quad (\text{B.31})$$

$$\delta\Gamma_{0i}^0 = \delta\Gamma_{i0}^0 = -\frac{\dot{a}}{a}\delta g_{0i} + \frac{1}{2}\partial_i \delta g_{00}, \quad (\text{B.32})$$

$$\delta\Gamma_{ij}^0 = \frac{1}{2}(-2a\dot{a}\delta_{ij}\delta g_{00} + \partial_i \delta g_{j0} + \partial_j \delta g_{i0} - \partial_0 \delta g_{ij}), \quad (\text{B.33})$$

$$\delta\Gamma_{00}^i = \frac{1}{2a^2}\delta^{ij}(-2\partial_0 \delta g_{0j} + \partial_j \delta g_{00}), \quad (\text{B.34})$$

$$\delta\Gamma_{0j}^i = \delta\Gamma_{j0}^i = \frac{1}{2a^2}\delta^{ik} \left( 2\frac{\dot{a}}{a}\delta g_{kj} - \partial_0 \delta g_{kj} - \partial_j \delta g_{k0} + \partial_k \delta g_{j0} \right), \quad (\text{B.35})$$

$$\delta\Gamma_{jk}^i = \frac{1}{2a^2}\delta^{il}(2a\dot{a}\delta_{jk}\delta g_{l0} - \partial_j \delta g_{kl} - \partial_k \delta g_{jl} + \partial_l \delta g_{jk}). \quad (\text{B.36})$$

### B.2.3 Ricci tensor and scalar

The perturbations of the Ricci tensor are given as

$$\delta R_{\mu\nu} = \frac{\partial \delta\Gamma_{\mu\nu}^\alpha}{\partial x^\alpha} - \frac{\partial \delta\Gamma_{\mu\alpha}^\nu}{\partial x^\alpha} + \delta\Gamma_{\beta\alpha}^\alpha \bar{\Gamma}_{\mu\nu}^\beta + \bar{\Gamma}_{\beta\alpha}^\alpha \delta\Gamma_{\mu\nu}^\beta - \delta\Gamma_{\beta\nu}^\alpha \bar{\Gamma}_{\mu\alpha}^\beta - \bar{\Gamma}_{\beta\nu}^\alpha \delta\Gamma_{\mu\alpha}^\beta, \quad (\text{B.37})$$

where bar denotes the background values of Christoffel symbols, which are given in the previous section. In the following we write down the components, plugging in the background FRW metric, and also the background Christoffel symbols in the previous section:

$$\begin{aligned}\delta R_{00} = & \frac{1}{2a^2}\Delta\delta g_{00} + \frac{3}{2}\frac{\dot{a}}{a}\partial_0\delta g_{00} - \frac{1}{a^2}\delta^{ij}\partial_i\partial_0\delta g_{j0} \\ & + \frac{1}{2a^2}\delta^{ij}\left[\partial_0^2\delta g_{ij} - 2\frac{\dot{a}}{a}\partial_0\delta g_{ij} + 2\left(\frac{\dot{a}^2}{a^2} - \frac{\ddot{a}}{a}\right)\delta g_{ij}\right],\end{aligned}\quad (\text{B.38})$$

$$\begin{aligned}\delta R_{0i} = \delta R_{i0} = & \frac{\dot{a}}{a}\partial_i\delta g_{00} - \left(\frac{\ddot{a}}{a} + 2\frac{\dot{a}^2}{a^2}\right)\delta g_{0i} + \frac{1}{2a^2}(\Delta\delta g_{0i} - \delta^{jk}\partial_i\partial_j\delta g_{0k}) \\ & + \frac{1}{2}\frac{d}{dt}\left[\frac{1}{a^2}\delta^{jk}(\partial_i\delta g_{jk} - \partial_j\delta g_{ki})\right],\end{aligned}\quad (\text{B.39})$$

$$\begin{aligned}\delta R_{ij} = & -\frac{1}{2}\partial_i\partial_j\delta g_{00} - (2\dot{a}^2 + a\ddot{a})\delta g_{00}\delta_{ij} - \frac{1}{2}a\dot{a}\partial_0\delta g_{00}\delta_{ij} \\ & + \frac{1}{2a^2}(\Delta\delta g_{ij} - \delta^{kl}\partial_i\partial_k\delta g_{jl} - \delta^{kl}\partial_j\partial_k\delta g_{il} + \delta^{kl}\partial_i\partial_j\delta g_{kl}) \\ & - \frac{1}{2}\partial_0^2\delta g_{ij} + \frac{1}{2}\frac{\dot{a}}{a}(\partial_0\delta g_{ij} - \delta_{ij}\delta^{kl}\partial_0\delta g_{kl}) + \frac{\dot{a}^2}{a^2}(-2\delta g_{ij} + \delta_{ij}\delta^{kl}\delta g_{kl}) \\ & + \frac{\dot{a}}{a}\delta_{ij}\delta^{kl}\partial_k\delta g_{0l} + \frac{1}{2}(\partial_i\partial_0\delta g_{j0} + \partial_j\partial_0\delta g_{i0}) + \frac{1}{2}\frac{\dot{a}}{a}(\partial_i\delta g_{j0} + \partial_j\delta g_{i0}).\end{aligned}\quad (\text{B.40})$$

The perturbation of the Ricci scalar is given as follows:

$$\delta R = \delta g^{\mu\nu}\bar{R}_{\mu\nu} + \bar{g}^{\mu\nu}\delta R_{\mu\nu}\quad (\text{B.41})$$

$$\begin{aligned} = & \frac{1}{a^2}\Delta\delta g_{00} + 6\left(\frac{\dot{a}^2}{a^2} + \frac{\ddot{a}}{a}\right)\delta g_{00} + 3\frac{\dot{a}}{a}\partial_0\delta g_{00} \\ & - 4\frac{\dot{a}}{a^3}\delta^{ij}\delta g_{0j} - \frac{2}{a^2}\delta^{ij}\partial_i\partial_0\delta g_{j0} + \frac{1}{a^2}\delta^{ij}\partial_0^2\delta g_{ij} \\ & - \frac{1}{a^4}\delta^{ij}\Delta\delta g_{ij} + \frac{1}{a^4}\delta^{ij}\delta^{kl}\partial_i\partial_k\delta g_{jl} - 2\frac{\dot{a}^2}{a^4}\delta^{ij}\delta g_{ij} - 2\frac{\ddot{a}}{a^3}\delta^{ij}\delta g_{ij}.\end{aligned}\quad (\text{B.42})$$

Finally, here we also give the perturbations of three-dimensional Ricci tensor and scalar:

$$\delta R_{ij}^{(d=3)} = -\frac{2}{a^2}(\Delta\delta g_{ij} + \partial_i\partial_j\delta^{kl}\delta g_{kl} - \delta^{kl}\partial_i\partial_k\delta g_{jl} - \delta^{kl}\partial_j\partial_k\delta g_{il}),\quad (\text{B.43})$$

$$\delta R^{(d=3)} = -\frac{1}{a^4}(\delta^{ij}\Delta\delta g_{ij} - \delta^{ij}\delta^{kl}\partial_i\partial_k\delta g_{jl}).\quad (\text{B.44})$$

Here if we use the specific form of the metric perturbation, the perturbation of the three-dimensional Ricci scalar becomes

$$\delta R^{(d=3)} = -\frac{4}{a^2}\Delta\psi. \quad (\text{B.45})$$

This implies that  $\psi$  induces the spatial curvature, which is the reason why it is called curvature perturbation.



# Appendix C

## Flat directions in MSSM

Here we list down the flat directions in MSSM, which are parametrized by the following gauge invariant monomials [37]:

	$B - L$	Lifted by renormalizable $W$
$H_u H_d$	0	$\times$
$L H_u$	-1	$\times$
$u^c d^c d^c$	-1	$\times$
$L L e^c$	-1	$\times$
$Q d^c L$	-1	$\times$
$Q u^c H_u$	0	$\circ$
$Q d^c H_d$	0	$\circ$
$L H_d e^c$	0	$\circ$
$Q Q Q L$	0	$\times$
$Q u^c Q d^c$	0	$\times$
$Q u^c L e^c$	0	$\times$
$u^c u^c d^c e^c$	0	$\times$
$Q u^c H_d e^c$	1	$\circ$
$Q Q Q H_d$	1	$\circ$

	$B - L$	Lifted by renormalizable $W$
$d^c d^c d^c LL$	-3	$\times$
$u^c u^c u^c e^c e^c$	1	$\times$
$Qu^c Qu^c e^c$	1	$\times$
$QQQQu^c$	1	$\times$
$d^c d^c d^c LH_d$	-2	$\bigcirc$
$u^c u^c d^c Qd^c H_u$	-1	$\bigcirc$
$(QQQ)_4 LLH_u$	-1	$\bigcirc$
$(QQQ)_4 LH_u H_d$	0	$\bigcirc$
$(QQQ)_4 H_u H_d H_d$	1	$\bigcirc$
$(QQQ)_4 LLLe^c$	-1	$\times$
$u^c u^c d^c Qd^c Qd^c$	-1	$\times$
$(QQQ)_4 LLH_d e^c$	0	$\bigcirc$
$(QQQ)_4 LH_d H_d e^c$	1	$\bigcirc$
$(QQQ)_4 H_d H_d H_d e^c$	2	$\bigcirc$

where  $_4$  denotes the contraction into the  $\mathbf{4}$  representation of the  $SU(2)$ .

Here we summarize the superpotentials that lift up the flat directions. The field components of the flat direction are listed in the top row, while the superpotentials in the left column.

	$Q$ $L$	$Q$ $u^c$	$L$ $d^c$	$L$ $e^c$	$u^c$ $d^c$	$u^c$ $e^c$	$Q$ $L$ $u^c$	$Q$ $L$ $d^c$	$Q$ $L$ $e^c$	$Q$ $u^c$ $d^c$	$Q$ $u^c$ $e^c$	$L$ $u^c$ $d^c$	$L$ $d^c$ $e^c$	$L$ $u^c$ $e^c$	$u^c$ $d^c$ $e^c$
$H_u Q u^c$		○					○			○	○				
$H_d L e^c$						○			○				○	○	
$H_d Q d^c$								○		○					
$Q Q Q L$	○	○					○	○	○	○	○				
$Q u^c Q d^c$		○					○	○		○	○				
$Q u^c L e^c$									○		○			○	
$u^c u^c d^c e^c$					○	○				○	○	○		○	○
$H_u L Q d^c L$															
$H_u L u^c d^c d^c$												○			
$H_u L L L e^c$				○									○		
$H_d L d^c d^c d^c$			○									○	○		
$Q d^c L Q d^c L$															
$u^c d^c d^c Q d^c L$												○			
$u^c d^c d^c u^c d^c d^c$					○							○			
$Q d^c L L L e^c$															
$L L e^c L L e^c$				○											
$L L e^c u^c d^c d^c$												○			
$H_u L L L d^c d^c d^c$			○												
$Q u^c Q u^c Q u^c H_d e^c e^c$											○				

	$Q$ $u^c$ $d^c$ $e^c$	$Q$ $L$ $u^c$ $d^c$	$Q$ $L$ $d^c$ $e^c$	$Q$ $L$ $u^c$ $e^c$	$L$ $u^c$ $d^c$ $e^c$	$Q$ $L$ $u^c$ $d^c$ $e^c$
$H_u Q u^c$	○	○		○		○
$H_d L e^c$			○	○	○	○
$H_d Q d^c$	○	○	○			○
$Q Q Q L$	○	○	○	○		○
$Q u^c Q d^c$	○	○	○	○		○
$Q u^c L e^c$	○	○	○	○	○	○
$u^c u^c d^c e^c$	○	○		○	○	○
$H_u L Q d^c L$						
$H_u L u^c d^c d^c$						
$H_u L L L e^c$						
$H_d L d^c d^c d^c$						
$Q d^c L Q d^c L$						
$u^c d^c d^c Q d^c L$						
$u^c d^c d^c u^c d^c d^c$						
$Q d^c L L L e^c$						
$L L e^c L L e^c$						
$L L e^c u^c d^c d^c$						
$H_u L L L d^c d^c d^c$						
$Q u^c Q u^c Q u^c H_d e^c e^c$						

# Appendix D

## Fermions outside the charged Q-ball

The fermions in the presence of the Coulomb potential of the form  $\sim 1/r$  can be solved analytically, which gives the solution outside the charged Q-ball. In this appendix, we show these solutions and their asymptotic behaviors, which will become spherical waves with additional phase factors.

The radial parts of the equations of motion for  $\chi$  (see Eq. (7.60)) becomes

$$\left(k_+ - q_\chi \frac{e^2 Q}{r}\right) f_\chi + \left(\frac{\partial}{\partial r} + \frac{3/2 + j}{r}\right) g_\chi = 0, \quad (\text{D.1})$$

$$\left(k_+ - q_\chi \frac{e^2 Q}{r}\right) g_\chi - \left(\frac{\partial}{\partial r} + \frac{1/2 - j}{r}\right) f_\chi = 0, \quad (\text{D.2})$$

where we used the relation  $\boldsymbol{\sigma} \cdot \nabla \Phi(j, m, j \pm 1/2) = \Phi(j, m, j \mp 1/2) \times [\partial/\partial r + (1 \pm (j + 1/2))/r]$ .

These equations are known to have the solutions of the following forms:

$$\begin{aligned}
f_\chi(r) = & \frac{e^{ik_+r}}{r} \left[ r^{s_0} C_+ \left[ {}_1F_1(s_0 + iq_\chi e^2 Q, 2s_0 + 1; -2ik_+r) \right. \right. \\
& + \frac{s_0 + iq_\chi e^2 Q}{j + 1/2} {}_1F_1(s_0 + 1 + iq_\chi e^2 Q, 2s_0 + 1; -2ik_+r) \left. \right] \\
& + r^{-s_0} C_- \left[ {}_1F_1(-s_0 + iq_\chi e^2 Q, -2s_0 + 1; -2ik_+r) \right. \\
& + \frac{-s_0 + iq_\chi e^2 Q}{j + 1/2} {}_1F_1(-s_0 + 1 + iq_\chi e^2 Q, -2s_0 + 1; -2ik_+r) \left. \right] \Bigg], \quad (D.3)
\end{aligned}$$

$$\begin{aligned}
g_\chi(r) = & i \frac{e^{ik_+r}}{r} \left[ r^{s_0} C_+ \left[ {}_1F_1(s_0 + iq_\chi e^2 Q, 2s_0 + 1; -2ik_+r) \right. \right. \\
& + \frac{s_0 + iq_\chi e^2 Q}{j + 1/2} {}_1F_1(s_0 + 1 + iq_\chi e^2 Q, 2s_0 + 1; -2ik_+r) \left. \right] \\
& - r^{-s_0} C_- \left[ {}_1F_1(-s_0 + iq_\chi e^2 Q, -2s_0 + 1; -2ik_+r) \right. \\
& + \frac{-s_0 + iq_\chi e^2 Q}{j + 1/2} {}_1F_1(-s_0 + 1 + iq_\chi e^2 Q, -2s_0 + 1; -2ik_+r) \left. \right] \Bigg], \quad (D.4)
\end{aligned}$$

where we defined  $s_0 = \sqrt{(j + 1/2)^2 - (q_\chi e^2 Q)^2}$ , and used the following confluent hypergeometric function:

$${}_1F_1(a, b; z) \equiv \sum_{k=0}^{\infty} \frac{a(a+1) \cdots (a+k-1)}{b(b+1) \cdots (b+k-1)} \frac{z^k}{k!}. \quad (D.5)$$

Then, if we use the following asymptotic form,

$${}_1F_1(a, b; z) \sim \Gamma(b) \left( \frac{e^z z^{a-b}}{\Gamma(a)} + \frac{(-1)^{-a} z^{-a}}{\Gamma(b-a)} \right), \quad |z| \gg 1 \quad (D.6)$$

we obtain the following behavior at infinity:

$$\begin{aligned}
f_\chi \sim & \left[ C_+ \frac{s_0 + iq_\chi e^2 Q}{j + 1/2} \left( (-1)^{s_0} \frac{(-i)^{-s_0 + iq_\chi e^2 Q} \Gamma(2s_0 + 1)}{\Gamma(s_0 + 1 + iq_\chi e^2 Q)} \right) \right. \\
& + C_- \frac{-s_0 + iq_\chi e^2 Q}{j + 1/2} \left( (-1)^{-s_0} \frac{(-i)^{s_0 + iq_\chi e^2 Q} \Gamma(-2s_0 + 1)}{\Gamma(-s_0 + 1 + iq_\chi e^2 Q)} \right) \left. \right] \times \frac{e^{-ik_+ r + iq_\chi e^2 Q \log(2kr)}}{r} \\
& + \left[ C_+ \left( (-1)^{s_0} \frac{i^{-s_0 - iq_\chi e^2 Q} \Gamma(2s_0 + 1)}{\Gamma(s_0 + 1 - iq_\chi e^2 Q)} \right) \right. \\
& \quad \left. + C_- \left( (-1)^{-s_0} \frac{i^{s_0 - iq_\chi e^2 Q} \Gamma(-2s_0 + 1)}{\Gamma(-s_0 + 1 - iq_\chi e^2 Q)} \right) \right] \times \frac{e^{ik_+ r - iq_\chi e^2 Q \log(2kr)}}{r},
\end{aligned} \tag{D.7}$$

$$\begin{aligned}
g_\chi \sim & \left[ C_+ \frac{s_0 + iq_\chi e^2 Q}{j + 1/2} \left( (-1)^{s_0} \frac{(-i)^{-s_0 + iq_\chi e^2 Q} \Gamma(2s_0 + 1)}{\Gamma(s_0 + 1 + iq_\chi e^2 Q)} \right) \right. \\
& + C_- \frac{-s_0 + iq_\chi e^2 Q}{j + 1/2} \left( (-1)^{-s_0} \frac{(-i)^{s_0 + iq_\chi e^2 Q} \Gamma(-2s_0 + 1)}{\Gamma(-s_0 + 1 + iq_\chi e^2 Q)} \right) \left. \right] \times (+i) \frac{e^{-ik_+ r + iq_\chi e^2 Q \log(2kr)}}{r} \\
& + \left[ C_+ \left( (-1)^{s_0} \frac{i^{-s_0 - iq_\chi e^2 Q} \Gamma(2s_0 + 1)}{\Gamma(s_0 + 1 - iq_\chi e^2 Q)} \right) \right. \\
& \quad \left. + C_- \left( (-1)^{-s_0} \frac{i^{s_0 - iq_\chi e^2 Q} \Gamma(-2s_0 + 1)}{\Gamma(-s_0 + 1 - iq_\chi e^2 Q)} \right) \right] \times (-i) \frac{e^{ik_+ r - iq_\chi e^2 Q \log(2kr)}}{r},
\end{aligned} \tag{D.8}$$

which consists of incoming and outgoing waves with additional phase factors,  $e^{\pm iq_\chi e^2 Q \log(2kr)}$ .

# Bibliography

- [1] I. Affleck and M. Dine, Nucl. Phys. B **249**, 361 (1985).
- [2] M. Dine, L. Randall and S. Thomas, Nucl. Phys. B **458**, 291 (1996).
- [3] S. Coleman, Nucl. Phys. B **262**, 263 (1985).
- [4] A. Kusenko and M. Shaposhnikov, Phys. Lett. B **418**, 46 (1998).
- [5] S. Kasuya and M. Kawasaki, Phys. Rev. D **61**, 041301 (2000).
- [6] S. Kasuya and M. Kawasaki, Phys. Rev. D **62**, 023512 (2000).
- [7] G. Dvali, A. Kusenko, and M. Shaposhnikov, Phys. Lett. B **417**, 99 (1998).
- [8] A. Kusenko, V. Kuzmin, M. Shaposhnikov and P. G. Tinyakov, Phys. Rev. Lett. **80**, 3185 (1997).
- [9] J. P. Hong, M. Kawasaki, and M. Yamada, Phys. Rev. D **92**, 063521 (2015).
- [10] J. P. Hong, M. Kawasaki, and M. Yamada, JCAP **08**, 053 (2016).
- [11] J. P. Hong and M. Kawasaki, Phys. Rev. D **95**, 123532 (2017).
- [12] J. P. Hong and M. Kawasaki, Phys. Rev. D **96**, 103526 (2017).
- [13] Planck Collaboration: P. A. R. Ade *et al.*, arXiv:1502.02114.
- [14] R. Kallosh and A. Linde, JCAP **1307**, 002 (2013).
- [15] M. Galante, R. Kallosh, A. Linde, and D. Roest, Phys. Rev. Lett. **114**, 141302 (2015).
- [16] R. Kallosh and A. Linde, Phys. Rev. D **91**, 083528 (2015).
- [17] A. D. Linde, Phys. Lett. B **108**, 389 (1982).
- [18] A. D. Linde, Phys. Lett. B **129**, 177 (1983).



- [19] A. A. Starobinsky, Phys. Lett. B **91**, 99 (1980).
- [20] V. F. Mukhanov and G. V. Chivisov, JETP Lett. **33**, 532 (1981).
- [21] E. J. Copeland, M. Gleiser, and H. R. Muller, Phys. Rev. D **52**, 1920 (1995).
- [22] S. Kasuya, M. Kawasaki, and F. Takahashi, Phys. Lett. B **559**, 99 (2003).
- [23] M. A. Amin, R. Easther, and H. Finkel, JCAP **1012**, 001 (2010); M. Gleiser, N. Graham, and N. Stamatopoulos, Phys. Rev. D **83**, 096010 (2011); M. A. Amin, R. Easther, H. Finkel, R. Flauger, and M. P. Hertzberg, Phys. Rev. Lett. **108**, 241302 (2012).
- [24] M. Kawasaki and N. Takeda, JCAP **07**, 038 (2014).
- [25] K. D. Lozanov and M. A. Amin, Phys. Rev. Lett. **119**, 061301 (2017).
- [26] J. Kim and J. McDonald, Phys. Rev. D **95**, 123537 (2017).
- [27] F. Hasegawa and J. P. Hong, arXiv:1710.07487.
- [28] G. N. Felder and I. Tkachev, Comput. Phys. Commun. **178**, 929 (2008).
- [29] Planck Collaboration: P. A. R. Ade *et al.*, arXiv:1502.01589.
- [30] G. Gamow, Phys. Rev. **70**, 572 (1946).
- [31] Particle Data Group Collaboration: K. A. Olive *et al.*, Chin. Phys. C **38**, 090001 (2014).
- [32] M. Kawasaki, K. Kohri, T. Moroi, and A. Yotsuyanagi, Phys. Rev. D **78**, 065011 (2008).
- [33] A. Linde, Phys. Lett. B **129**, 177 (1983).
- [34] P. J. Steinhardt and M. S. Turner, Phys. Rev. D **29**, 2162 (1984).
- [35] A. Linde, Phys. Rev. D **49**, 748 (1994).
- [36] V. Kuzmin, V. Rubakov, and M. E. Shaposhnikov, Phys. Lett. B **155**, 36 (1985).
- [37] T. Gherghetta, C. Kolda, and S. Martin, Nucl. Phys. B **468**, 37 (1996).
- [38] A. de Gouve'a, T. Moroi, and H. Murayama, Phys. Rev. D **56**, 1281 (1997).
- [39] K. Enqvist and J. McDonald, Nucl. Phys. B **570**, 407 (2000).

- [40] K. Enqvist and J. McDonald, Phys. Lett. B **425** 309 (1998).
- [41] J. Hisano, M. Nojiri, and N. Okada, Phys. Rev. D **64**, 023511 (2001).
- [42] M. Kawasaki and M. Yamada, Phys. Rev. D **87**, 023517 (2013).
- [43] S. Kasuya, M. Kawasaki, and T. T. Yanagida, arXiv:1502.00715.
- [44] T. Hiramatsu, M. Kawasaki, and F. Takahashi, JCAP **1006**, 008 (2010).
- [45] S. Kasuya and M. Kawasaki, Phys. Rev. D **64**, 123515 (2001).
- [46] K. Lee, J. A. Stein-Schabes, R. Watkins and L. M. Widrow, Phys. Rev. D **39**, 1665 (1989).
- [47] I. E. Gulamov, E. Ya. Nugaev, and M. N. Smolyakov, Phys. Rev. D **89**, 085006 (2014).
- [48] J. Arafune, T. Yoshida, S. Nakamura, and K. Ogure, Phys. Rev. D **62**, 105013 (2000).
- [49] P. B. Price and M. H. Salamon, Phys. Rev. Lett. **56**, 1226 (1986).
- [50] W. D. Wilson, L. G. Haggmark, and J. P. Biersack, Phys. Rev. B **15**, 2458 (1977).
- [51] J. L. Feng, Z. Surujon, and H. B. Yu, Phys. Rev. D **86**, 035003 (2012).
- [52] K. Hamaguchi, M. Ibe, T. T. Yanagida, and N. Yokozaki, Phys. Rev. D **90**, 015027 (2014).
- [53] A. Cohen, S. Coleman, H. Georgi, and A. Manohar, Nucl. Phys. B **272**, 301 (1986).
- [54] T. Multamaki and I. Vilja, Nucl. Phys. B **574**, 130 (2000).
- [55] M. Gleiser, Phys. Rev. D **49**, 2978 (1994).
- [56] N. Takeda and Y. Watanabe, Phys. Rev. D **90**, 023519 (2014).
- [57] J. J. M. Carrasco, R. Kallosh, and A. Linde, JHEP **10**, 147 (2015).
- [58] J. J. M. Carrasco, R. Kallosh, and A. Linde, Phys. Rev. D **92**, 063519 (2015).
- [59] R. F. Dashen, B. Hasslacher, and A. Neveu, Phys. Rev. D **11**, 3424 (1975).

- [60] E. Farhi, N. Graham, A. H. Guth, N. Iqbal, R. R. Rosales, and N. Stam-atopoulos, Phys. Rev. D **77**, 085019 (2008).
- [61] G. Fodor, P. Forgacs, Z. Horvath, and M. Mezei, Phys. Lett. B **674**, 319 (2009).
- [62] J. P. Hong, M. Kawasaki, and M. Yamazaki, arXiv:1711.10496.
- [63] LIGO Scientific Collaboration and Virgo Collaboration: B. P. Abbott, *et al.*, Phys. Rev. Lett. **116**, 061102 (2016).
- [64] B. S. Sathyaprakash and B. F. Schutz, Living Rev. Rel. **12**, 2 (2009).
- [65] C. J. Moore, R. H. Cole, and C. P. L. Berry, Class. Quant. Grav. **32**, 015014 (2015)
- [66] K. Enqvist, S. Kasuya, and A. Mazumdar, Phys. Rev. Lett. **89** 091301 (2002); K. Enqvist, S. Kasuya, and A. Mazumdar, Phys. Rev. D **66** 043505 (2002).
- [67] M. P. Hertzberg, Phys. Rev. D **82** 045022 (2010).
- [68] M. Kawasaki, M. Yamada, JCAP **02** 001 (2014).
- [69] M. Cicoli, F. G. Pedro and G. Tasinato, JCAP **12** 022 (2011).
- [70] J. P. Conlon and F. Quevedo, JHEP **01** 146 (2006).
- [71] S. Kasuya and M. Kawasaki, Phys. Rev. D **89**, 103534 (2014).